博士論文

Numerical simulation of Lamb wave propagation in CFRP skin/stringer structures for ultrasonic SHM systems to detect impact damage

(衝撃損傷を検知する超音波 SHM システムのための CFRP スキン/ストリンガ構造におけるラム波伝播の数値シミュレーション)

鄧　培文

Table of contents

1 Research background

1.1 Carbon fiber reinforced plastic (CFRP)

Carbon fiber reinforced plastic (CFRP) is a kind of composite material, which uses carbon fibers as a reinforcement and polymer resin as a matrix. Carbon fiber is a kind of reinforcing fibers which is about 7 micrometers in diameter and consists of more than 90% carbon. Carbon fiber has excellent mechanical properties such as high tensile strength and high stiffness, and other advantages including high chemical resistance and high temperature tolerance. However, the carbon fiber cannot keep its shape well. On the other hand, though not as strong as the carbon fiber, the polymer resin can keep the composites' shape very well and act as a good complement to the carbon fibers. Thus, in CFRP materials, the carbon fibers are providing strength and rigidity while the polymer resin such as epoxy is binding the reinforcements together. Because both components are lightweight materials, CFRP materials are of high specific strength and high specific stiffness when compared to metallic material. Specifically, the density of CFRP is about 1500 kg/m^3, which is only 1/5 of that of iron or 1/2 of that of aluminum, but the specific tensile strength and the specific Young's modulus of CFRP can reach 10 times and 3 times those of iron, respectively.

These properties make CFRP very suitable for the application to the aviation industry because

more usage of CFRP can lower the fuel consumption to achieve a large cost reduction. For this reason, the global leading aircraft companies, Boeing and Airbus, both have applied CFRP to the manufacturing of a majority of primary structures. To be specific, now Boeing 787 is using over 50% composite and Airbus A350 XWB is using 52% composite by weight as shown in **Fig. 1.1** [1][2][3], compared to barely 10% composite usage of previous generation Boeing 777.

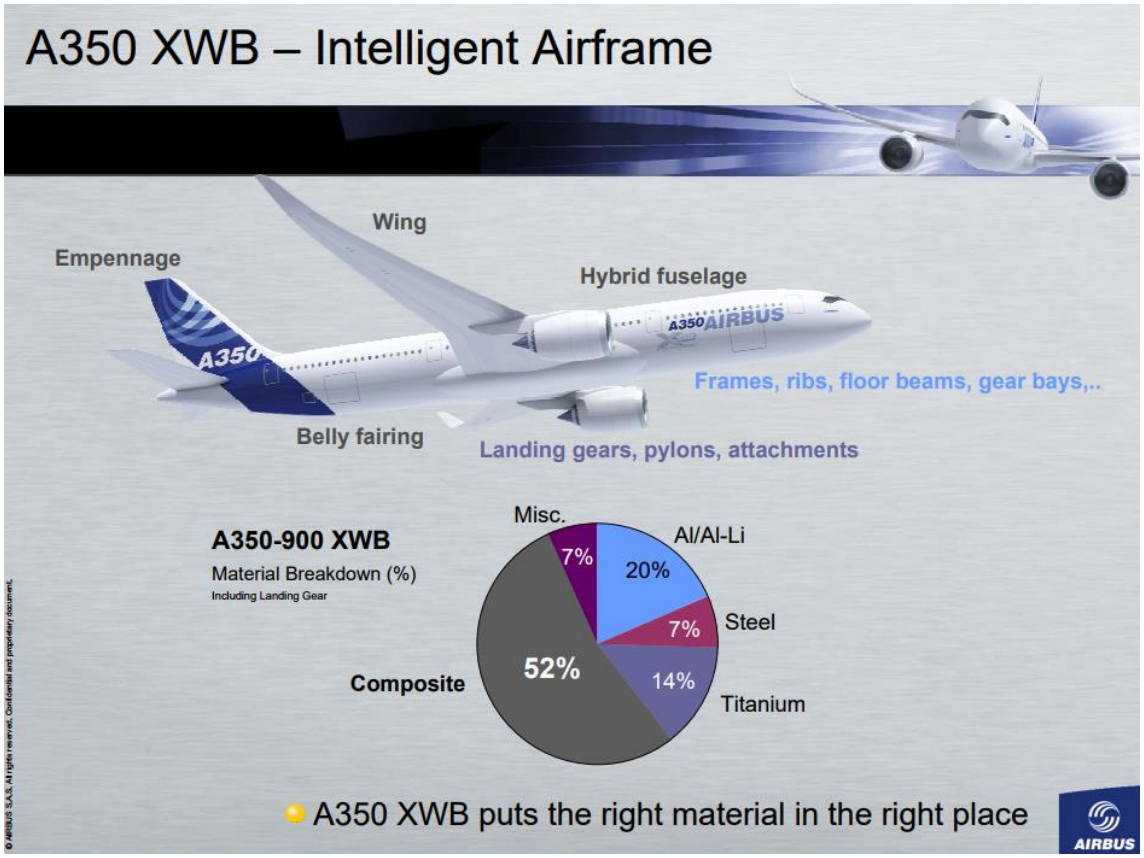

Fig. 1.1. Airbus used 52% composite in latest A350 XWB [1]

In addition to aerospace engineering, CFRP's application also concerns many industrial fields, such as automotive engineering, civil engineering, and sports goods. As the application rate

continues to increase, CFRP markets will have a rapid growth in the near future as estimated by Marsh (see **Fig. 1.2**) [4][5][6].

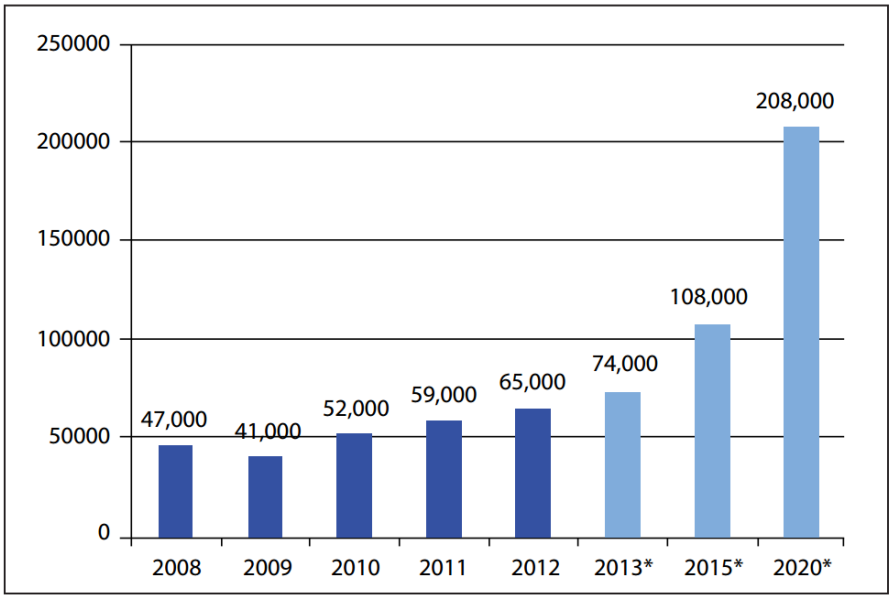

Fig. 1.2. Global demand for CFRP in tons 2008-2020 (*estimated) [5].

1.2 CFRP structures

Among those applications of CFRP, the application in the semimonocoque parts of large-scale structures is very prominent.

Semimonocoque is a shell structure combining internal ribs or frames as its stiffeners. It derives its tensile strength mainly from the external skin while derives its compressive strength part from the stiffeners. The fuselage of a Boeing 787 aircraft or chassis of a BMW i series car are typical CFRP semimonocoque structures, for example.

In such a semimonocoque fuselage, due to the existence of many repetitive periodic structures,

only one-unit of the whole structure is usually considered as a representative object of research. As shown in **Fig. 1.3**, one-unit structure is taken out from the fuselage and such a structure is usually called the "skin/stringer structure". The stringer is of hat-shaped type in this figure. In this structure, the skin functions as the load carrying member while the longitudinal stringers function as the stiffening members which support the skin and keep the skin from bucking and bending under compression or shear loads.

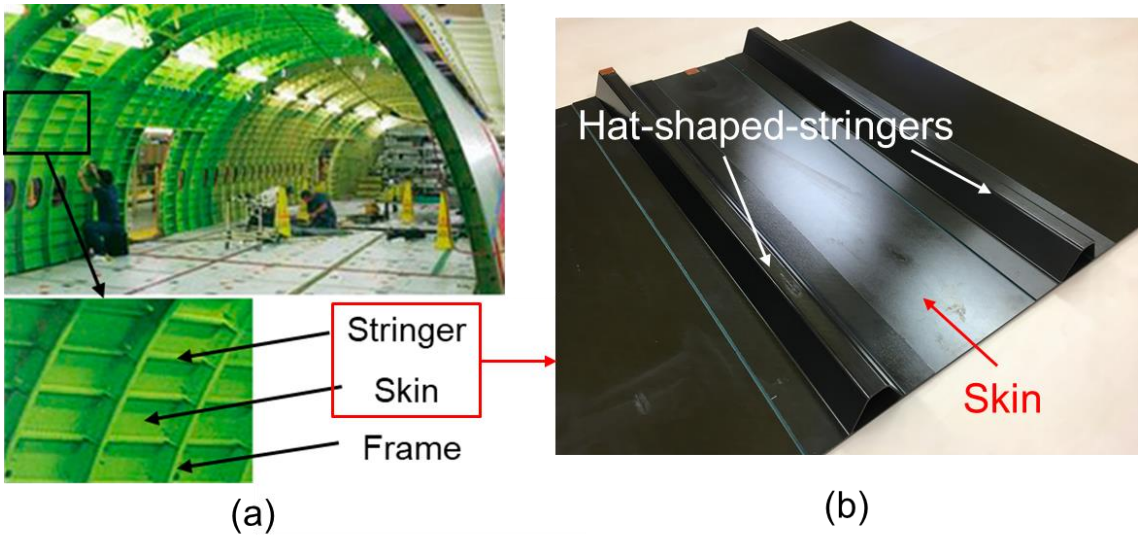

Fig. 1.3. (a) Interior of fuselage and (b) typical skin/stringer structure.

1.3 Impact damage in CFRP structures

Impact damage is one of the most common damage forms in a CFRP structure, which could occur during its manufacture, operation or maintenance process. For aircrafts, impact damage is usually caused by a dropped spanner, a runway debris, a collision with birds or a hail storm.

Impact damages having obvious surface indentation are easily detected, but most of them could hardly be detected by visual inspection. These impact damages are called barely visible impact damage (BVID). BVID is mainly caused by low-velocity impact, which can induce fatal internal damages. The severity is reflected in a significant degradation of mechanical properties by generating large amount of delamination between layers inside the structure, even though there is a very small surface indentation [7][8]. In previous literature, a reduction in residual tensile and compression strength of up to 50% have been observed in specimens which displays no visible damage [9]. Therefore, it is of great significance to detect impact damages, especially BVIDs, in CFRP structures.

1.4 Detection of impact damages

In order to detect damages, especially the BVIDs, without changing the physical state of the structure, nondestructive inspection (NDI) method is frequently used.

NDI is a collective term for a series of methods to detect the existing internal damages of a structure without causing new damages. Methods such as eddy-current, magnetic-particle, liquid penetrant, radiographic, ultrasonic and visual testing are often used in NDI [10]. In practical aircraft inspection, visual testing, knock testing and ultrasonic testing are the most used methods in NDI to examine damages.

However, executing a thorough NDI to detect BVIDs requires enormous amount of costs and labors. Since NDI is an important work among the maintenance, the maintenance costs of aircrafts can usually be very high. For example, more than 200 billion dollars per year are spent on the maintenance and repairs cost in US. And the maintenance and repairs cost can even reach a quarter of whole commercial operating costs annually [11].

One of the conventional ways to conduct NDI is to execute a "schedule-based inspection". To be specific, as shown in **Fig. 1.4 (a)**, a schedule-based inspection at certain intervals is the commonly adopted method to detect damages within the industry. In this case, a thorough nondestructive inspection is conducted during interrupt of operations and the intervals is usually a regulated period. However, the schedule-based inspection is not very effective. For example, sometimes the thorough inspection is still regularly conducted though there are no damages occurred in the structure, or sometimes the inspection is not conducted during the intervals but actually needed because of a suddenly happened damage which has uncertain effect on the structure.

To handle this problem, structural health monitoring (SHM) systems are proved to be effective by some researches [12][13]. This is because when SHM system is introduced into this inspection, the concise condition monitoring can be conducted frequently, and the health state information can be more easily obtained, as shown in **Fig. 1.4 (b)**. In this case, the inspection process becomes

demand-based at efficient intervals, which means a thorough inspection will be conducted only if it is necessary to do so.

Thus, the efficiency of NDI can be improved by introducing SHM systems into it, meanwhile the maintenance could have a largely cost reduction.

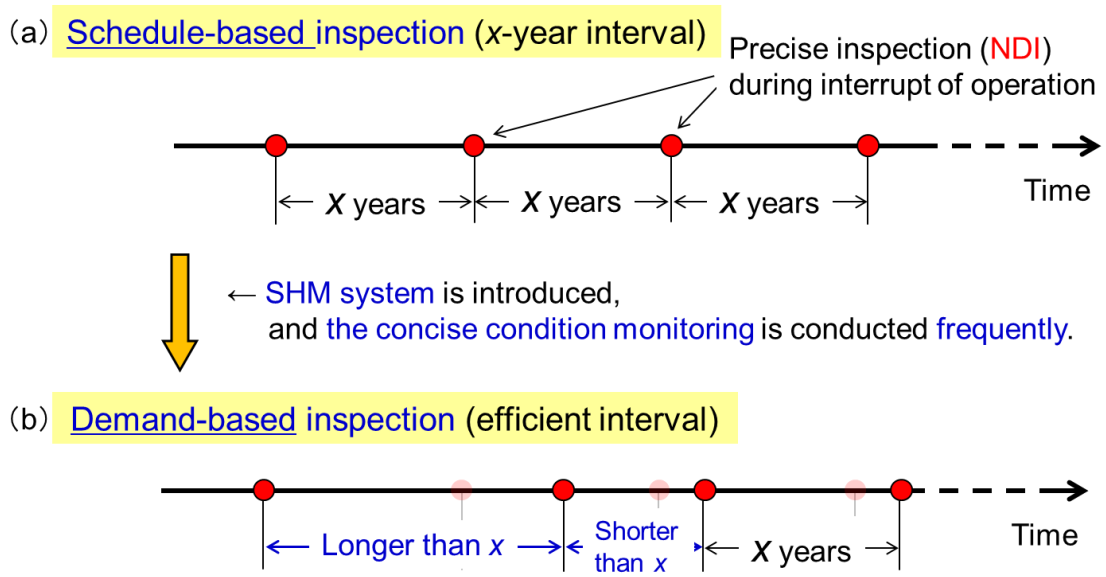

Fig. 1.4. Schematic of (a) schedule-based inspection and (b) demand-based inspection.

1.5 Introduction of SHM system

SHM system can implement different functions depending on the purpose of the design. For the detection of BVID in CFRP structures, active SHM system using guided waves is mostly used.

1.5.1 Active SHM method

Structural health monitoring (SHM) is an emerging interdisciplinary research area, and it aims at assessing the present health state of a structure by using its integrated sensors network. As **Fig. 1.5** shows, the sensors network is similar to human body's nervous system. We could regard SHM systems as a doctor and the structure as a patient: for the objective of SHM method, the doctor can diagnose the patient and give a judgement of the patients' health condition [14].

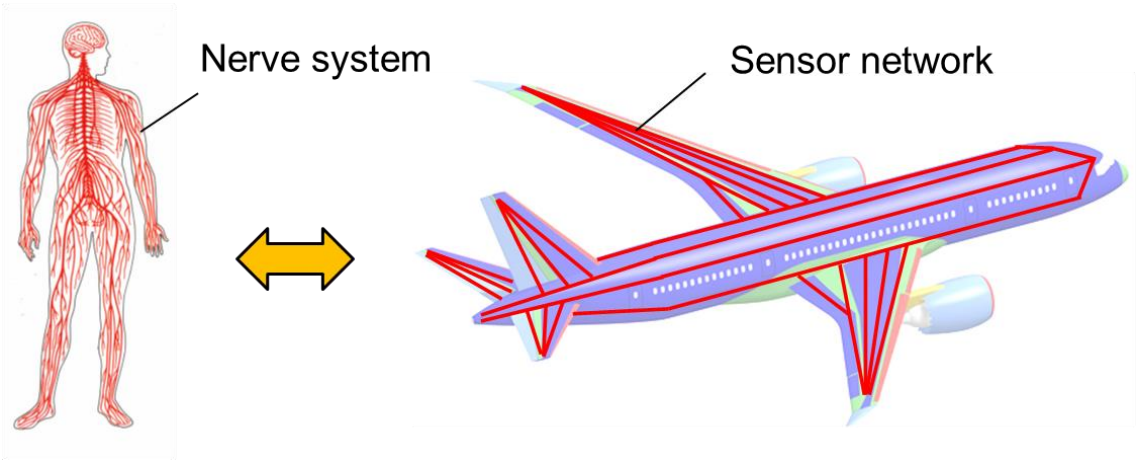

Fig. 1.5. Nerve system of human body is similar to sensors network of aircraft

In terms of performing forms, SHM methods could be classified as two types: a) passive SHM; and b) active SHM [11]. As shown in **Fig. 1.6**, passive SHM and active SHM methods both have sensors embedded in the monitored structure and the monitored structure will respond accordingly when the external environment changes such as an emergence of damage. But they also have differences. The passive SHM concerns about measuring the physical changes of monitored

structure caused by external environment directly, such as loading, stress, acoustic emission (AE) signals. On the other hand, active SHM concerns about measuring the perturbation in the received signals and these signals are excited by the embedded actuator and will perturb according to the emergence of the physical changes.

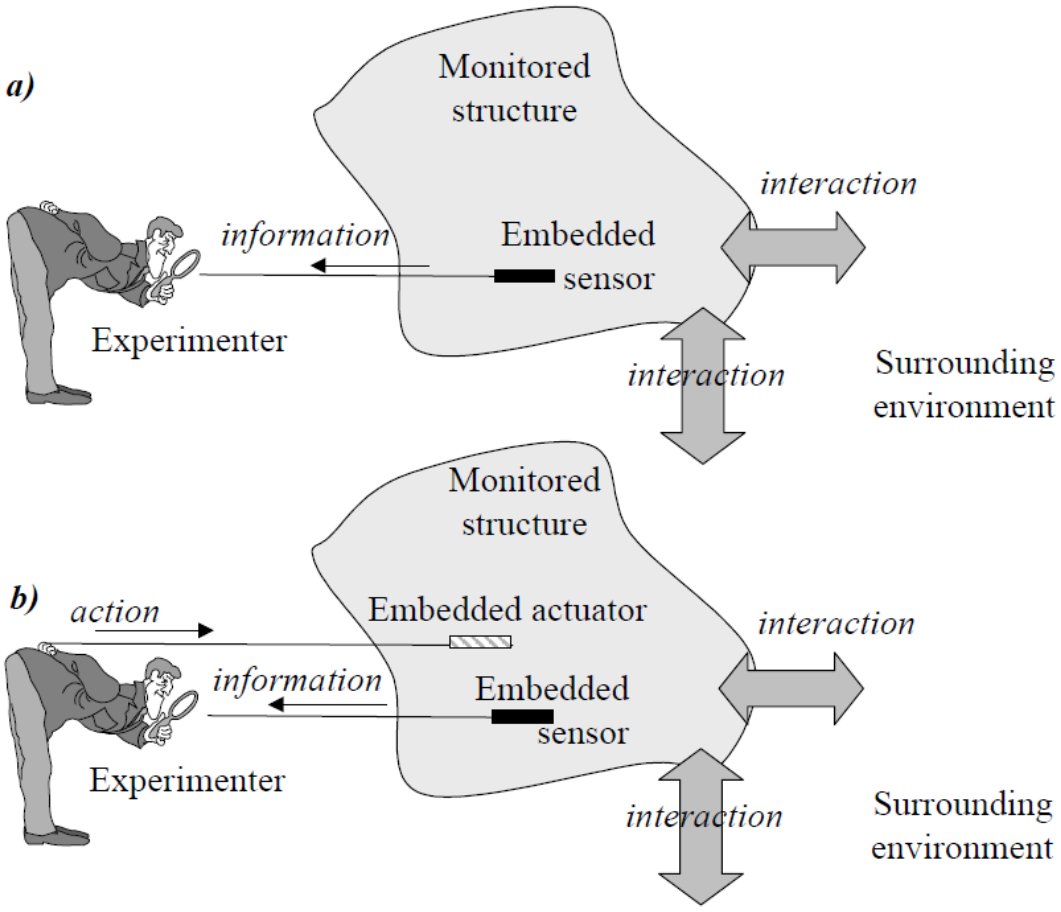

Fig. 1.6. Two main ways to perform SHM: a) passive and b) active [10].

Passive SHM method is useful, but it's less reliable because passive SHM method does not directly assess the health state of the structure but infers the health state using passive sensors

[15]. In contrast, active SHM can provide us the information of the present health state and based on this we can make more reliable decisions such as if we can continue to use it or should carry out thorough nondestructive inspections and repairs. In this respect, active SHM methodology can provide valuable information for the execution of NDI.

1.5.2 Guided waves

Among active SHM, guided waves testing is mostly used because it can offer an effective and reliable way to evaluate the presence, severity, location, type of damage, etc. [16].

Guided waves are mechanical stress waves which propagate in a structure and their travelling is guided by the structure's boundaries. According to the boundary conditions of the structure, guided waves are classified as different types. For instance, shear horizontal plate waves (SH waves) and Lamb waves propagate in plates; Rayleigh waves propagate in surfaces; flexural waves and torsional waves propagate in rods.

Among those types, Lamb wave, named after Horace Lamb, was found in thin plates with parallel free boundaries in 1917. But it hasn't been used as a means of detecting damage until 1961 (applied firstly by Dr. Worlton) [17], when compared to the conventional ultrasonic testing which is developed earlier in 1942 by Dr. Floyd [18] and applied more widely today. However, guided waves testing or Lamb waves testing have the advantages that (1) it makes long distance

inspection available; (2) it enables the inspection in inaccessible regions of structure; and (3) it has high sensitivity to multiple damage forms [19]. **Fig. 1.7** revealed the difference between these two kinds of testing methods in schematic.

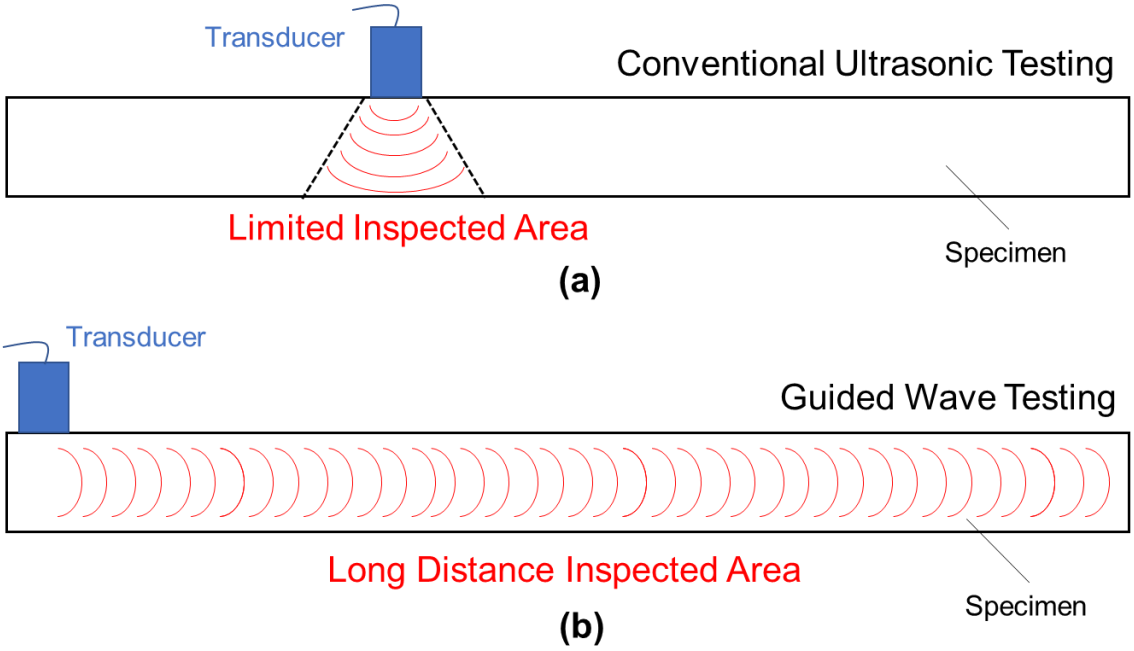

Fig. 1.7. Schematic of (a) conventional ultrasonic testing and (b) guided wave testing.

1.5.3 Development of the SHM system

A generic active SHM system is shown in **Fig. 1.8** [11]. It is consisting of two kinds of modules. The hardware module includes several embedded sensors, data concentrators, and a monitoring unit, while the software module contains the data acquisition, management, deliver and diagnosis systems. The two modules work as complement to each other.

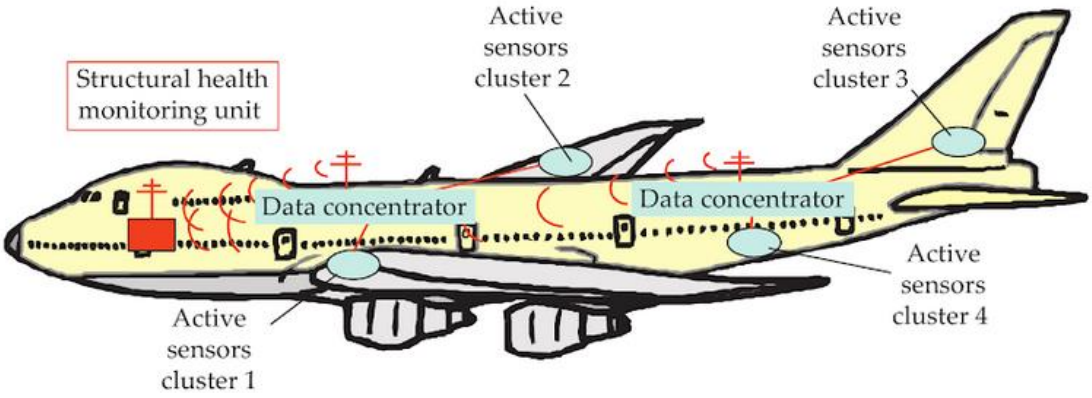

Fig. 1.8. Schematic of a generic active SHM system [11].

Fig. 1.8 shows that SHM system is very large and complex. The development of a reliable integrated SHM system is not easy and usually takes several years. From 2005, SUBARU and our research groups started to develop a SHM system consisting of a micro fiber composite (MFC) actuator, which is a film-type piezoelectric transducer, and a fiber Bragg grating (FBG) sensor, which is a kind of optical fiber sensor, to detect damages in a wide area of CFRP skin/stringer structures (see **Fig. 1.9**). The MFC actuator generates ultrasonic Lamb wave which propagates in the structure and is received by the FBG sensor. As the damage initiates and grows in the structure, the propagated Lamb wave changes. Then, an interrogation unit gives a judgement about whether a damage exists by analyzing the Lamb wave's waveform differences between the intact case and the damaged case [20].

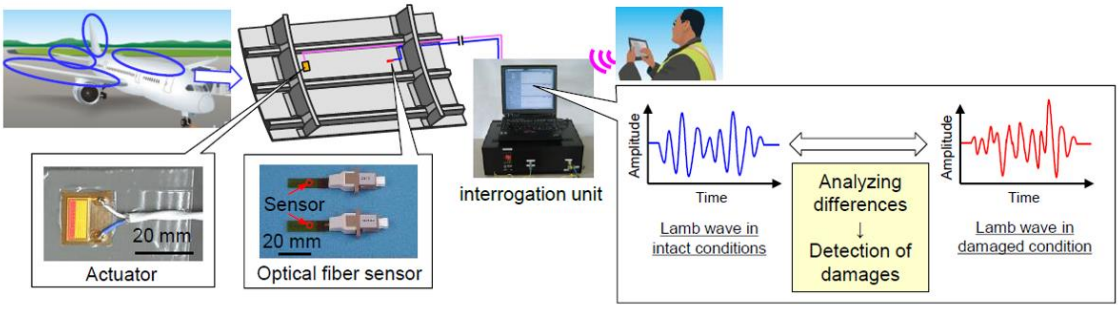

Fig. 1.9. Overview of SHM system developed by SUBARU [20].

1.5.4 Reliability of the SHM system

SUBARU and our research groups have made lots of attempts in developing similar SHM systems with integrated sensors to detect debonding, delamination or impact damage for the past decades [21][22][23][24][25][26][27]. Most of these researches proposed methods to recognize the signals in order to detect different damages, however, they lack the verification of reliability of proposed SHM system. Thus, to make a SHM system more reliable, practical problems need to be addressed. For example, for the detection of BVIDs in a CFRP skin/stringer structure, various impact damages with different location or dimensions should be taken into consideration (see **Fig. 1.10**), because a reliable SHM system must respond to various damage situations. This requires an optimal configuration of actuator(s)/sensor(s).

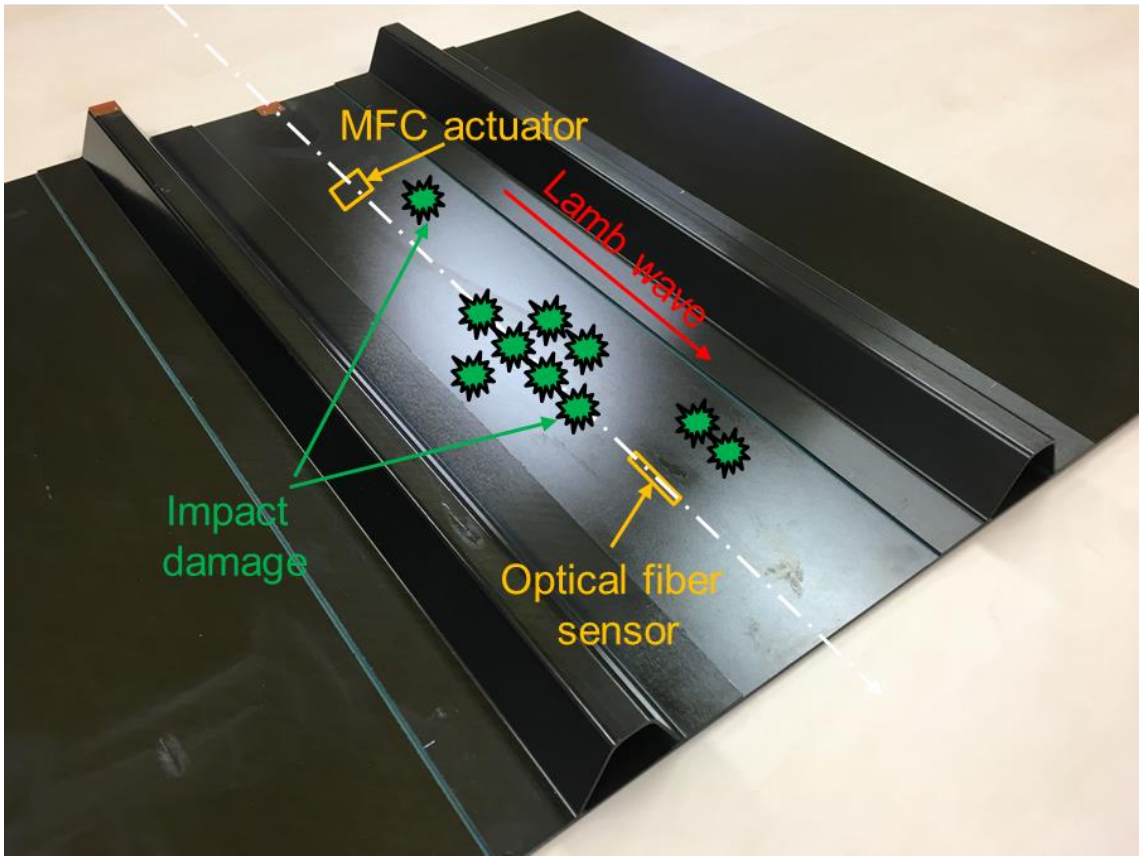

Fig. 1.10. Various impact damages in a skin/stringer structure with different dimension and location.

1.5.5 Methods to optimize the configuration

In order to determine the optimal configurations of ultrasonic actuators and sensors, the wave propagation behavior should be clarified for various impact damages with different dimensions and locations [28]. Although the optimal placement of sensors for SHM have been studied early by using mathematical tools [29][30][31], the experimental investigation is still the most common method to optimize the configuration in reality [32]. The experimental investigation is usually costly, laborious, and time-consuming. This is because the specimen cannot be used again after

the first impact generation test. Every time the position or dimension of an impact damage is changed, a new specimen is needed.

In contrast, in the simulation, since the position and dimension of the impact damage can be changed easily with a few adjustments in the finite element method (FEM) software, the investigation of the optimal configurations based on numerical simulations is more efficient and economical.

1.6 Objective of this thesis

Therefore, in this study, we attempt to establish an effective simulation method to investigate the ultrasonic propagation behavior in CFRP structures with impact damages with different dimensions and locations.

In specific, the content of this thesis are as follows:

First, we attempted to establish a simplified modeling method of an impact damage in a quasi-isotropic CFRP laminate plate. Instead of simulating the details of the impact-damage area, we simply reduce elastic constants in the region of the impact. The reason of proposing the simplified model is that it will greatly reduce time cost of modeling by avoiding tedious labor. Then, we incorporated the simulation method of an impact damage into a FEM model of a CFRP skin/hat-shaped stringer structure and simulated the wave propagation behavior in the damaged structure.

Then the applicability of the modeling method was evaluated through the comparison with experiment results. Furthermore, in order to understand the complex waveform received in the sensor, we attempted to calculate theoretically the dispersion characteristics of Lamb waves in complex-shaped structures by constructing a modified semi-analytical finite element (SAFE) method. Finally, a brief summary was made about the whole thesis. In appendix, the propagation behaviors in woven CFRP laminates with impacts are also investigated to evaluate the applicability of this simulation method.

1.7 Framework of this thesis

The frame work of this thesis is shown in **Fig. 1.11**.

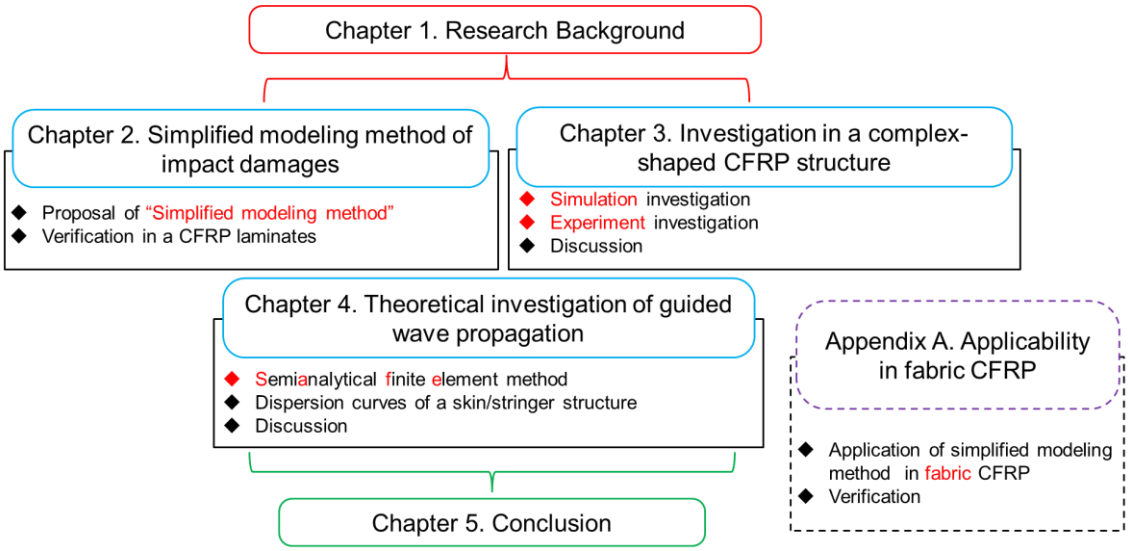

Fig. 1.11. Framework of this thesis.

The whole thesis includes 5 chapters and an appendix chapter. **Chapter 1** is the introduction and research background. The CFRP, CFRP structures, impact damage, detection of impact damage, introduction of SHM, and the objective are discussed. In **Chapter 2**, the simplified modeling method of impact damages in CFRP structures was introduced and then this method was verified with experiments. In **Chapter 3**, this simulation method was applied to a complex-shaped CFRP structure, then the simulation investigation and the experiment investigation were discussed. Then to help understanding the waveforms that we obtained in **Chapter 3**, the theoretical investigation of guided wave propagation was conducted by the calculation of the dispersion curves with modified SAFE method in **Chapter 4**. And in **Chapter 5**, a brief conclusion about my research was made. Finally, the investigation of guided wave propagation in a fabric CFRP laminates is discussed in the appendix chapter.

2 Simplified modeling method of impact damage

2.1 Introduction

In this thesis, we first present our investigation of impact damage modeling in a quasi-isotropic CFRP plate in which guided Lamb waves propagate.

Because impact damages in CFRP structures consist of multiple microscopic damages, such as delamination, shear cracks, and transverse cracks, it is difficult to precisely model the impact damages for FEM analysis. However, in order to investigate the SHM systems to detect impact damages, we need to model various kinds of impact damages easily. Therefore, we attempt to establish a simple modeling method of impact damages. When the wavelength of a Lamb wave is much longer than the microscopic damages, we can assume the impact-damaged area as a homogeneous region with the stiffness degradation. The benefit of this model is to reduce the time to construct FEM models. In particular, we can easily set several damages in various positions of the structure.

2.2 Simplified modeling method of impact damage

2.2.1 Theoretical background: stiffness matrix and velocities of Lamb waves in

quasi-isotropic composite plate

A quasi-isotropic composite plate can be represented by five independent stiffness coefficients $C_{11}, C_{12}, C_{13}, C_{33},$ and C_{44} (3-axis corresponds to out-of-plane direction). The 6 × 6 stiffness matrix is

$$\begin{bmatrix} C_{11} & C_{12} & C_{13} & 0 & 0 & 0 \\ C_{12} & C_{11} & C_{13} & 0 & 0 & 0 \\ C_{13} & C_{13} & C_{33} & 0 & 0 & 0 \\ 0 & 0 & 0 & C_{44} & 0 & 0 \\ 0 & 0 & 0 & 0 & C_{44} & 0 \\ 0 & 0 & 0 & 0 & 0 & C_{66} \end{bmatrix},$$

where

$$C_{66} = \frac{C_{11}-C_{12}}{2}. \tag{1}$$

The relationships between elastic constants and stiffness coefficients in the quasi-isotropic case are as follows:

$$\begin{cases} C_{11} = \frac{1-\nu_{23}\nu_{32}}{E_2E_3\Delta}, \\ C_{12} = \frac{\nu_{21}+\nu_{31}\nu_{23}}{E_2E_3\Delta}, \\ C_{13} = \frac{\nu_{31}+\nu_{21}\nu_{32}}{E_2E_3\Delta}, \\ C_{33} = \frac{1-\nu_{12}\nu_{21}}{E_1E_2\Delta}, \\ C_{44} = G_{23}, C_{66} = G_{12}, \end{cases} \tag{2}$$

where

$$\Delta = \frac{1-\nu_{12}\nu_{21}-\nu_{23}\nu_{32}-\nu_{13}\nu_{31}-2\nu_{21}\nu_{32}\nu_{13}}{E_1E_2E_3}, \tag{3}$$

ν's are Poisson's ratios, E's are longitudinal elastic moduli, and G's are transverse elastic moduli. The stiffness coefficients of CFRP quasi-isotropic laminates (T700S/2500, $[45/0/-45/90]_{3s}$) are given in **Table 2.1**.

Table 2.1. Density and stiffness constants of CFRP (T700S/2500)

	ρ	C_{11}	C_{12}	C_{13}	C_{33}	C_{44}	C_{66}
Quasi-isotropic	1530	57.57	19.31	5.16	10.71	3.46	19.13
Unidirectional	1530	133.09	4.98	4.98	10.71	2.70	4.80

Density in kg/m^3 and stiffness constants in GPa.

The stiffness coefficients and density ρ are related to the velocity of elastic waves. For example, the velocity of a longitudinal bulk wave propagating in the thickness direction is expressed as

$$v_{\text{bulk}} = \sqrt{\frac{C_{33}}{\rho}}. \tag{4}$$

A guided wave in a plate (Lamb wave) has many modes, and the existence and velocity of which are significantly dependent on frequency. It is convenient to use dispersion curves to describe such a relation between velocity of modes and the frequency. There are two basic types of modes existing in Lamb waves, the symmetric modes and antisymmetric modes. For each type, there exist a number of modes corresponding to the solutions of Rayleigh-Lamb equation

$$\begin{cases} \dfrac{\tan pd}{\tan qd} = -\dfrac{\left(\xi^2 - q^2\right)^2}{4\xi^2 pq} \ (symmetric), \\ \dfrac{\tan pd}{\tan qd} = -\dfrac{4\xi^2 pq}{(\xi^2 - q^2)^2} \ (antisymmetric), \end{cases} \tag{5}$$

where p and q are given by

$$p^2 = \frac{\omega^2}{C_P^2} - \xi^2, q^2 = \frac{\omega^2}{C_S^2} - \xi^2, \tag{6}$$

ω is angular frequency, ξ is wave number, C_P is longitudinal wave speed, C_S is transverse

wave speed, and d is half thickness of plate.

For each symmetric modes, they are designated S_0,S_1,S_2,⋯, and for antisymmetric modes, they are designated A_0, A_1, A_2,⋯. **Fig. 2.1** shows the dispersion curves of group velocities of Lamb waves propagating in a 3.4-mm-thick CFRP plate. This dispersion curves can be easily calculated by software DISPERSE theoretically based on the extension of **Eqs.(5)** to anisotropic materials. DISPERSE is an interactive Windows program designed to calculate dispersion curves for multilayered anisotropic structures and developed by Imperial College.

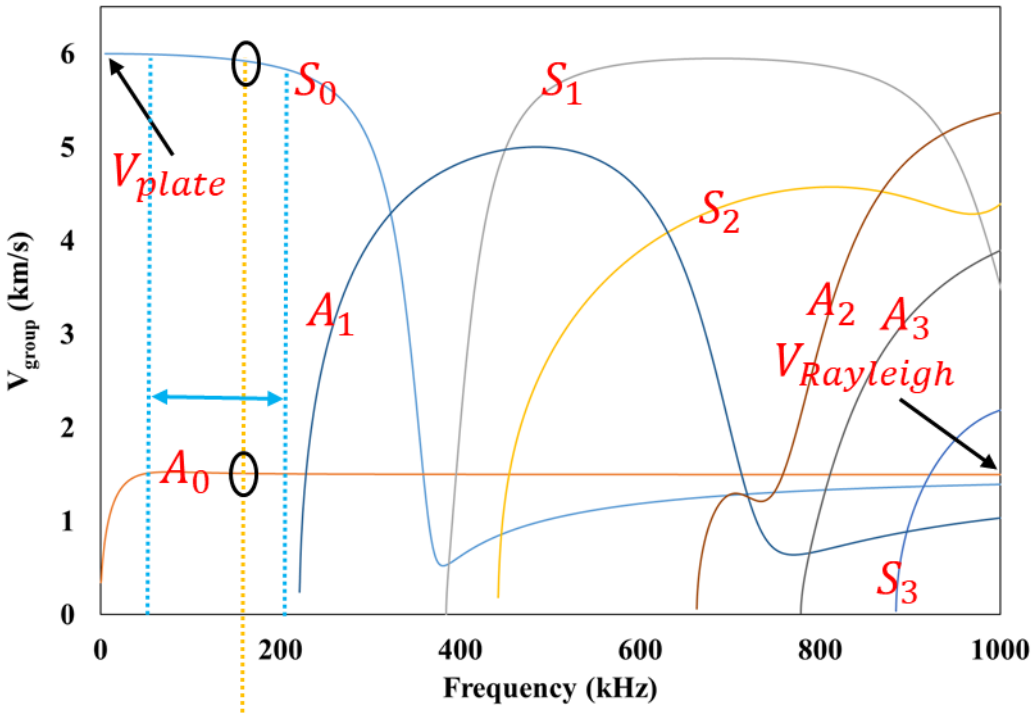

Fig. 2.1. Dispersion curves of group velocities of Lamb waves in a 3.4-mm-thickness CFRP quasi-isotropic plate. The parameters in **Table 2.1** were used to obtain the curves.

At low frequencies, i.e., $f \leq 220$ kHz, the velocity of the lowest-order symmetric mode (S_0) reaches a constant value known as the plate velocity v_{plate}:

$$v_{S_0} \rightarrow v_{\text{plate}}. \tag{7}$$

In an isotropic thin sheet [33], the plate velocity is expressed as

$$v_{\text{plate}} = \sqrt{\frac{4(\lambda+\mu)\mu}{(\lambda+2\mu)\rho}}, \tag{8}$$

where λ and μ are Lamé constants. Similarly, in a quasi-isotropic CFRP plate, the plate velocity is expressed as

$$v_{\text{plate}} = \sqrt{\frac{C_{11}C_{33}-(C_{13})^2}{\rho C_{33}}}. \tag{9}$$

Because C_{13} is much smaller than C_{11} and C_{33} for a quasi-isotropic CFRP plate, C_{13} can be omitted from **Eq. (9)**, yielding the following equation:

$$v_{\text{plate}} \approx \sqrt{\frac{C_{11}}{\rho}}. \tag{10}$$

At high frequencies, the velocities of the lowest-order modes (A_0 and S_0) are close to the velocity of a Rayleigh surface wave, v_{Rayleigh}. In particular, although the velocity of the lowest-order antisymmetric mode, v_{A_0}, sharply changes at frequencies < 40 kHz, it approximates to a constant v_{Rayleigh} at frequencies > 40 kHz:

$$v_{A_0} \rightarrow v_{\text{Rayleigh}}. \tag{11}$$

The velocity of a Rayleigh surface wave is close to that of a transverse wave, $v_{\text{transverse}} = \sqrt{\frac{C_{44}}{\rho}}$ [11]. Therefore,

$$v_{\text{Rayleigh}} \approx \sqrt{\frac{C_{44}}{\rho}}. \tag{12}$$

For a 3.4-mm-thick CFRP plate, in the frequency range 40-220 kHz, the velocities of A_0 mode and S_0 mode satisfy both **Eq. (7)** and **Eq. (11)**, they are respectively

$$v_{S_0} \approx \sqrt{\frac{C_{11}}{\rho}},\ v_{A_0} \approx \sqrt{\frac{C_{44}}{\rho}}. \tag{13}$$

In the above frequency range, S_0 and A_0 modes are propagating waves (the higher modes cannot propagate). The minimum ultrasonic wavelength of the propagating waves is > 6.8 mm (calculated with velocity of A_0 mode and frequency at 220 kHz), which is much larger than the thickness of the plate. Therefore, homogeneous effective stiffness parameters can be used.

2.2.2 Observation of impact-damaged area

We prepared a 3.4-mm-thick CFRP quasi-isotropic laminate plate (T700SC/2500 $[45/0/-45/90]_{3s}$) for the observation of an actual impact damage. The CFRP used in the experiment is T700SC/2500 instead of T700S/2500 because T700S/2500 is no longer marketed. And since we don't have the information about the stiffness constants of T700SC/2500, we make an assumption that T700SC/2500 has the same degradation ratio in the impact-damaged area as that of T700S/2500.

Impact damage in the form of a 4-mm-diameter dent was generated at the center of the plate. The plate is shown in **Fig. 2.2**. Then, an ultrasonic C-scan observation was conducted to measure

the size of the damaged area, as shown in **Fig. 2.3**. The damaged area was quasi-isotropic and approximately 28 mm in diameter. After cutting through the damaged area, a microscope was used to observe its cross section to investigate the damage, as shown in **Fig. 2.4**. Delamination could be found around the impact point and the delaminated area increased in the deeper interfaces of the plies.

Fig. 2.2. CFRP laminate plate with an impact damage at the center.

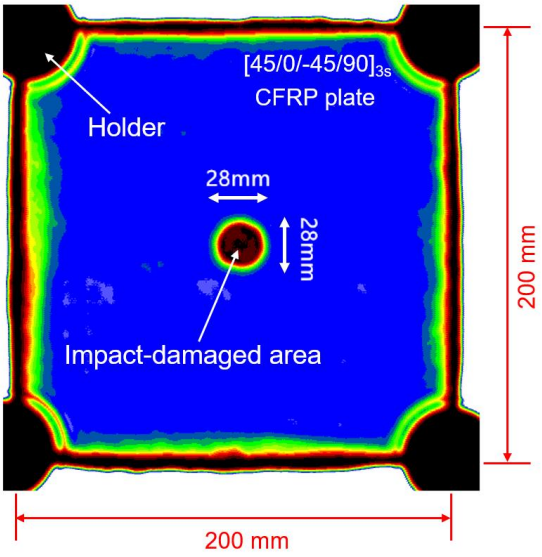

Fig. 2.3. C-scan observation of the damaged CFRP plate.

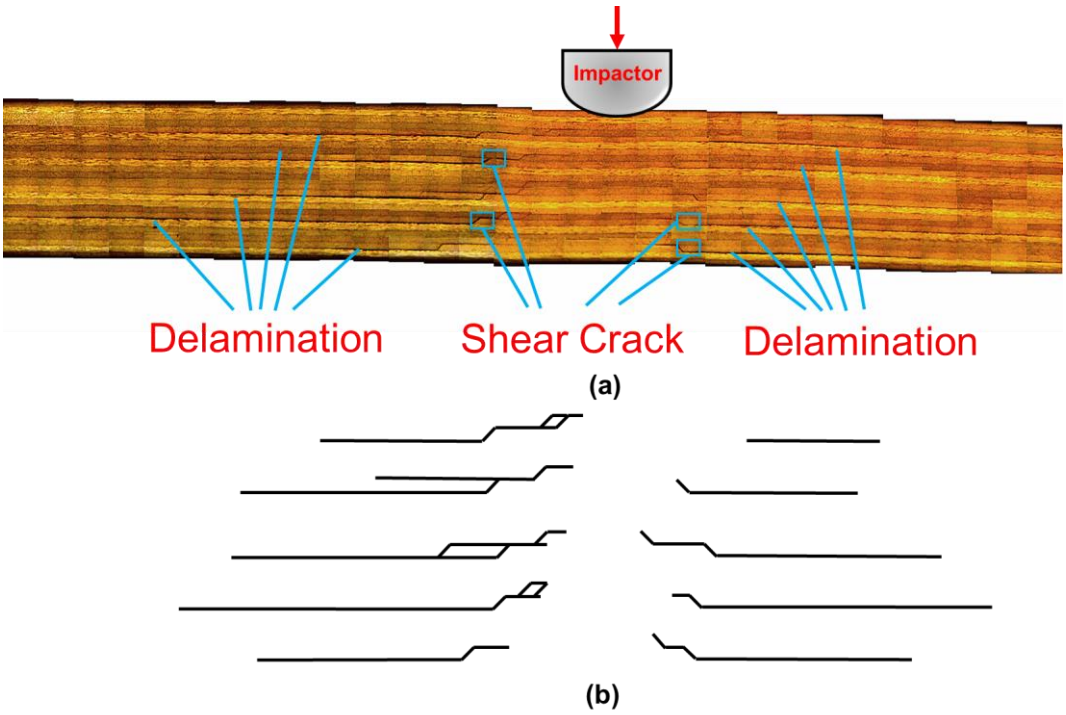

Fig. 2.4. (a) Cross-sectional image observed by a microscope and (b) schematic of the damages.

From the observations, we considered the impact-damaged region as a frustum with degraded stiffness constants [34]. **Fig. 2.5 (a)** shows the geometry of our model of the impact-damaged region, which was assumed to be homogeneous and quasi-isotropic. **Fig. 2.5 (b)** shows the FE model of the impact-damaged region.

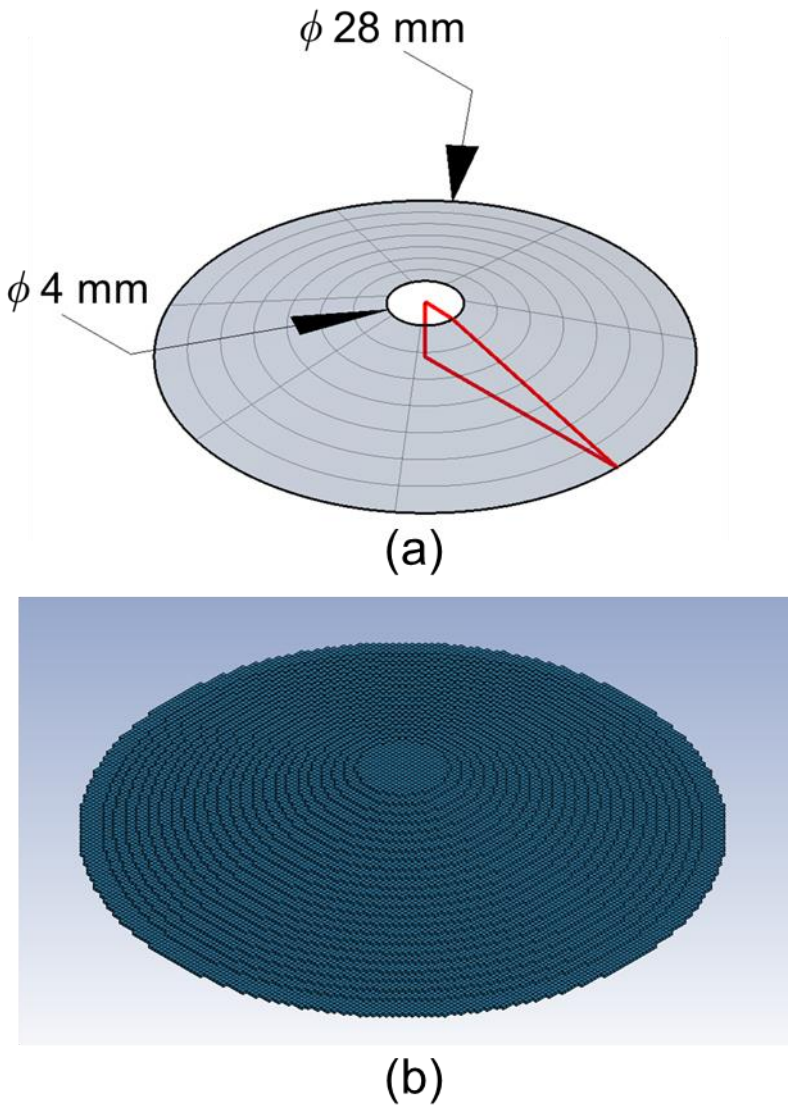

Fig. 2.5. (a) Impact-damaged region assumed to be a homogeneous and quasi-isotropic frustum with degraded stiffness constants, (b) FE Model of impact-damaged region with LS-DYNA.

In this thesis, the modeling of impact damage as a frustum, the stiffness of which is homogeneously degraded, is called the "simplified modeling method". These hypotheses will be verified in **Section 2.3**.

2.2.3 Determination of stiffness constants by measurement of ultrasonic propagation

To establish the simplified model, the degradation rates of the stiffness coefficients in the impact-damaged area must be determined. Of the five independent stiffness coefficients, C_{11} and C_{44} can be determined based on the change in the ultrasonic velocities, C_{12} and C_{13} can be deduced from the cross-sectional observation, and C_{33} is discussed in detail in the following section.

2.2.3.1 Determination of C_{11} and C_{44} based on the change in ultrasonic velocities

The degraded values of C_{11} and C_{44} can be determined based on the change in ultrasonic velocities from ultrasonic experiments. We first investigated Lamb wave's propagation in the specimen plate. An ultrasonic actuator (AE sensor NF-AE-900M, NF Corporation, Yokahama, Japan) was fixed on the top of the plate and two ultrasonic sensors were set symmetrically on the top and bottom of the plate as receivers (see **Fig. 2.6**). The two sensors were moved at 10-mm

intervals along the propagation path, which included the center of the impact-damaged area. By adding or subtracting the two signals detected by the two sensors, we obtained the symmetric or antisymmetric components of the signals.

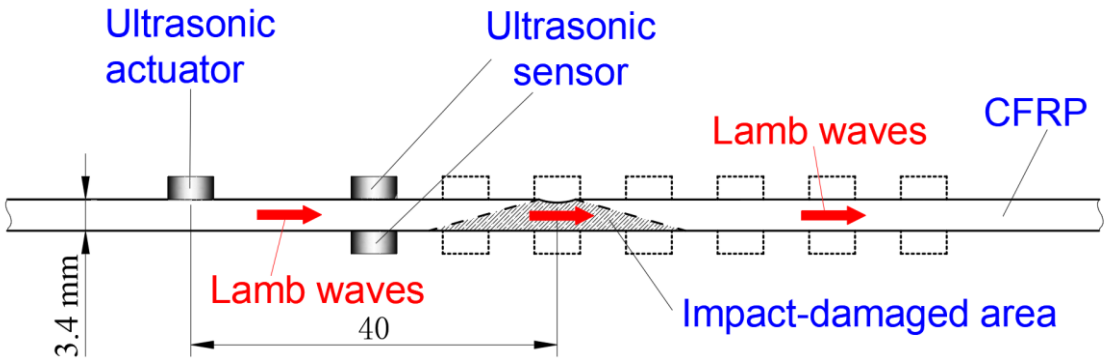

Fig. 2.6. Experimental setup for measuring Lamb wave propagation to determine C_{11} and C_{44}.

The input signal was generated as a three-cycle sinusoidal wave with a Hamming window at 180 kHz, which is between 40 and 220 kHz. The output waveform at 60 mm in the damaged plate is shown in **Fig. 2.7**.

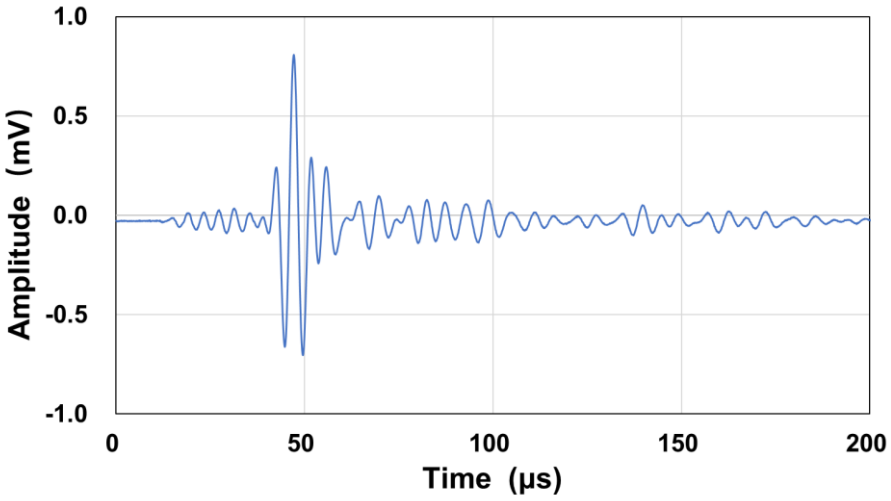

Fig. 2.7. Output waveform at a propagation distance of 60 mm in the damaged CFRP plate.

For contrast, we did the same experiment on an intact CFRP plate. **Fig. 2.8** shows the propagation times of Lamb waves in intact and damaged CFRP plates. The propagation times were determined using the maximum peaks of the waveforms. The number of experimental data of the S_0 mode were less plotted than those of the A_0 mode because it is difficult to separate the S_0 mode from the A_0 mode at a short propagation distance. **Fig. 2.8** clearly shows the increase in the propagation time due to impact damage in the propagation path, and the increase in the propagation time of the A_0 mode was greater than that of the S_0 mode. Using the assumption that the impact damage was homogeneous, we assumed that the Lamb waves propagated at constant velocities V_{im} in the impact-damaged area ($V_{\mathrm{im}} = v_{\mathrm{imS_0}}$ or $v_{\mathrm{imA_0}}$. Hereafter, $v_{\mathrm{imS_0}}$ and $v_{\mathrm{imA_0}}$ are referred to as the velocities of the S_0 and A_0 modes in the impact-damaged region. The velocities of the S_0 and A_0 modes in the intact area are referred to as $v_{\mathrm{inS_0}}$ and $v_{\mathrm{inA_0}}$.)

Additionally, the propagation distance in the impact-damaged area, S_{im}, is considered to be the average length of the maximum diameter of 28 mm and the minimum diameter of 4 mm. S_{im} was 16 mm according to the calculation.

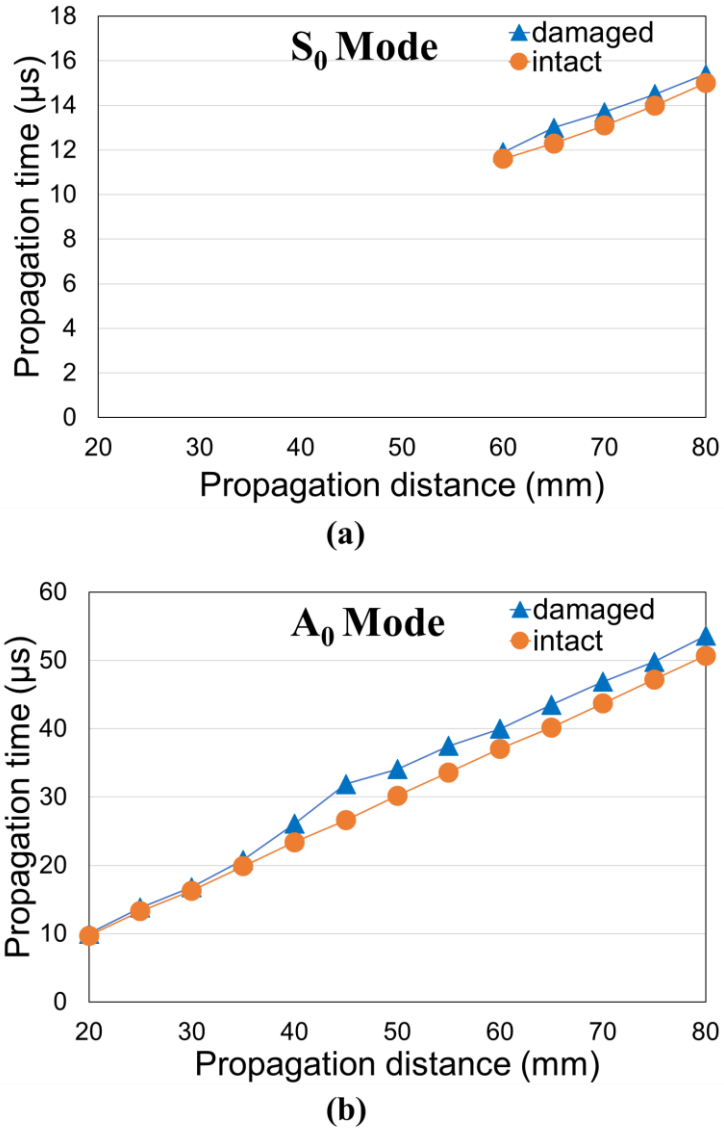

Fig. 2.8. Propagation times of Lamb waves in the intact and damaged CFRP plates. (a) S_0 and (b) A_0 modes are plotted. Input waveform was a three-cycle sinusoidal wave with a Hamming window at 180 kHz.

When a propagation distance S of the Lamb waves in the impact-damaged plate is the same as that in the intact plate, we obtain the following equations:

$$\begin{cases} t_{\mathrm{in}} \times V_{\mathrm{in}} = S, \\ t_{\mathrm{b}} \times V_{\mathrm{im}} = S_{\mathrm{im}}, \\ S_{\mathrm{im}} + t_{\mathrm{a}} \times V_{\mathrm{in}} = S, \\ t_{\mathrm{im}} = t_{\mathrm{a}} + t_{\mathrm{b}}, \end{cases} \tag{14}$$

where V_{in} ($= v_{\mathrm{inS_0}}$ or $v_{\mathrm{inA_0}}$) is the average velocity of the Lamb wave in the intact plate; t_{in} and t_{im} are the average propagation times at distance S in the intact plate and in the impact-damaged plate, respectively; and t_{a} and t_{b} are the propagation times in the intact region and in the impact-damaged region of the damaged plate, respectively. The velocity V_{im} ($v_{\mathrm{imS_0}}$ or $v_{\mathrm{imA_0}}$) and V_{in} ($v_{\mathrm{inS_0}}$ or $v_{\mathrm{inA_0}}$) can be easily obtained from **Eqs. (14)**.

The calculated group velocities in the intact area are as follows:

$$v_{\mathrm{inS_0}} = 5.30\ \mathrm{km/s}\,,\ v_{\mathrm{inA_0}} = 1.60\ \mathrm{km/s}\,,$$

and calculated group velocities in the impact-damaged area are as follows:

$$v_{\mathrm{imS_0}} = 4.55\ \mathrm{km/s}\ (85.8\%\ \mathrm{of}\ v_{\mathrm{inS_0}}),\ v_{\mathrm{imA_0}} = 1.23\ \mathrm{km/s}\ (76.7\%\ \mathrm{of}\ v_{\mathrm{inA_0}}).$$

According to Eqs. (13), because $C_{11} \propto v_{S_0}^2$ and $C_{44} \propto v_{A_0}^2$, we assumed that

$$\frac{C_{11,in}}{C_{11,im}} = \left(\frac{v_{inS_0}}{v_{imS_0}}\right)^2,\ \frac{C_{44,in}}{C_{44,im}} = \left(\frac{v_{inA_0}}{v_{imA_0}}\right)^2, \tag{15}$$

where C_{11} ($= C_{11,in}$ or $C_{11,im}$) is the stiffness constants C_{11} in the intact area or in the impact-damaged area, C_{44} ($= C_{44,in}$ or $C_{44,im}$) is the stiffness constants C_{44} in the intact area or in the impact-damaged area.

According to **Eq. (15)**, C_{11} in the impact-damaged area is assumed to degrade at the same rate

as $v_{S_0}^2$(26.2% degradation) and C_{44} in the impact-damaged area is assumed to degrade at the same rate as $v_{A_0}^2$(40.8% degradation).

2.2.3.2 Determination of C_{13} and C_{12} based on observational results

Based on the cross-section observation shown in **Fig. 2.4**, delamination was the most dominant form of damage, and it is reasonable to assume that the out-of-plane Poisson's ratios were close to 0, namely, ν_{31}, ν_{32} = 0, because the delamination could not transfer the vertical strain. Hence, according to **Eq. (2)**, C_{13} becomes 0. In addition, the in-plane Poisson's ratio ν_{12} can be assumed approximately invariant through the impact process. According to **Eq. (2)**, because $C_{11} \propto E_{11}$ and $C_{12} \propto E_{11}$, C_{12} is assumed to degrade at the same rate as C_{11} (26.22% degradation).

2.2.3.3 Determination of C_{33}

The propagation time of the longitudinal bulk wave in the thickness direction around the impact-damaged area was measured using the experimental setup shown in **Fig. 2.9**. The measured propagation time as a function of distance from the center of the impact-damaged area is plotted in **Fig. 2.10** (a). The average velocity of bulk wave in the intact area is $v_{\text{bulk}} = 2.67\text{km/s}$.

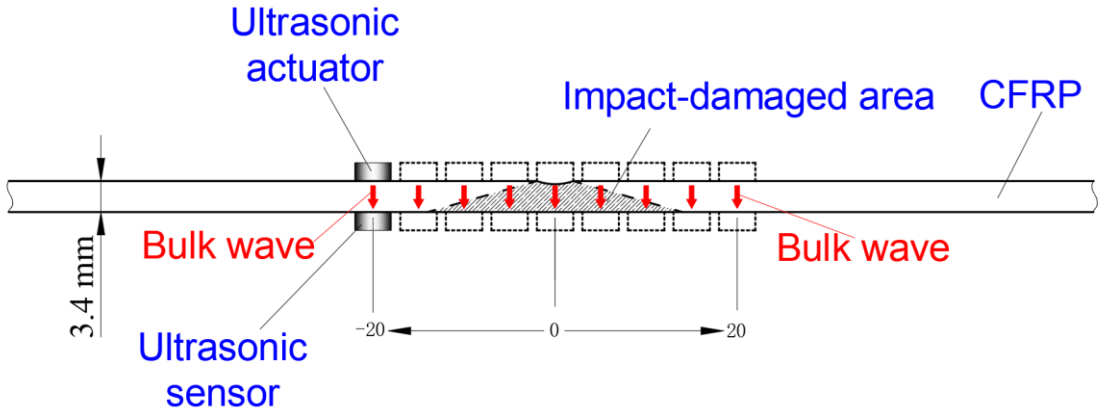

Fig. 2.9. Experimental setup for measuring longitudinal bulk wave propagation to determine C_{33}.

Input waveform was a three-cycle sinusoidal wave with a Hamming window at 180 kHz.

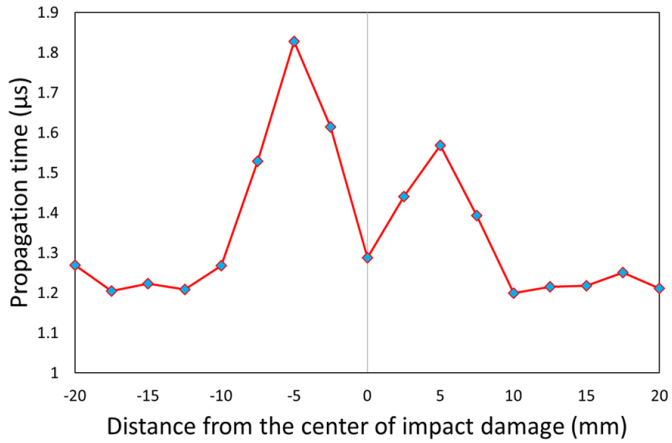

(a)

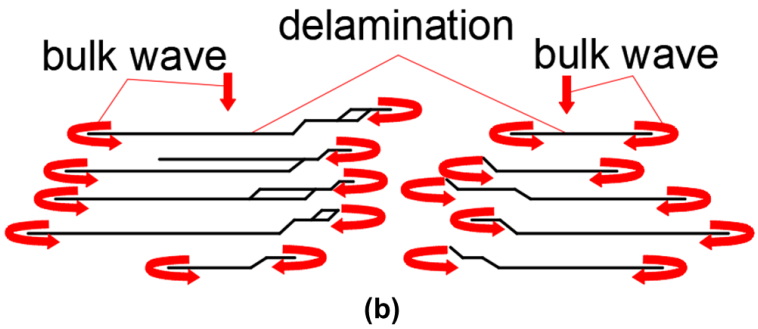

(b)

Fig. 2.10. (a) Propagation time of the longitudinal bulk wave as a function of distance from the impact damage center. (b) Bulk wave propagation time increases with the number of delaminations.

The plot shows that the bulk wave propagation time was longer around the impact-damaged area, but in the center of the impact damage, the ultrasonic propagation time was the same as that of the intact area. Considering the cross-section image in **Fig. 2.4**, delaminations probably blocked the propagation of the bulk wave in the thickness direction, as shown in **Fig. 2.10** (b). The bulk wave propagated from the upper surface to the lower surface by detouring around the delamination. Because the propagation time varied with position in the impact-damaged area, it was difficult to determine an accurate value of C_{33} for the entire model, but it should be between the values calculated with respect to the longest and shortest travel times (which are equal in the intact area) in the thickness direction. In our study, we assumed that C_{33} was not degraded, because the stiffness value in the thickness direction does not significantly affect the Lamb waves. The major concern for our model is the numerical simulation of Lamb wave behavior. Hence, a parameter unrelated to the behavior is not necessarily changed. Using the same C_{33} value as that in the intact area is simpler.

Here we present detailed verification of this fact based on simulation. We compared two values of C_{33}: intact and 51% degraded. The degraded value is calculated as

$$C'_{33} = \rho v^2_{\text{bulk\_min}}, \tag{16}$$

where $v_{\text{bulk\_min}}$ is the minimum propagation velocity of the bulk wave in the impact-damaged area from **Fig. 2.10** (a). The simulation was conducted using LS-DYNA simulation software

(Livermore Software Technology Corporation, Livermore, CA, USA). An out-of-plane force of a three-cycle sinusoidal wave with a Hamming window at 180 kHz on the CFRP plate (90 × 90 × 3.4 mm^3, mesh size = 0.2 mm in the in-panel direction and 0.14167 mm in the thickness direction) excited Lamb waves, which propagated along the plate. To estimate the time delay caused by the change in C_{33}, we calculated the cross correlation, which measures the similarity between two waveforms. By shifting the waveform calculated for the degraded case, we found the time delay between the waveform in the unchanged case and that in the degraded case. The obtained delay is shown in **Fig. 2.11**. Few differences were found because the 0.1-μs time delay is only 0.29% of 34.5 μs, which was the propagation time at the distance of 50 mm. Hence, the stiffness coefficient in the thickness direction, C_{33}, has little effect on the propagation time of Lamb waves and can be regarded as invariant in this modeling.

The above analysis was used to determine the stiffness matrix values of the impact-damaged area, as shown in **Table 2.2**. Outside this area, the stiffness matrix values remain unchanged from those of the intact CFRP shown in **Table 2.1**. With the stiffness matrix determined, we have established the simplified model.

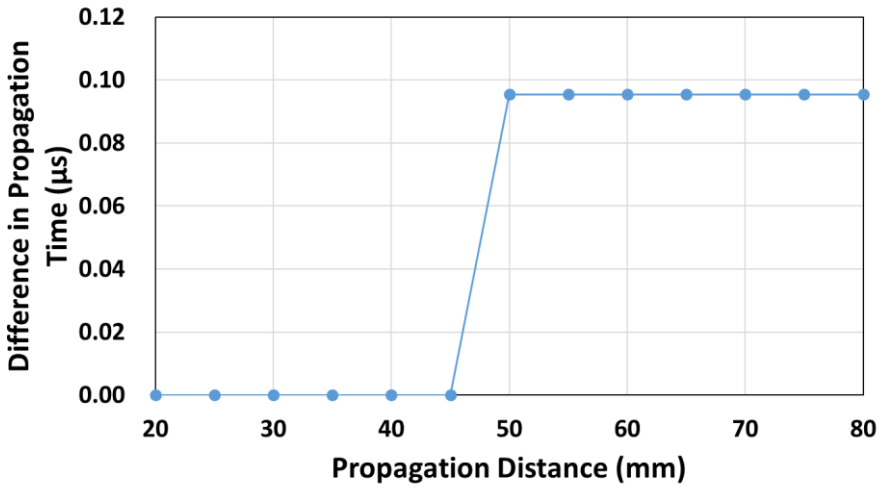

Fig. 2.11. Calculated time differences (delay) of waveforms between degraded C_{33} and unchanged C_{33} according to cross-correlation analysis.

Table 2.2. Density and stiffness constants of impact-damaged area in the simplified modeling method (T700S/2500)

	ρ	C_{11}	C_{12}	C_{13}	C_{33}	C_{44}	C_{66}
Impact-damaged area	1530	42.47	14.25	0	10.71	2.05	14.11

Density in kg/m^3 and stiffness constants in GPa

2.3 Verification of the validity of the simplified modeling method

In **Section 2.2**, we have established the simplified model of impact damage using the assumption that the impact-damaged area is quasi-isotropic and homogeneous. To verify the validity of the simplified modeling method presented in this thesis, we compared the results

calculated using this model with those calculated using a precise FEM model and those obtained by experiment.

2.3.1 Comparison with a precise multiple-delamination model

Our "multiple-delamination model" models the impact damage in detail by using double nodes to represent delamination. In this model, peanut-shaped delamination is taken into account [35][36][37]. **Fig. 2.12** shows our multilayer-delamination model where each peanut-shaped delamination between adjacent plies extends along the direction of the ply. The delamination size increases with depth. In this model, each laminate layer was simulated using the unidirectional stiffness constants listed in **Table 2.1**. The laminate configuration was $[45/0/-45/90]_{3s}$. Using LS-DYNA, we calculated the Lamb wave propagation through the damaged area with a propagation distance of 40 mm along four directions: 45°, 0°, -45°, and 90°. Then, the calculated waves underwent wavelet transformation. The results are presented in **Fig. 2.13** as propagation time as a function of frequency. The velocity and frequency of the Lamb waves in the four directions were in good agreement. Thus, the dependence of Lamb wave propagation on direction is negligible, even in the laminated multiple-delamination model, considering the difference of fiber direction in each ply. Therefore, the assumption that the impact-damaged area is quasi-isotropic used in constructing the simplified model is reasonable and acceptable.

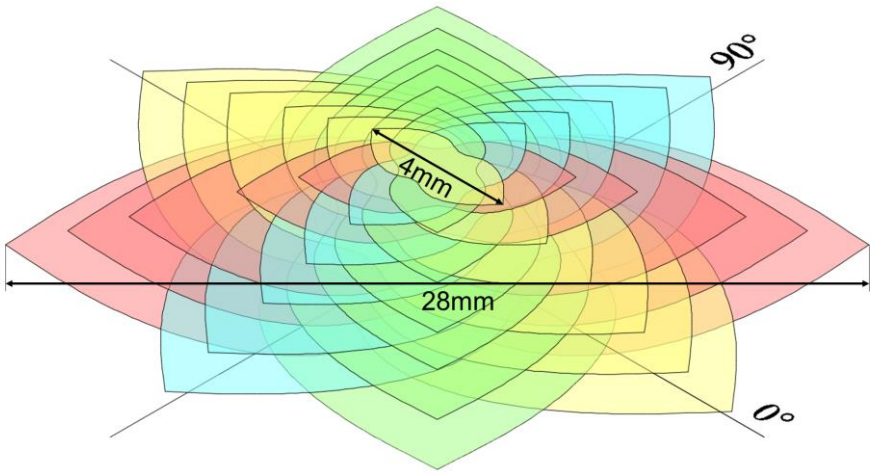

Fig. 2.12. Schematic of delamination used in the multiple-delamination model of impact damage.

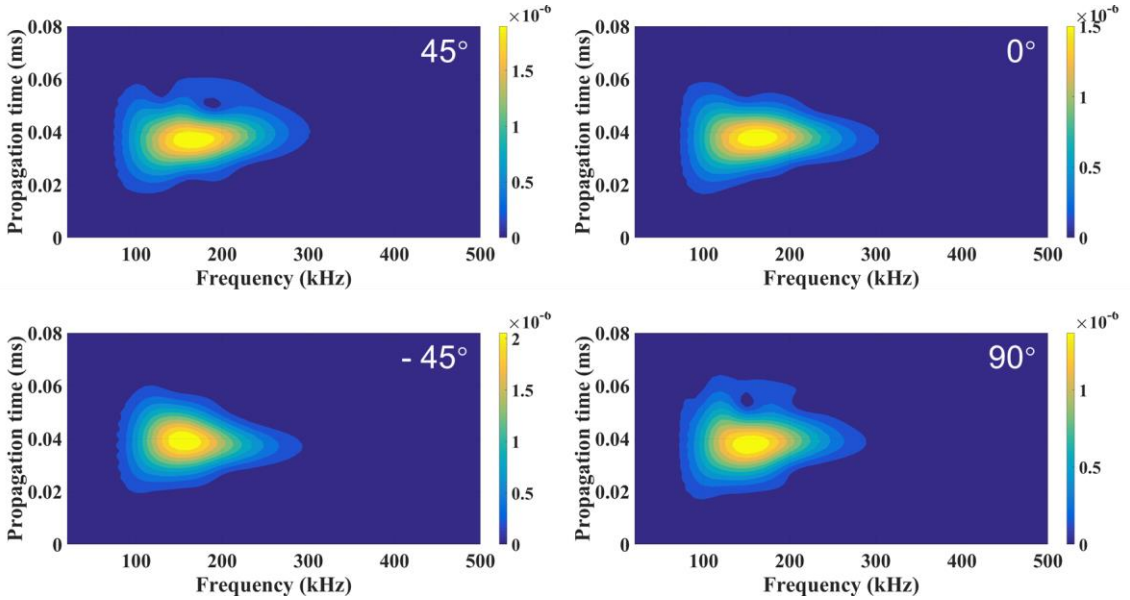

Fig. 2.13. Wavelet transformations of waves propagating through the impact-damaged region in four propagation directions. The laminated multiple-delamination model was used, and the propagation distance was 40 mm.

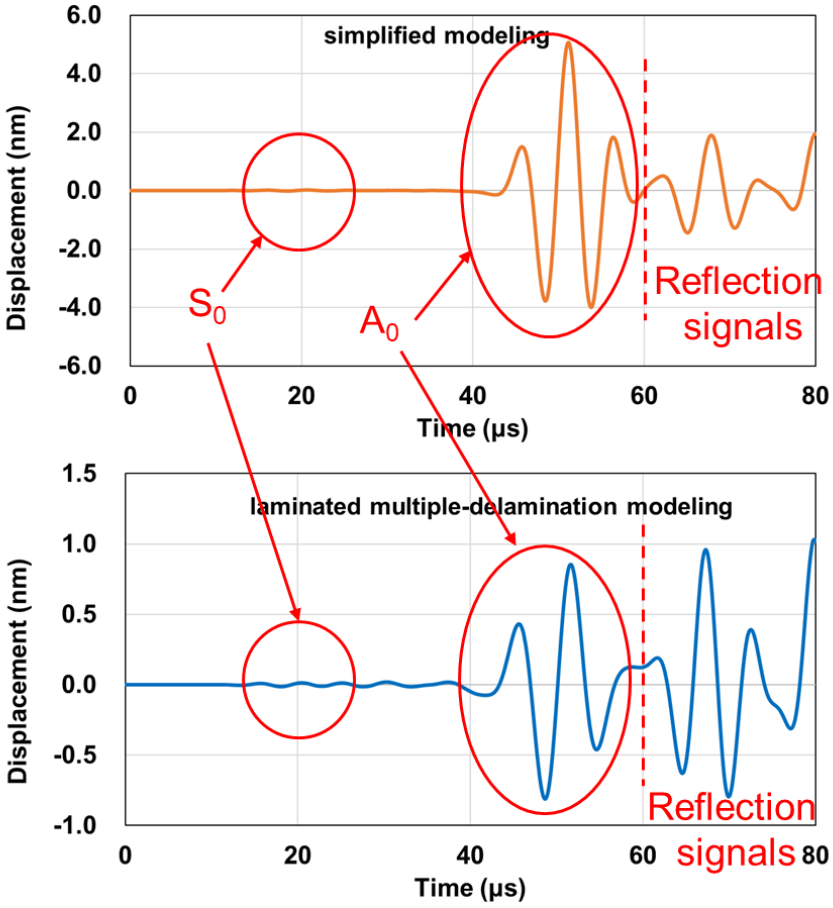

Fig. 2.14. Waveforms at a propagation distance of 60 mm in the simplified and the laminated multiple-delamination models.

Next, the waveforms of the laminated multiple-delamination model and the simplified model were compared at various propagation distances. **Fig. 2.14** shows the waveforms calculated with both models at a propagation distance of 60 mm. In these waveforms, the S_0 mode appears at about 14 μs, the A_0 mode appears at about 38 μs, and the reflection waves from the edges of the plate appear at approximately 60 μs. After removing the reflection signals, the direct propagated waves underwent wavelet transformation, as shown in **Fig. 2.15**. The wavelet transform results

of both models at each propagation distance agree well.

Furthermore, because the displacement of the A_0 mode is much larger than that of the S_0 mode in the waveforms, we determined the propagation time from the maximum peak of the A_0 mode in each wavelet transform result. The obtained propagation times are plotted in **Fig. 2.16**. The propagation time obtained with the simplified model agrees well with that obtained with the multiple-delamination model. In addition, as expected from the dispersion curves in **Fig. 2.1**, the propagation time for three cases are similar in the range from 40 to 220 kHz. These results indicate that the simplified model is appropriate for simulating Lamb wave propagation through impact damage in this frequency range.

2.3.2 Comparison with experimental observation

For a better understanding of Lamb wave propagation behavior, we compared the results calculated using FEM analysis with experimental results, as shown in **Fig. 2.17**.

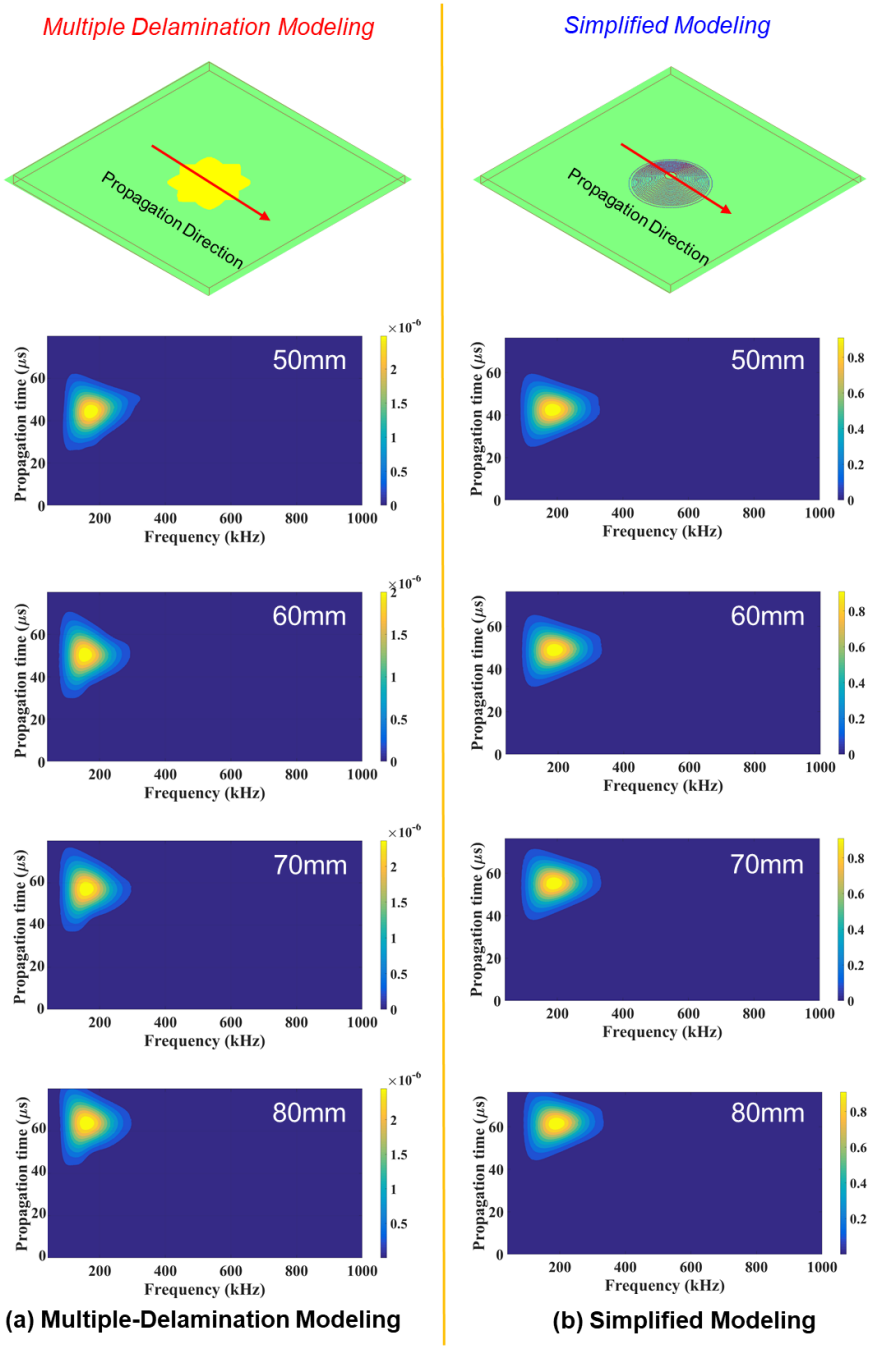

Fig. 2.15. Comparison of wavelet transformation of the propagated waves in the laminated multiple-delamination model and the simplified model at various propagation distances. Input waveform was a three-cycle sinusoidal wave with a Hamming window at 180 kHz.

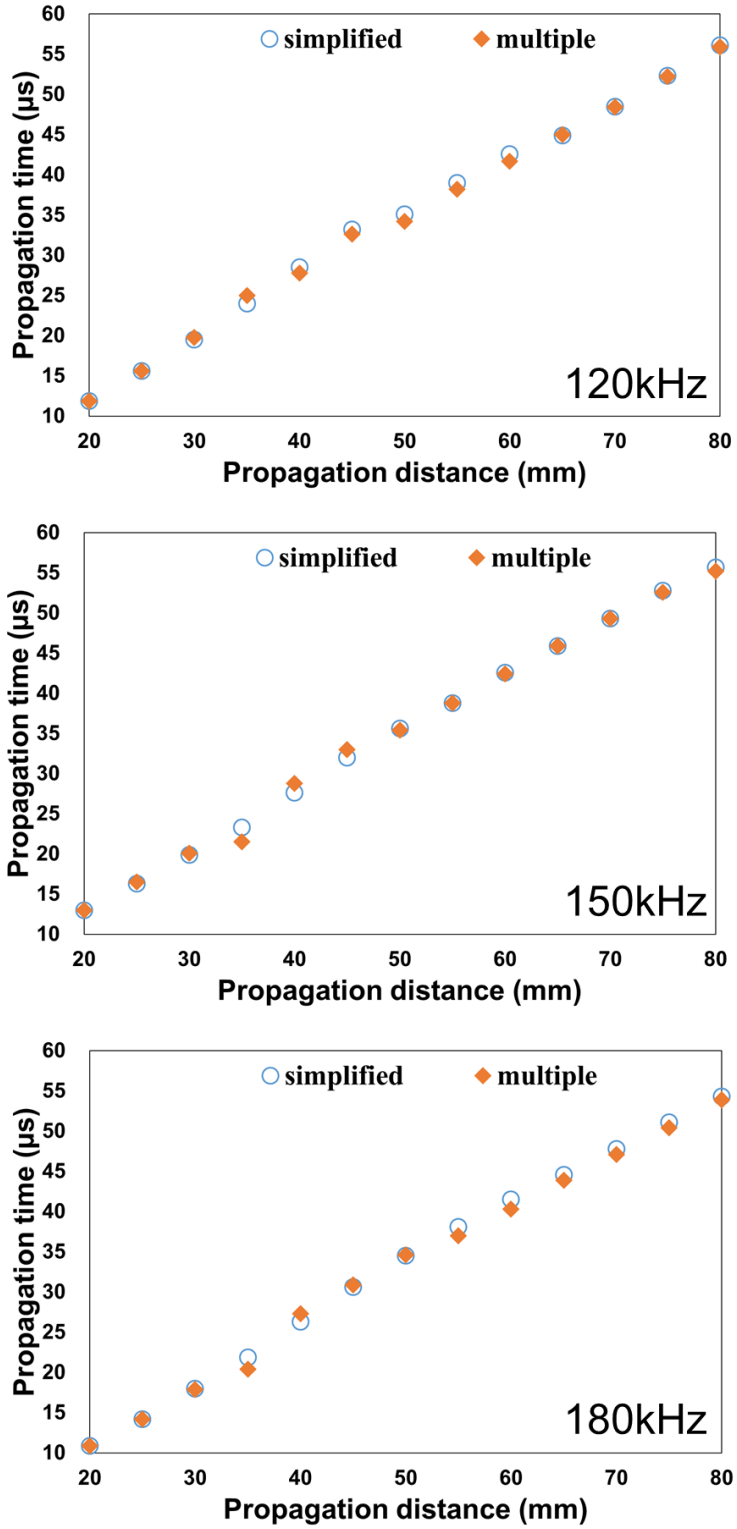

Fig. 2.16. Comparison of propagation times between the multiple-delamination model and the simplified model at different frequencies.

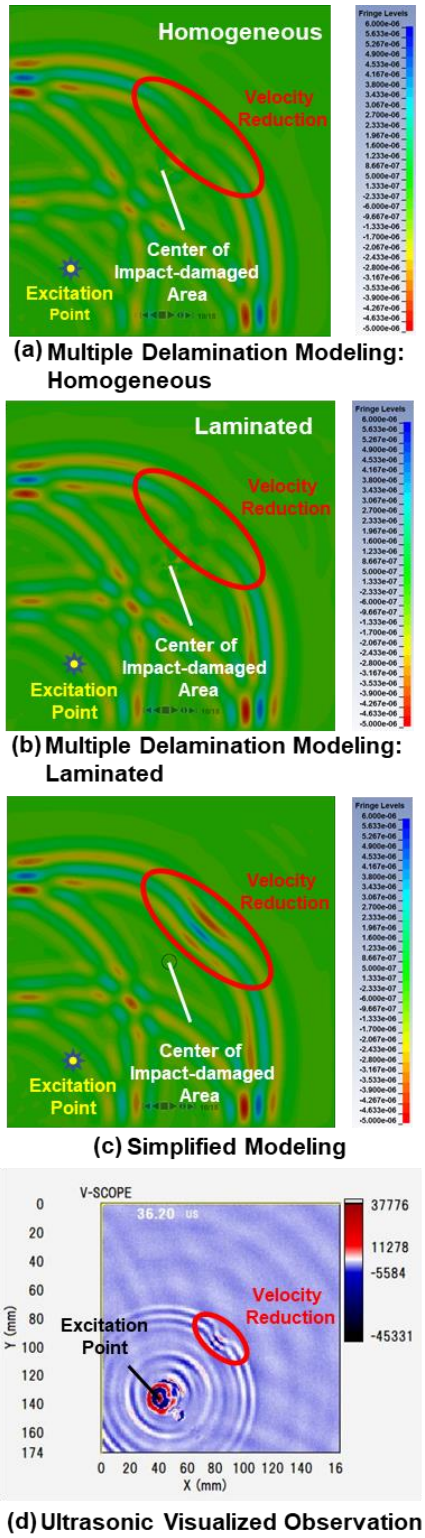

Fig. 2.17. Comparison of Lamb wave propagation behavior calculated using three models and observed by ultrasonic visualization.

In the FEM analysis, the impact-damaged area was at the center of the plate. The plate had a lamination configuration of $[45/0/-45/90]_{3s}$, and dimensions of $90 \times 90 \times 3.4$ mm^3. The mesh size was 0.2 mm in the in-panel direction and 0.14167 mm in the thickness direction. The input waveform in the simulation was a three-cycle sinusoidal wave with a Hamming window at 180 kHz and the *Z*-displacement was plotted.

Fig. 2.17(a) shows the wave propagation calculated with the homogeneous multiple-delamination model and the effective stiffness matrix for a quasi-isotropic laminate listed in **Table 2.1** for the whole homogeneous plate. **Fig. 2.17**(b) shows the wave propagation calculated with the laminated multiple-delamination model. **Fig. 2.17**(c) shows the wave propagation calculated with our simplified model. The propagation behavior of Lamb waves and the change in velocity at the impact-damaged area agree well among these three models. However, the amplitudes of the Lamb waves after passing through the impact-damaged area as found by the multiple-delamination models and our simplified model were different. The amplitude behind the impact-damaged area in the simplified model was larger than those in the multiple-delamination models.

To clarify the reason for the difference in amplitude between models, we obtained the total energy of the propagation wave in the multiple-delamination model calculated using LS-DYNA and found that the energy loss at the delaminated region consisting of double nodes. The energy loss was probably caused by the friction force between the upper and lower surfaces of each

delamination. On the other hand, in the simplified model, because the wave velocity decreased more in the impact-damaged region than in the intact region due to the degradation of the stiffness constants, the propagation direction of the wave changed by refraction when it passed through the low-velocity region. Hence, the impact-damaged region acted as a focusing lens and the amplitude increased behind the impact-damaged area.

Fig. 2.17(d) shows the visualized ultrasonic propagation observation conducted using the Laser Ultrasonic Visualizing Inspector (LUVI) system, which was developed by Tsukuba Technology. The LUVI uses a laser as the signal generator and an AE sensor as the receiver to obtain the wave propagation behavior based on reciprocity theory [38]. The velocity reduction seen in the experimental results was similar to that in all the simulation results. The amplitude was increased when the waves passed through the impact-damaged area, which agrees well with the simulation results of the simplified modeling method. This experimental result shows that the wave energy did not dissipate at the impact-damaged area and, thus, the simplified model is more appropriate than the multiple-delamination models.

For further comparison, the differences in propagation time between the wave in the damaged plate and that in the intact plate were calculated using cross-correlation analysis. The results are plotted as a function of propagation distance in **Fig. 2.18**. Two kinds of modeling method using stiffness constants of T700S/2500 are compared and the experiment results in a CFRP laminate

made of T700SC/2500 are also plotted for comparison.

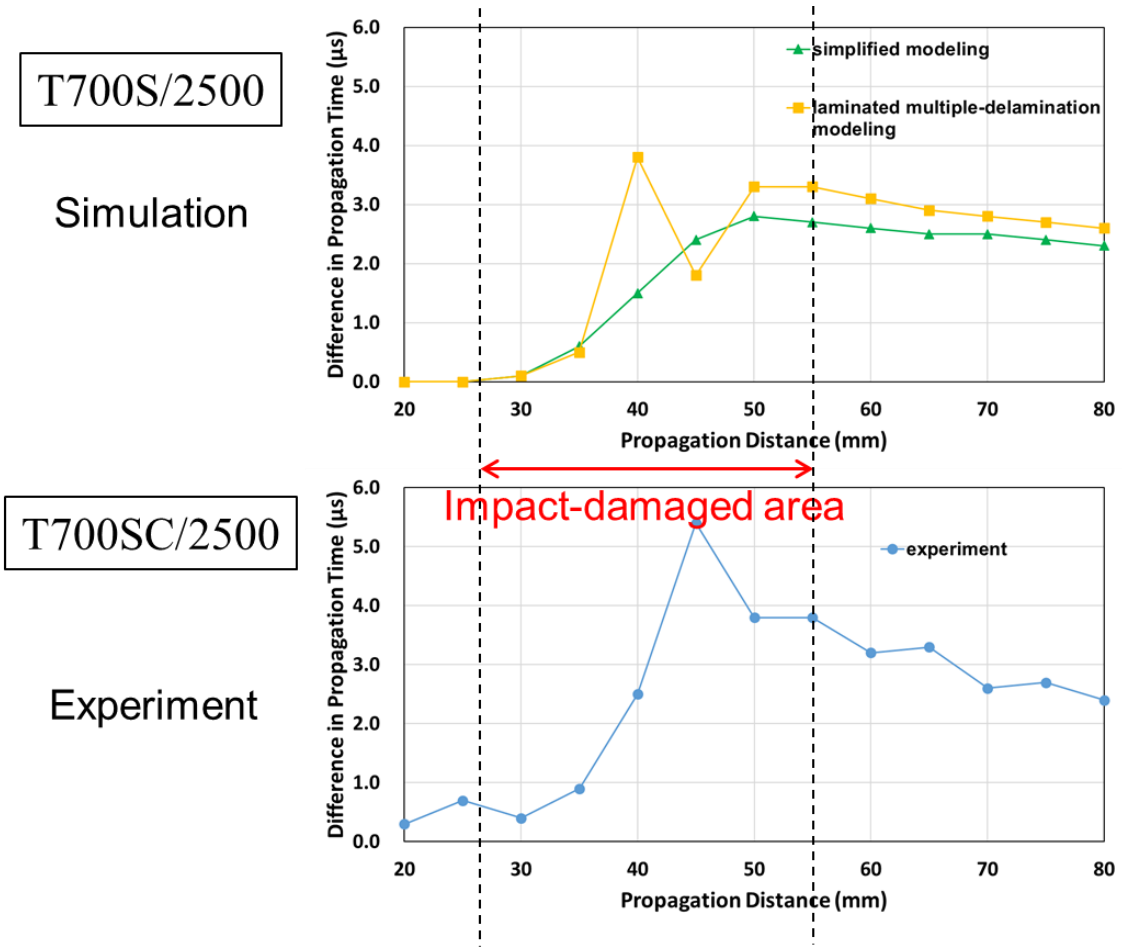

Fig. 2.18. Difference in propagation time between the wave in the damaged plate and that in the intact plate at different propagation distances. The input waveform in the simulation was a three-cycle sinusoidal wave with a Hamming window at 180 kHz.

Before passing through the damaged area (center of impact-damaged area is at 40 mm), the difference in propagation time for all three results is nearly zero. This means that wave

propagation in the damaged plate is the same as that in the intact plate. Around the damaged area, especially at 45 mm, the time delays of the three models do not agree well. However, after passing through the damaged area such as after 60 mm, the time difference becomes stable and has a slow decline for all the three models. The slow decline is mainly because part of the Lamb waves come around the impact-damaged area rather than passing through the impact-damaged area directly when the distance between the measure point and the center of impact-damaged area is long. The wave propagation behaviors after passing through the impact-damaged area is more reliable than that around the impact-damaged area to detect a damage. **Fig. 2.18** shows that the tendency of difference in propagation time after passing through the impact-damaged area agreed among the results of two kinds of modelings and the experiment results of T700SC. This agreement indicates that the simplified modeling method is quantitatively appropriate for modeling the impact damage in Lamb wave propagation simulation in quasi-isotropic composite structures.

2.4 Conclusions

In this chapter, for a practical FEM simulation of Lamb wave propagation, we modeled the impact-damaged area in a CFRP plate as a homogeneous frustum in which the quasi-isotropic stiffness constants are degraded. The dimensions of the damaged region were determined by experimental observation. The degraded stiffness matrix of the impact-damaged region was

determined from the measured velocities of waves and using some assumptions. We showed that the calculated behavior of Lamb wave propagation in the simplified model agrees well with that in the multiple-delamination model and with the experimental results.

The frequencies used in this section ranged from 40 to 220 kHz, which seem suitable for use in SHM systems because the behavior of Lamb waves can be easily interpreted.

This simplified model will be useful for the investigation of suitable configurations of actuators and sensors for SHM systems to detect impact damages of various sizes and locations. The simplified model does not reduce computational cost because total amount of elements is not changed. However, it reduces effort of making a simulation model. To be specific, the modeling time of the simplified model is approximately 1/10 of that of multiple-delamination model used in this thesis. Thus, the simplified model is efficient and useful.

In the subsequent chapter, the applications of this simplified model in a CFRP skin/stringer structure will be discussed.

3 Investigation of guided wave propagation in a complex-shaped CFRP structure

3.1 Introduction

In **Chapter 2**, we discussed the impact damage modeling method of Lamb wave propagation in a quasi-isotropic CFRP laminate plate. In order to verify the applicability of our proposed simplified modeling method in complex-shaped structures, we prepared a CFRP quasi-isotropic skin/hat-shaped stringer structure (T800/3900-2B, $[45/0/-45/90]_s$, both skin and stringer are 1.5 mm in thickness). The value of the skin thickness is typical one of real aircraft fuselage. Therefore, by analyzing this specimen, we can proceed to develop a SHM system applicable to real aircrafts. The stiffness coefficients are given in **Table 3.1**. This skin/hat-shaped stringer structure is also laminated by unidirectional plies. This structure is shown in **Fig. 3.1**(a) and in consideration of its periodicity, one unit of the specimen's dimension is shown in **Fig. 3.1**(b).

Table 3.1. Density and stiffness constants of the CFRP quasi-isotropic skin/hat-shaped stringer structure (T800/3900-2B)

	ρ	C_{11}	C_{12}	C_{13}	C_{33}	C_{44}	C_{66}
Quasi-isotropic	1580	67.45	24.63	4.84	9.22	3.53	22.10

Density in kg/m^3 and stiffness constants in GPa.

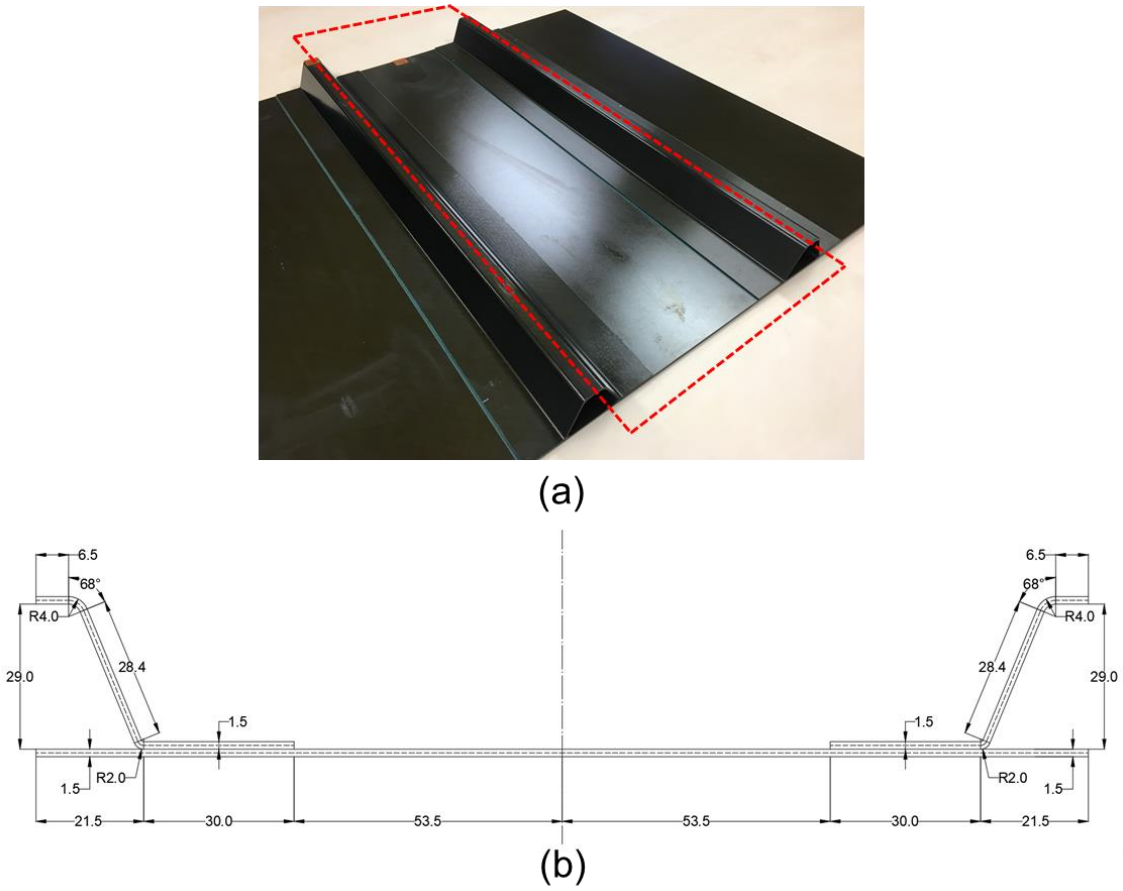

Fig. 3.1. (a) CFRP skin/hat-shaped stringer structure and (b) the dimensions of the cross-section of one unit of the periodical structure.

3.2 Simulation investigation

FEM analysis was performed with the commercial FEM software ComWAVE, as shown in **Fig. 3.2**.

ComWAVE is used to model the CFRP skin/hat-shaped stringer structure instead of LS-DYNA in our research because compared to ComWAVE, it takes a large computing cost with LS-DYNA

to model such a large and complex structure.

ComWAVE is a software application developed by ITOCHU techno-solutions that has an excellent performance in simulating dynamic behaviors, such as ultrasonic propagation in structures or ultrasonic testing in medical science. ComWAVE has the following advantages: 1) it is specialized in ultrasonic simulation; 2) its maximum number of elements can reach 1 billion because it adopts a voxel type finite element method as its analytical solver; 3) it executes analysis by using a computer cluster (memory distributed parallel computing environment) which enables high-speed calculation.

In the current skin/hat-shaped stringer model used for analysis with ComWAVE, the total number of elements is 596 Mega, in which the number of elements of the CFRP skin/hat-shaped stringer model is 45 Mega and the null elements are 551 Mega. In ComWAVE, the whole calculated area is a rectangular parallelepiped, in which the volume occupied by CFRP skin/hat-shaped stringer structure is small, and the portion corresponding to air (null elements) is the majority.

In the fuselage part of a real aircraft, the dimension of CFRP skin/stringer structure is nearly the same as our specimen. In the wing tip part of a real aircraft, the thickness of the skin will be about twice of that of our specimen. In the wing root part of a real aircraft, the thickness of the skin will be about 7 times of that of our specimen, the spacing between the stringers will be about

1.5 times of that of our specimen, and the length of stringers will be twice that of our specimen. Therefore, combining the dimensions in the other two directions and according to the rough estimation, the corresponding number of elements of the skin/hat-shaped stringer model in wing root will be the most among the three actual applications, which is about 900 Mega.

ComWAVE requires about 7 GByte of memory per 100 mega elements. The skin/hat-shaped stringer model in wing root is about 1454 M elements and the total computing cost is about 101 GByte. In addition, the laboratory workstation's installed memory is 256 GBytes and can handle up to 3 billion (3000 M) elements.

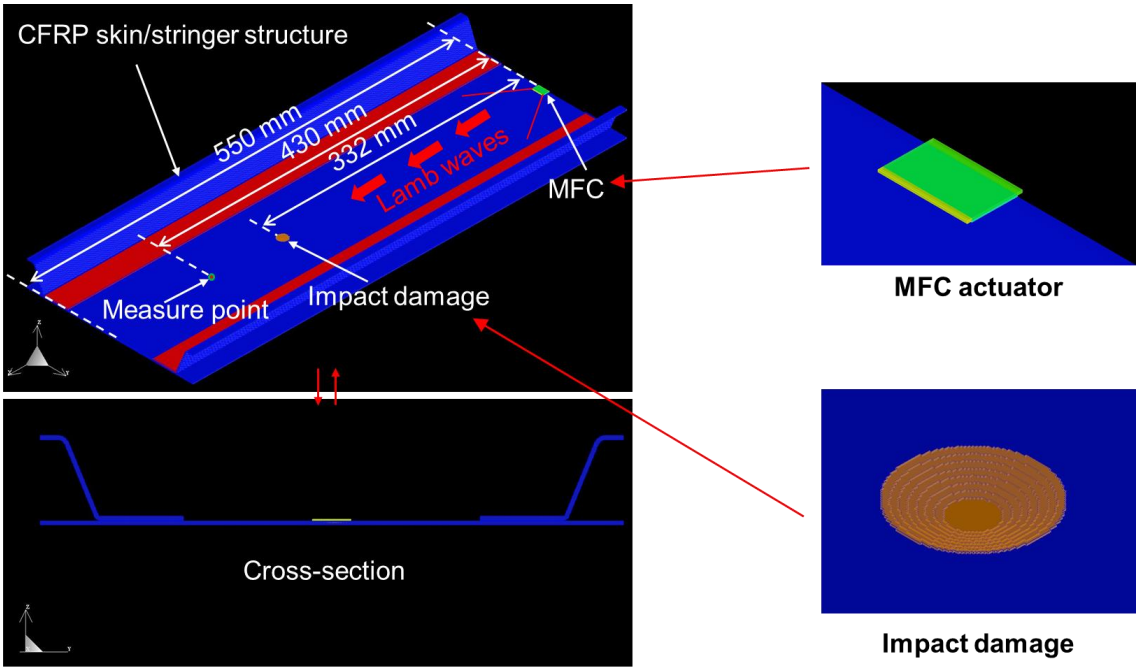

Fig. 3.2. Finite element model of CFRP skin/hat-shaped stringer structure with ComWAVE.

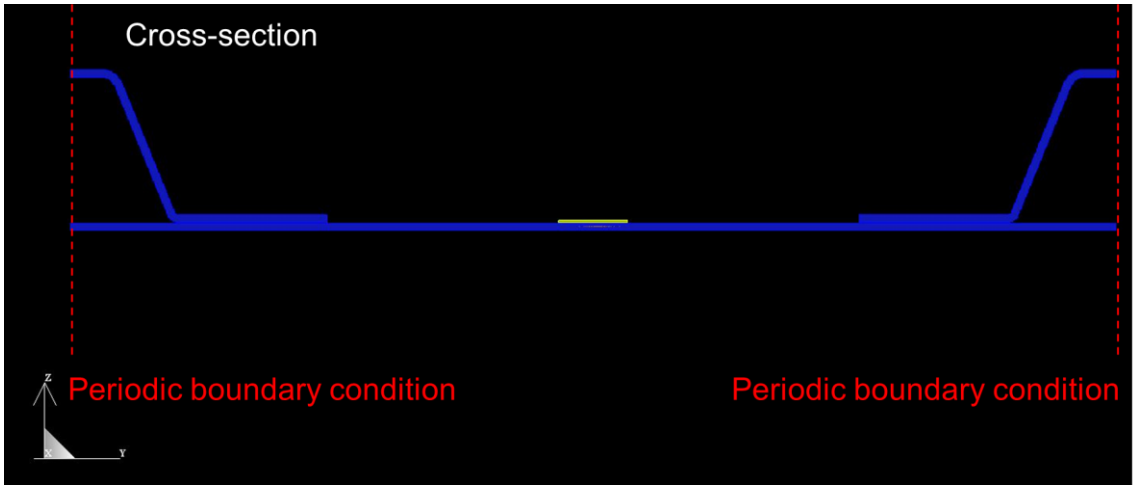

Fig. 3.3. Periodic boundary conditions were applied on both sides.

Since the skin/hat-shaped stringer structure can be assumed as a periodic structure, just one unit area between two adjacent stringers was modeled with periodic boundary conditions on both sides according to the cross-section dimensions in **Fig. 3.1**(b), and the model is shown in **Fig. 3.3**. The parameters in **Table 3.1** were used in the intact area of the CFRP skin/hat-shaped stringer structure. The mesh size was determined by the thickness of one ply in the laminate which is 0.1875 mm. The impact damage was modeled with a simplified modeling method using the dimensions of the real impact damage generated in the experimental investigation. The mesh division is shown in **Fig. 3.4**.

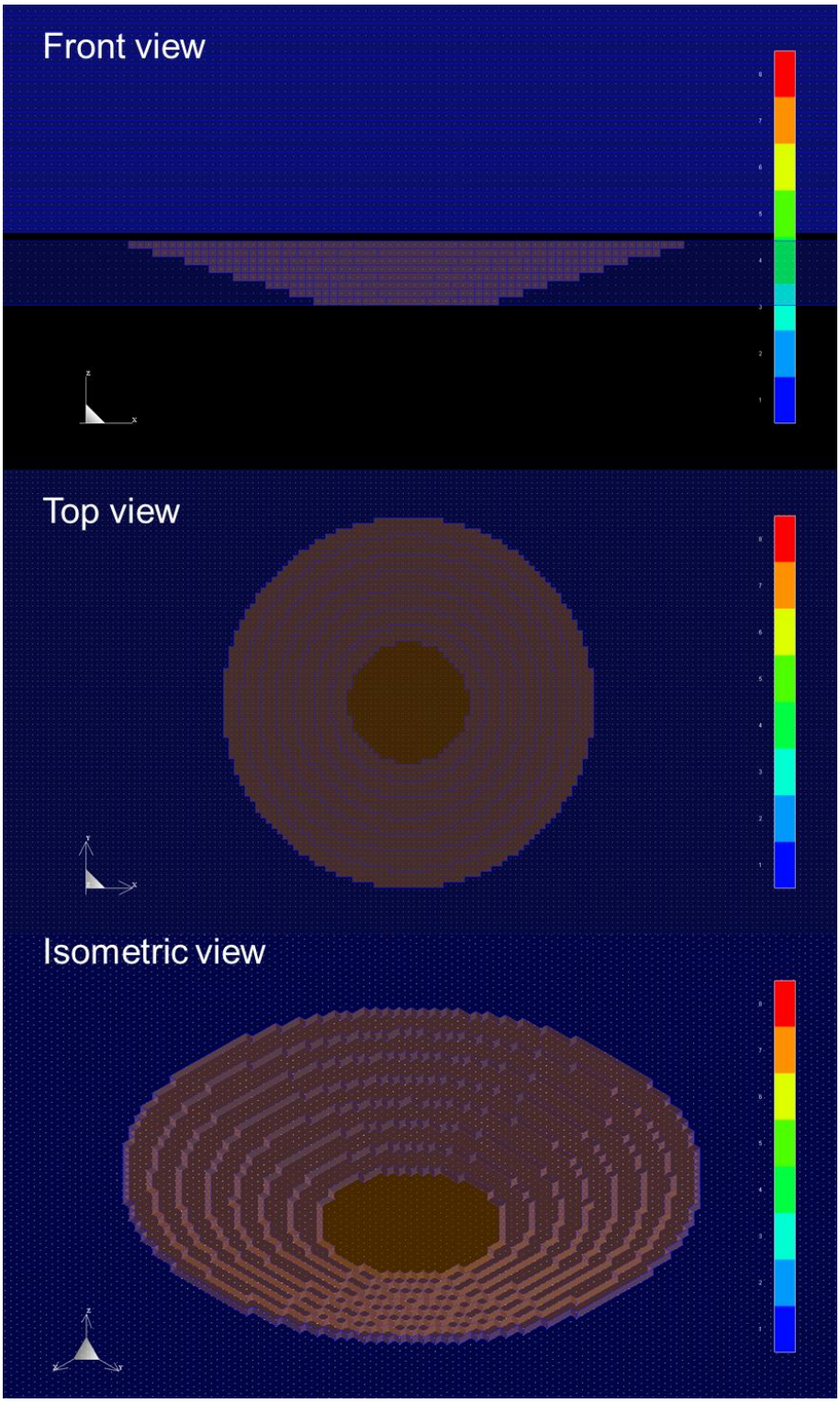

Fig. 3.4. Impact damage in skin/hat-shaped stringer with ComWAVE

The impact-damaged area was quasi-isotropic and approximately 14 mm in diameter. The stiffness of the impact-damaged area was calculated as the same degradation ratio as that of the CFRP laminates case in **Chapter 2**. The recalculated parameters of the impact-damaged area were shown in **Table 3.2**. The adhesive layers between the hat stringer and the skin were also modeled.

The modeling method of the MFC actuator is very important because it has a large effect on the excitation of the wave. Thus, it will be discussed in detail in the next section.

Table 3.2. Density and stiffness constants of the impact-damaged area in the CFRP quasi-isotropic skin/hat-shaped stringer structure (T800/3900-2B)

	ρ	C_{11}	C_{12}	C_{13}	C_{33}	C_{44}	C_{66}
Impact-damaged area	1580	49.77	18.17	0	9.22	2.10	16.31

Density in kg/m^3 and stiffness constants in GPa.

3.3 MFC actuator modeling method

3.3.1 MFC

In order to properly model the propagation behaviors of the Lamb waves generated by the MFC actuator, the mechanism of MFCs should be studied first.

The Macro Fiber Composite (MFC) actuator is a flexible actuator that consists of thin

rectangular piezoelectric fibers sandwiched between layers of epoxy adhesive and polyimide films with electrodes (see **Fig. 3.5**). MFCs will bend or distort materials to counteract or generate vibrations under the circumstance voltage applied. It has broad band characteristics and directional excitation of ultrasonic waves. Furthermore, MFCs have a high flexibility and reliability with a comparatively low cost.

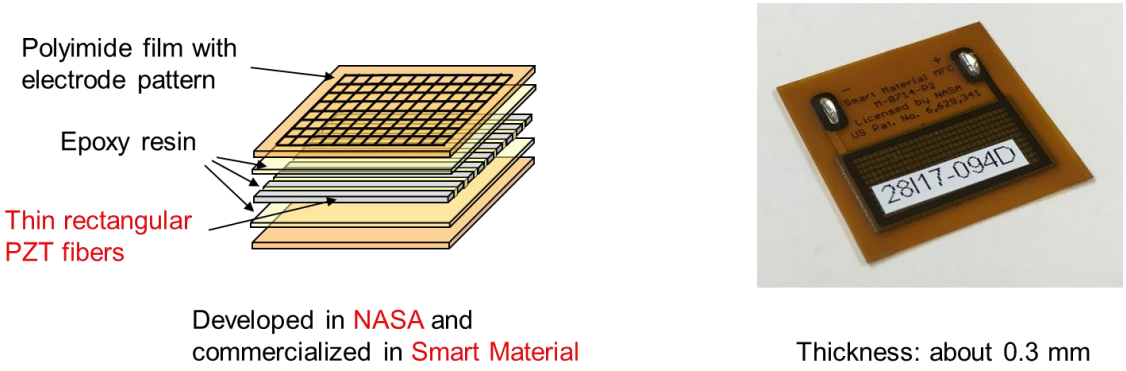

Fig. 3.5. Macro Fiber Composite (MFC).

3.3.2 MFC actuator modeling method with LS-DYNA

Since MFCs generate vibrations by the piezoelectric fibers in the form of volume force, it is reasonable to use volume force or similar vibration excitation form in the simulation to make the MFC actuator model more reliable. Thus, we can model the generation of vibrations with LS-DYNA through thermal expansion, which generates vibrations also in the form of volume force.

3.3.3 MFC actuator modeling method with ComWAVE

However, if we use ComWAVE to conduct the simulation, we cannot easily model the vibrations of MFCs because ComWAVE has no corresponding module capable of generating vibrations in the form of volume force.

For this reason, we proposed a new method to model the MFC actuator with ComWAVE.

First, we made a cross-section observation of a real MFC and found the thickness of the PZT layer is approximately twice that of both epoxy layers in total, as shown in **Fig. 3.6**. We then constructed an MFC actuator model, which consists of a PZT layer and an epoxy layer, of equal thickness to the real MFC, as shown in **Fig. 3.7**. In this figure, the MFC actuator is modeled as the green part in the white box. The ultrasonic waves were then excited by the application of oscillation from two rigid bodies attached on both sides of the PZT layer.

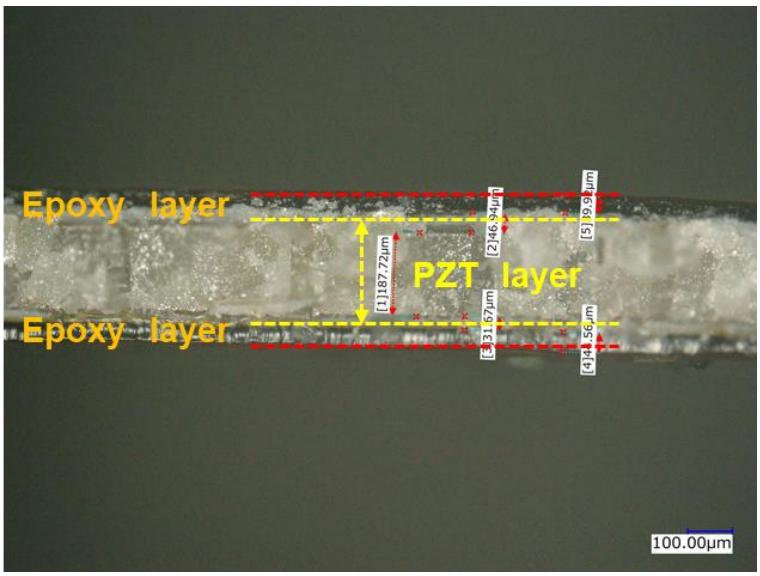

Fig. 3.6. Cross-section observation of MFC.

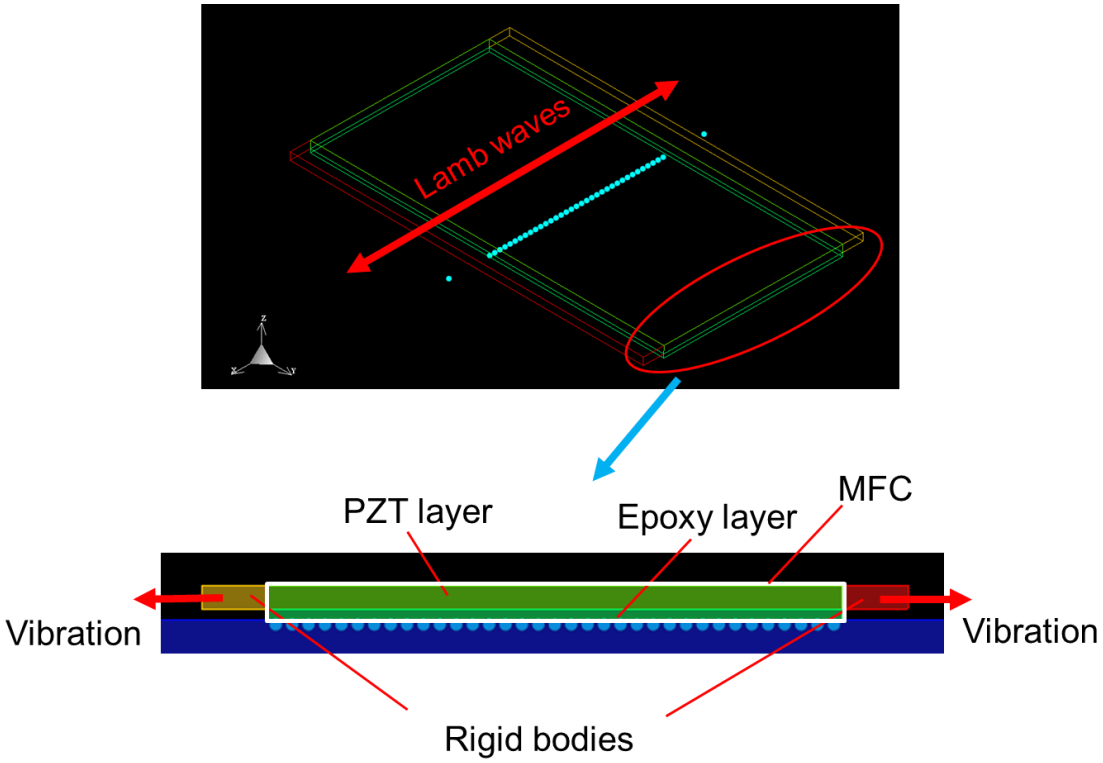

Fig. 3.7. Finite element model of the MFC actuator.

3.3.4 Verification of the MFC actuator modeling method with ComWAVE

To verify the validity of the proposed new modeling method of MFC actuator, we constructed simulation models with LS-DYNA and ComWAVE, respectively. In either case, the MFC actuator was attached to the center of a CFRP laminate, as shown in **Fig 3.8**. The MFC actuators in both cases are of the same dimension and stiffness. The difference between the two cases lies in the ultrasonic excitation method of the MFC: the proposed rigid bodies vibration method was applied in ComWAVE, while the thermal expansion method was applied in LS-DYNA. Both two cases

used a three-cycle sinusoidal wave with a Hamming window at 180 kHz as the input wave. The displacement in the direction of Lamb wave propagation (x-direction) of typical nodes from A to G (see **Fig. 3.9**) was then recorded. The normalized results are shown in **Fig. 3.10**, and the waveforms of each node between the two methods (ComWAVE and LS-DYNA) were in good agreement.

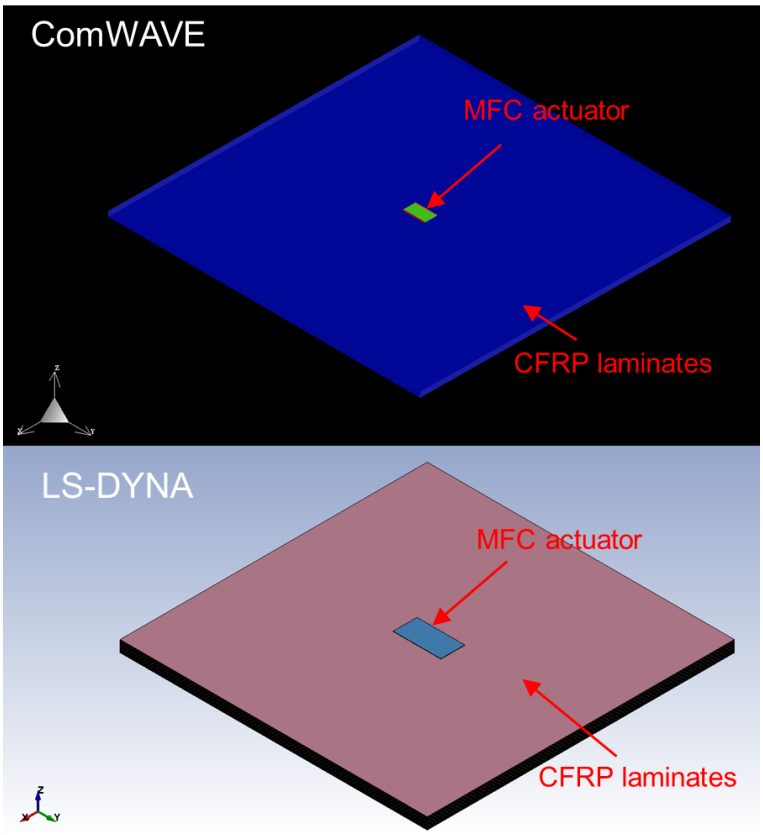

Fig. 3.8. Comparison between the two kinds of MFC modeling method.

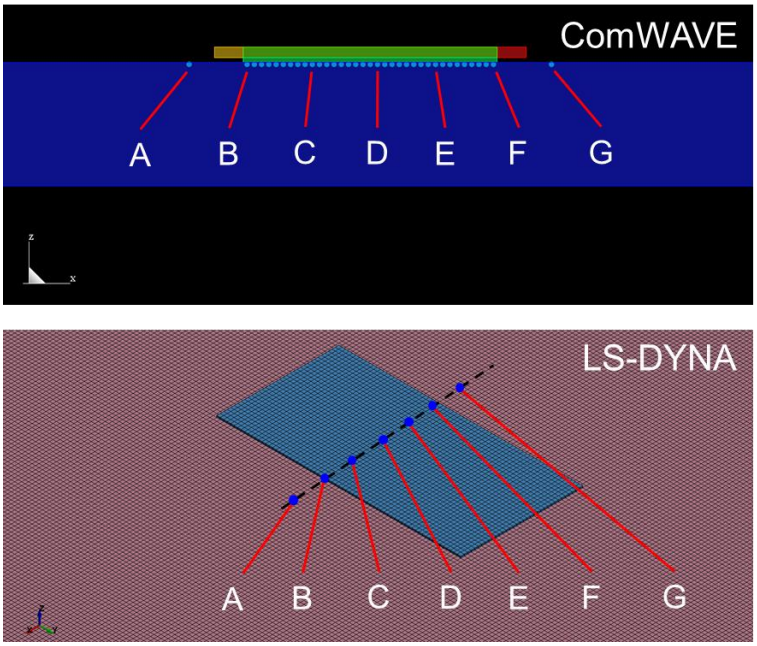

Fig. 3.9. Wave acquisition points with ComWAVE and LS-DYNA.

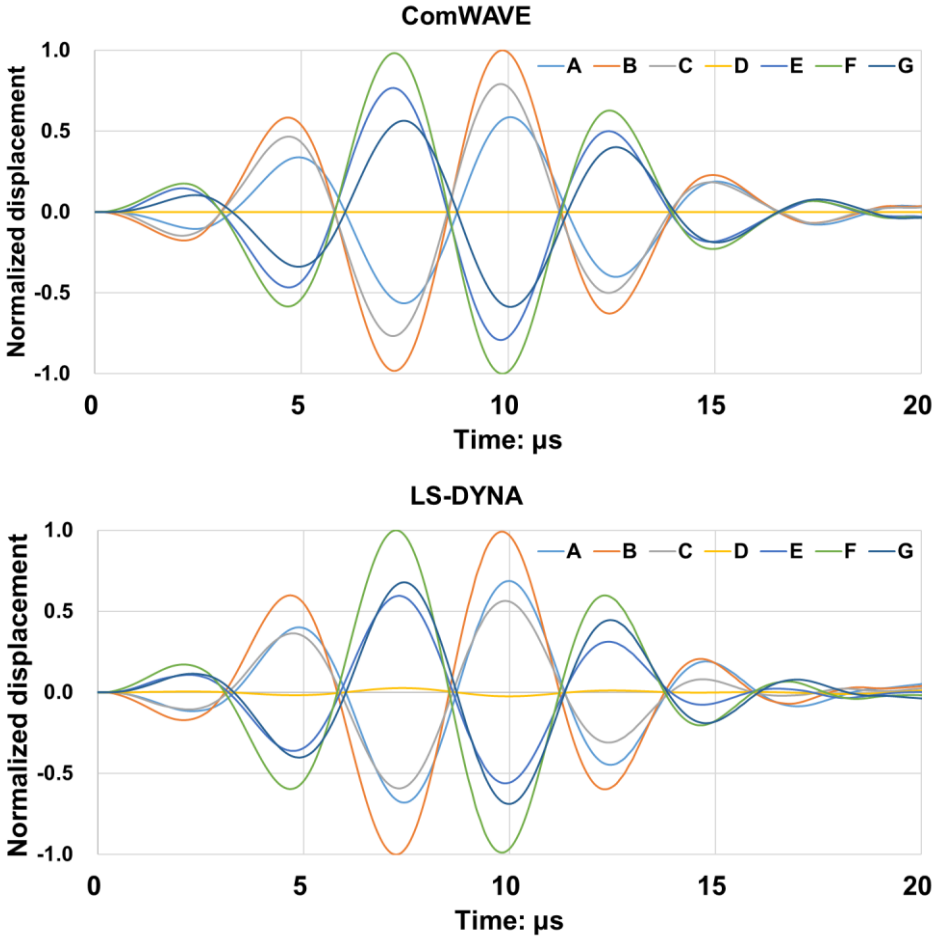

Fig. 3.10. Waveforms of typical nodes A ~ G between the two kinds of MFC modeling method.

More comparisons are conducted to verify this modeling method. **Fig. 3.11** shows the normalized displacement of each node at typical times. Six representative times of input waveform during excitation period are chosen. The agreement of the results shown in **Fig. 3.11** implies that our MFC actuator model with ComWAVE is appropriate to simulate the excitation of ultrasonic waves.

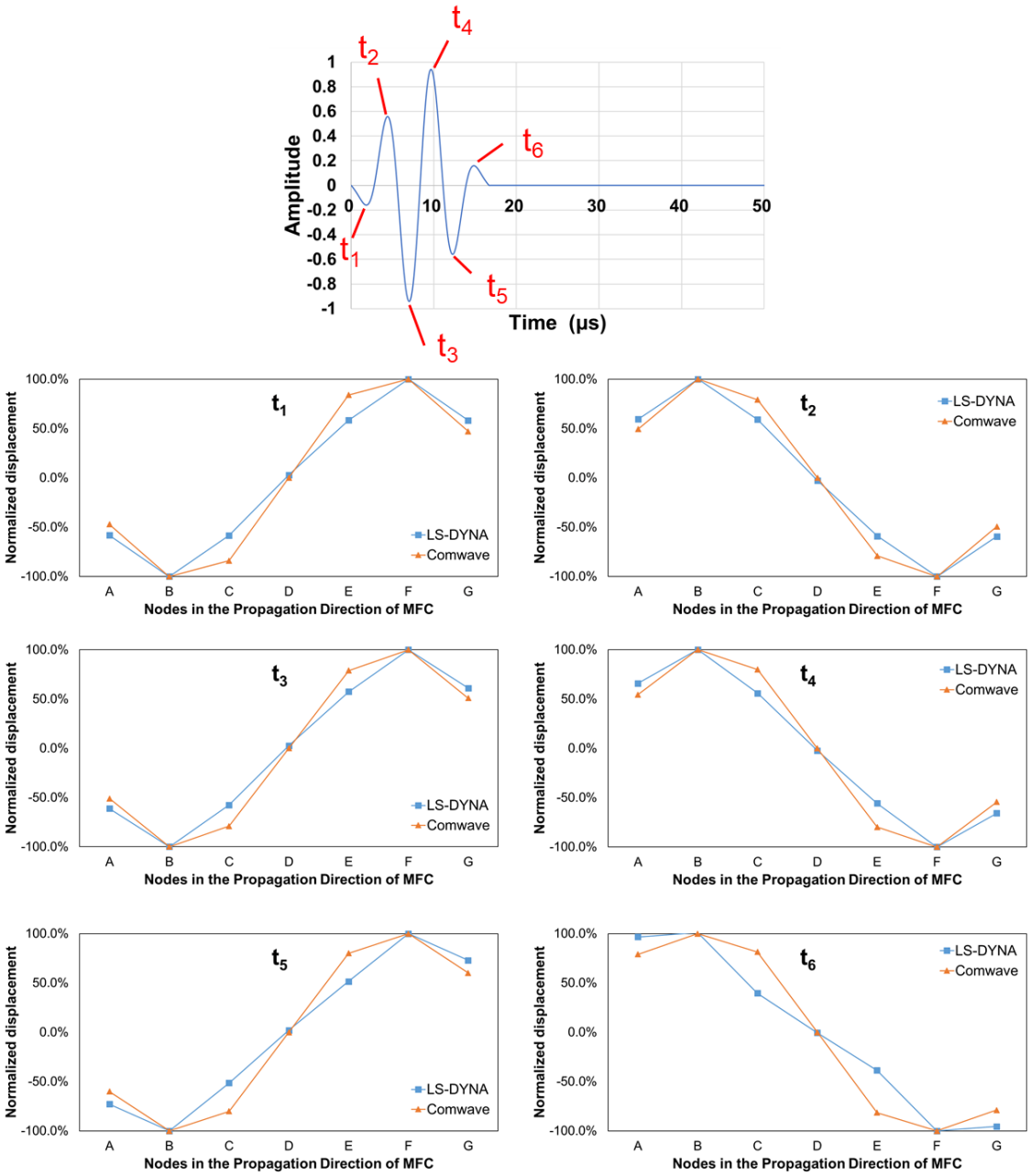

Fig. 3.11. Normalized displacement of nodes A~G at typical moments of the input waveform.

3.4 Experimental investigation

For the verification of the FEM simulation of the CFRP skin/hat-shaped stringer structure, an

experimental measurement was then conducted. Before that, impact testing was completed in SUBARU (see **Fig. 3.12**).

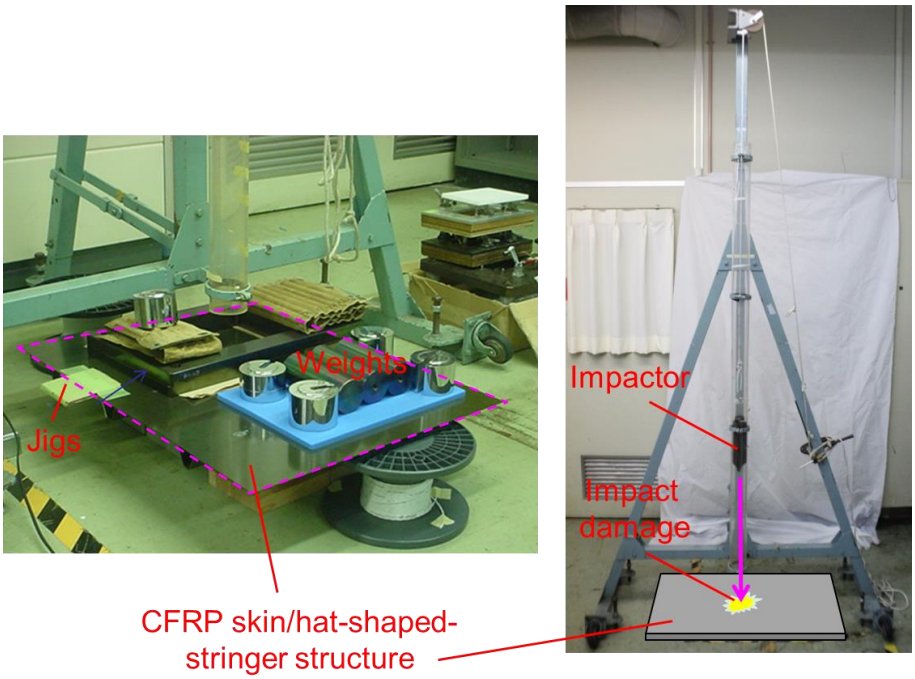

Fig. 3.12. Impact testing in SUBARU.

The impact damage was generated on the back of the skin plate. **Fig. 3.13** shows the detail of the impact-damaged area.

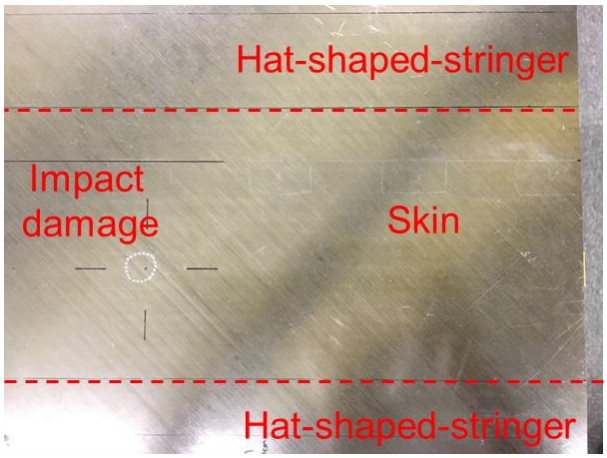

Fig. 3.13. Impact damage details.

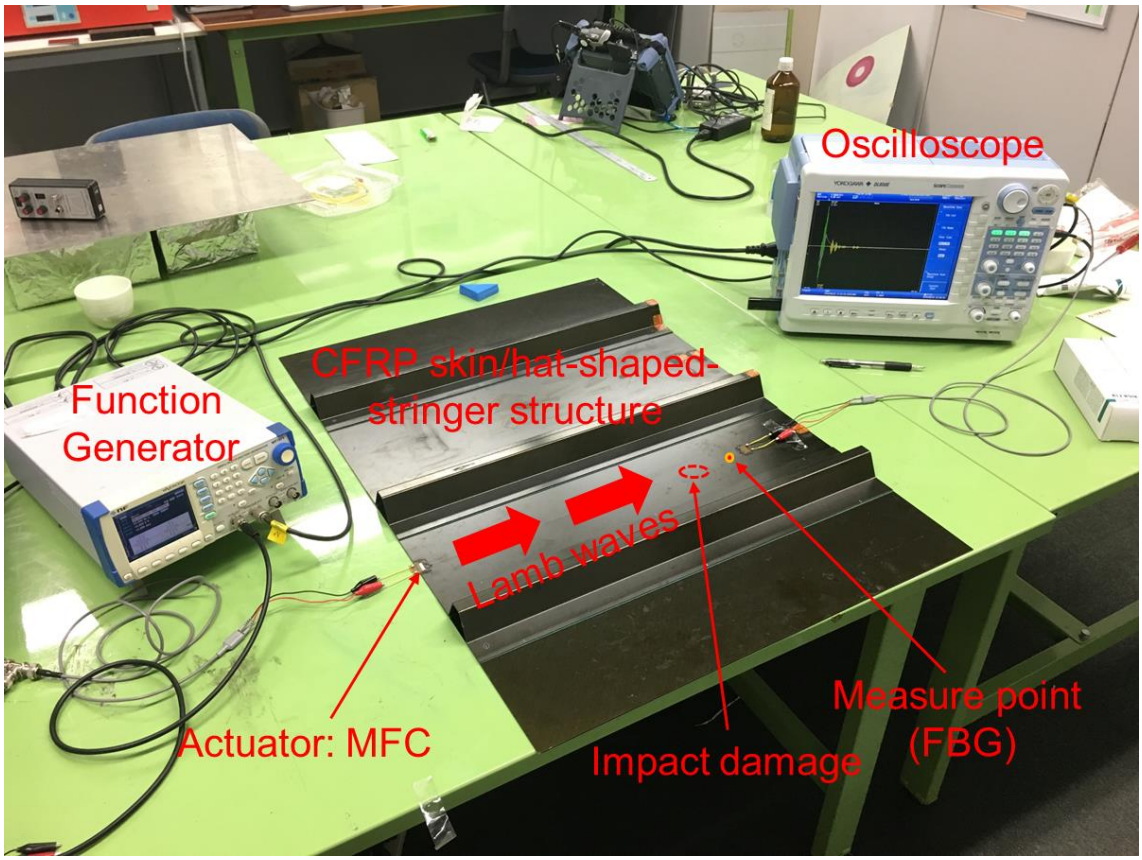

Fig. 3.14. Ultrasonic experimental setup in the CFRP skin/hat-shaped stringer structure.

In the ultrasonic experimental setup (see **Fig. 3.14**), we used a multifunction generator (NF WF1973) to generate an electrical signal and MFC as the actuator to convert the electrical signal into strain. The input wave to the MFC was a three-cycle sinusoidal wave with a Hamming window at 100 kHz or 180 kHz.

Meanwhile, a fiber Bragg grating (FBG) was used as the receiver and an oscilloscope (YOKOGAWA DL850E) was used to record the waveform.

The FBG sensor is a type of optical fiber sensor, constructed in a short segment that reflects particular wavelengths of light and transmits others [39]. The principle of the FBG sensor can be explained using **Fig. 3.15**: when a broadband light is input into the sensor, the optical filter inside the fiber would reflect a wave whose wavelength is λ_B,

$$\lambda_B = 2n\Lambda, \tag{17}$$

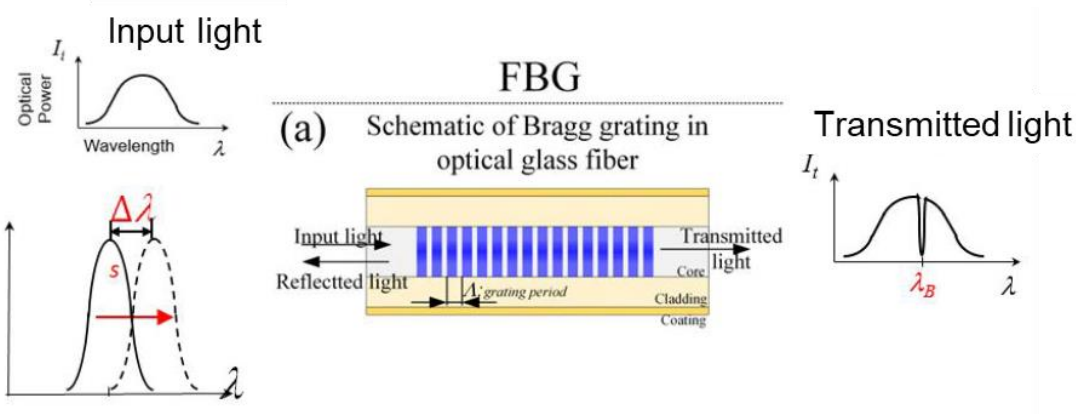

Fig. 3.15. Principle of an FBG sensor.

In **Eq. (17)**, the grating period is Λ, dictating which wavelengths pass or get reflected, and n is the core average refractive index. External factors such as heat and vibration will cause a shift in the wavelength of the reflective light; these variations can then be translated into physical engineering units such as amplitude, strain and temperature as all FBG sensors are based on measuring within a selected wavelength range. Unlike conventional electrical sensors, FBG sensors are non-conductive, electrically passive and immune to electromagnetic interference, making them a safe and reliable alternative to MFC sensors.

3.5 Results

The received strain waves were compared between the experimental results and the simulation results. The comparison results at 180 kHz are shown in **Fig. 3.16**.

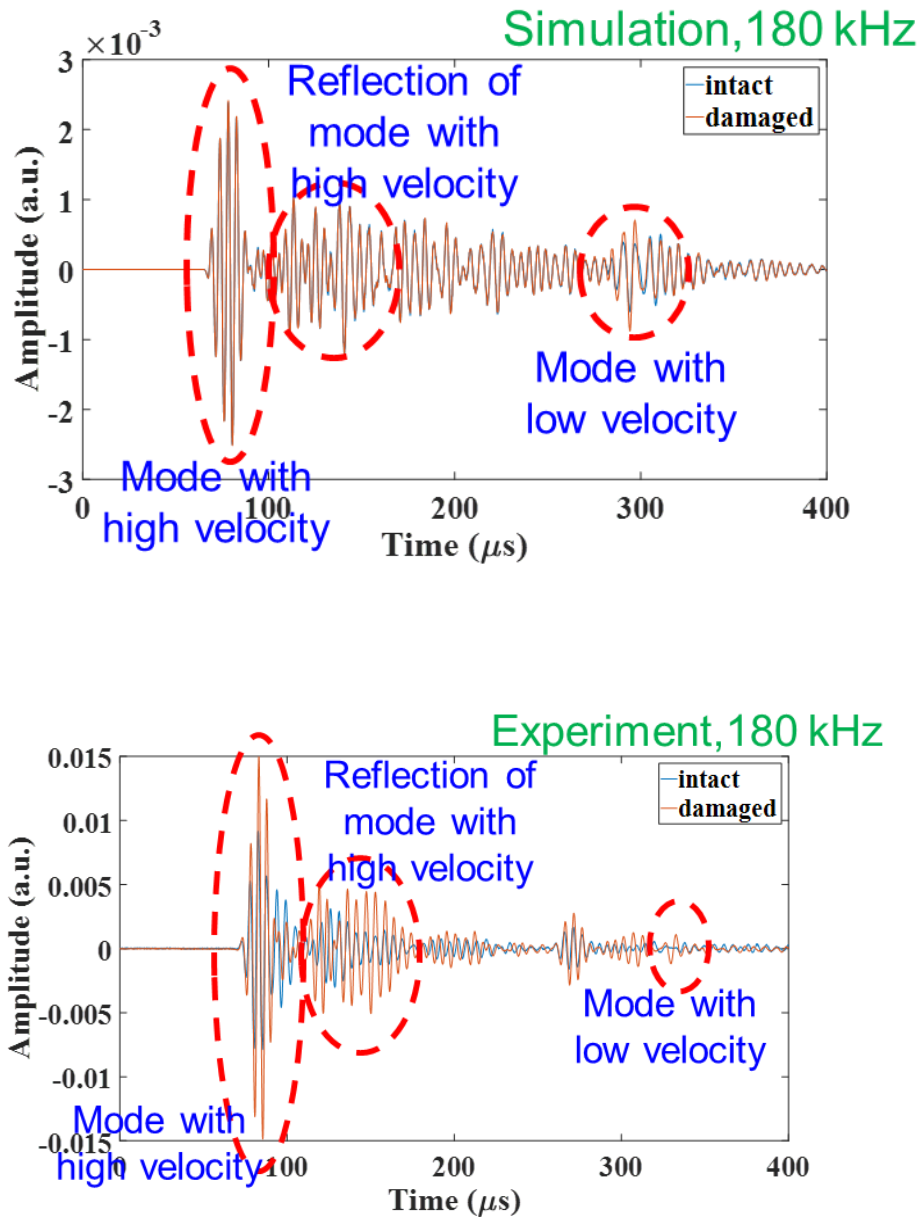

Fig. 3.16. Comparison of waveforms between simulation results and experiment results at 180 kHz with a propagation distance of 430 mm.

The comparison results at 100 kHz is shown in **Fig. 3.17**.

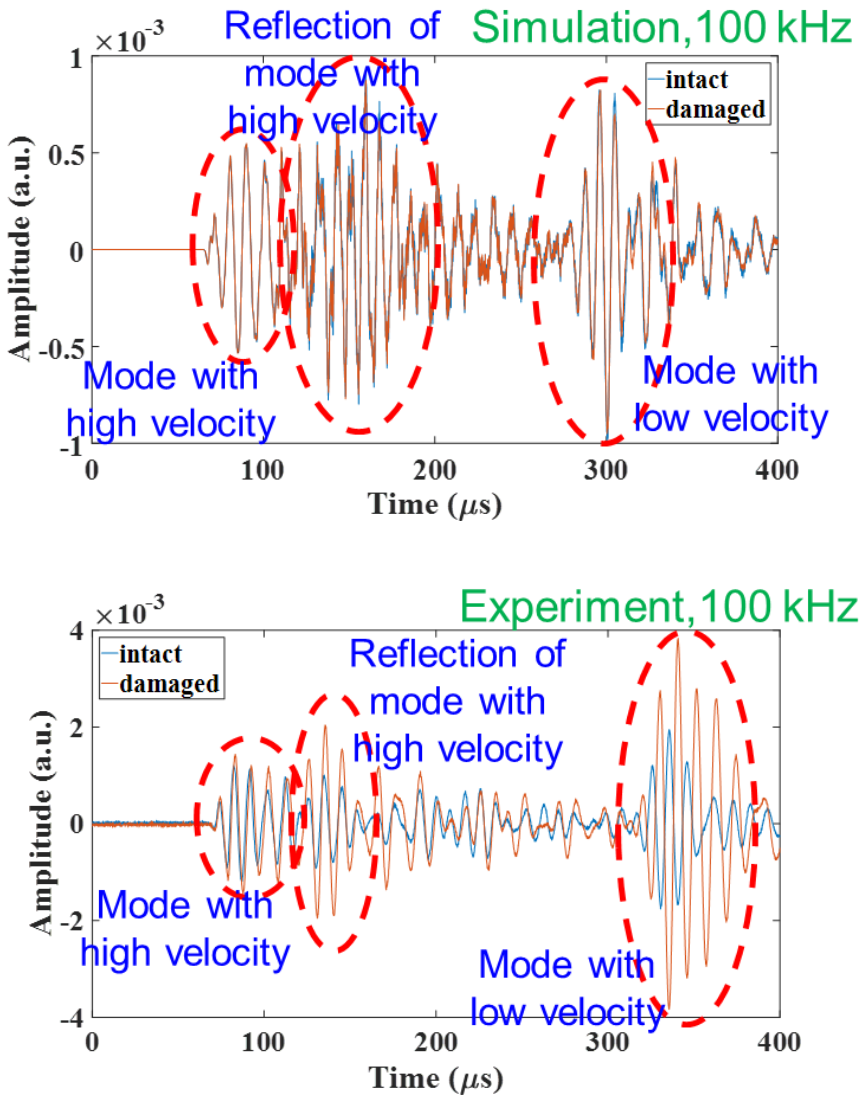

Fig. 3.17. Comparison of waveforms between simulation results and experiment results at 100 kHz with a propagation distance of 430 mm.

3.6 Discussion

There are three domain modes in both cases in **Fig. 3.16** and **Fig. 3.17**, they are the mode with high velocity, the reflection of mode with high velocity, and the mode with low velocity, respectively. The reflected waves are generated at the stringers on both sides (see **Fig. 3.18**).

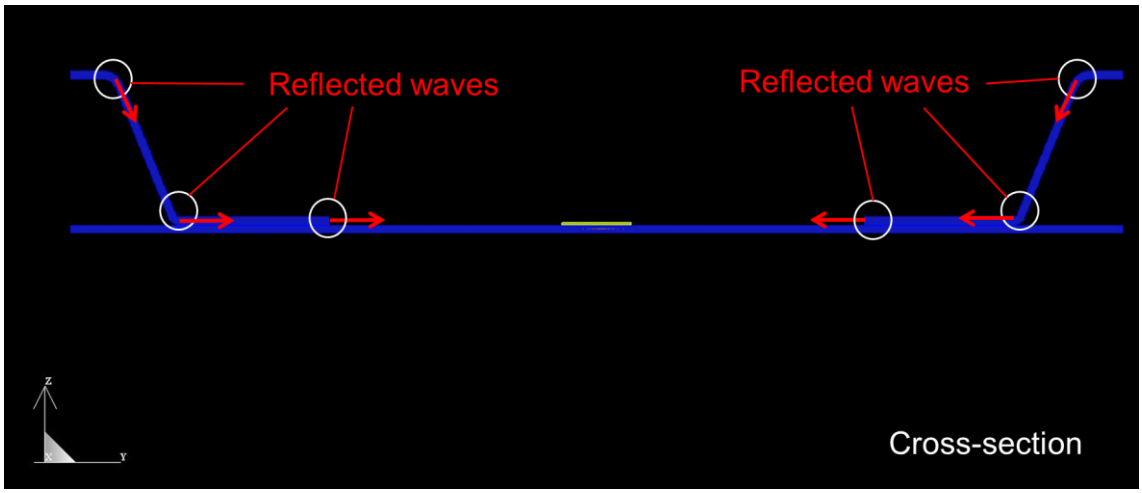

Fig. 3.18. Reflected waves in skin/hat-shaped stringer structure.

It is found that there is a delay between the intact case and the damaged case in both experimental results around the mode with low velocity. However, in the simulation results, it seems that the delay is not as large as that in the experimental results. For verification, we plotted the visualized wave propagation behavior at 100 kHz in the simulation in **Fig. 3.19**. This figure shows the existence of delay, and also shows that the reflected waves generated at stringers are strong.

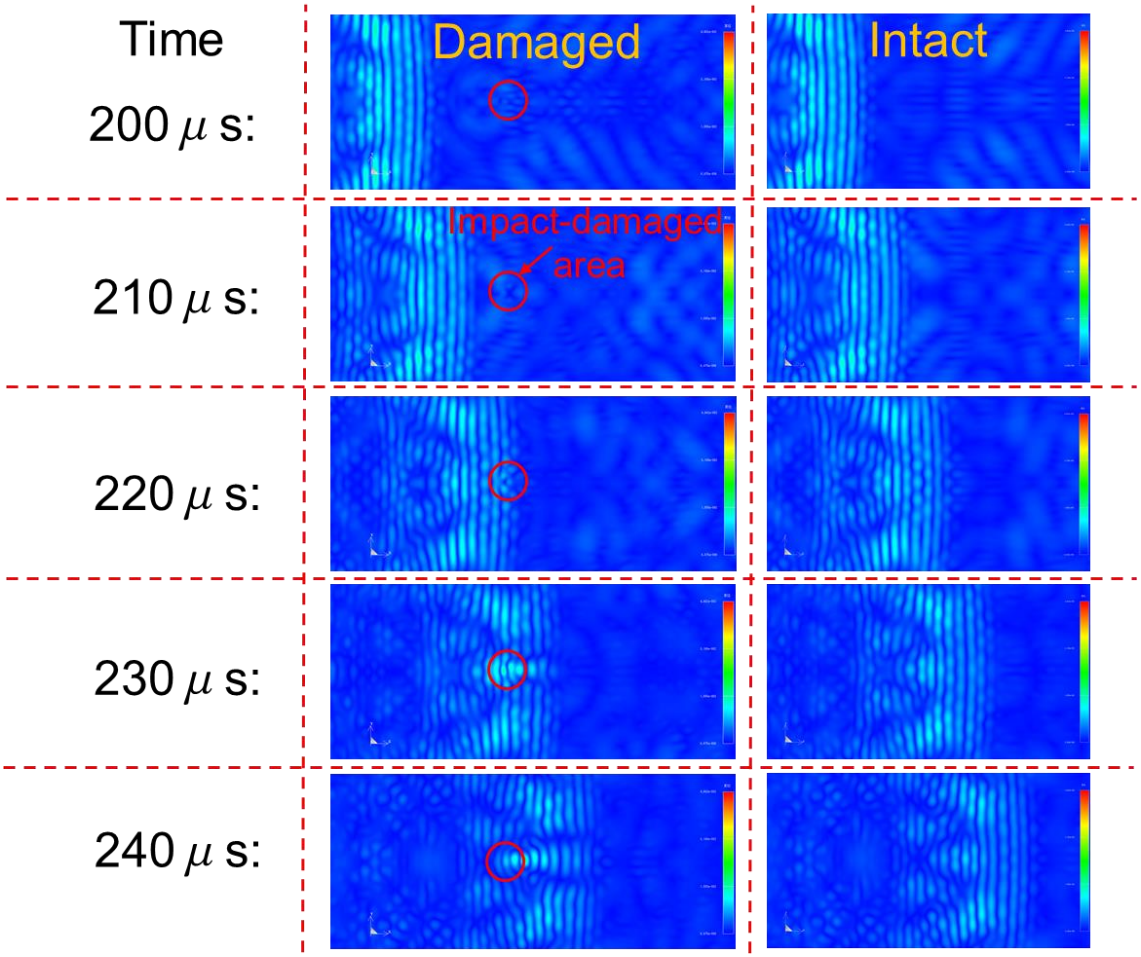

Fig. 3.19. Wave propagation behavior at 100 kHz.

Fig. 3.16 and **Fig. 3.17** indicate that the simulated waveforms agree with the measured waveforms in experiments from the viewpoint of the appearance and relative amplitude of multiple modes in the Lamb waves at both 100 kHz and 180 kHz. The wave packets around 300 μs, which is the mode with low velocity, seem to have larger differences between intact and damaged cases than other wave packets.

Thus, we further examined the waveforms around 300 μs in both the simulation and experiment results of 180 kHz, and found that there exists a time difference (delay) in the propagation time at input frequencies of both 100 kHz and 180 kHz (see **Fig. 3.20**). We only examined the waveforms at 100 kHz because the amplitude of the mode with low velocity in the experiment results is very small at 180 kHz and it is difficult to find the delay clearly.

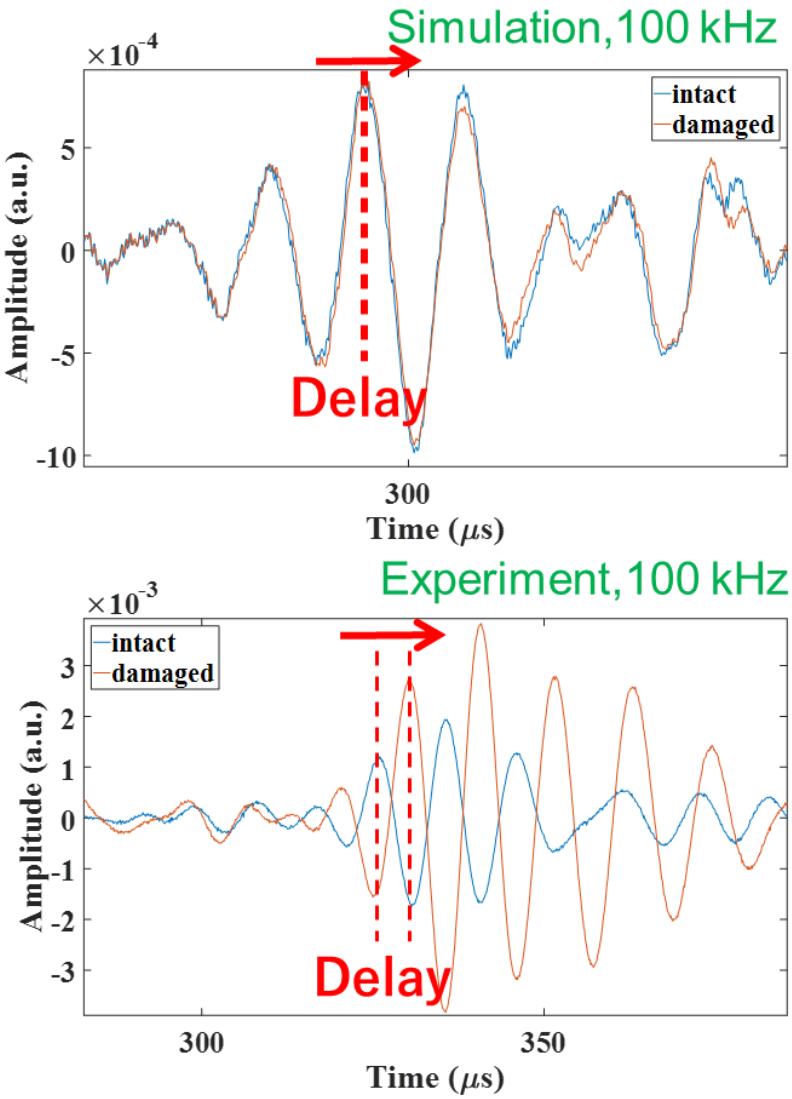

Fig. 3.20. Close-up view of the waveforms at 100 kHz in **Fig. 3.16** and **Fig. 3.17** around 300 μs.

At 100 kHz, though the time delay exists in both the simulation and experiment results, there are some mismatches between them.

Firstly, the propagation time of the mode with low velocity is different between the experiment and simulation. It seems that there is a problem with the value of the stiffness constants used in the simulation. The stiffness constant of T800/3900-2B was provided by the collaborative research partner SUBARU through a literature survey. This may differ from the actual parameters of the skin/hat-shaped stringer structure.

Secondly, the time of delay is different between the experiment and simulation. In order to investigate whether this mismatch is due to the wave propagation at long propagation distance, we conducted another two simulation as shown in **Fig. 3.21** and **Fig. 3.22**.

In **Fig. 3.21**, we conducted the simulation using the same simulation setup of the skin/stringer structure with the input frequency at 100 kHz, but we measured the waveform at the propagation distance of 360 mm, which is a shorter propagation distance than 430 mm shown in Fig. 3.2. The magnified waveform results show that the delay exists around 250 μs and it is more obvious than that of the case with a longer propagation distance. The main reason may be the slow reduction in the time delay with an increase in the distance from the impact damage as mentioned in **Chapter 2**. When the distance between the measure point and the center of impact-damaged area is long, part of the Lamb waves come around the impact-damaged area rather than passing through

the impact-damaged area directly.

In **Fig. 3.22**, we conducted the simulation using the same simulation setup of skin/stringer structure with input frequency at 100 kHz, but the impact damage's location is set at 100 mm and we measured the waveform at the propagation distance of 120 mm. The waveform results show an obvious delay in propagation time of mode with low velocity in the damaged case, compared with that of intact case. This delay does not seem to be as large as the delay of the experiment results in **Fig. 3.17**. However, it is similar to the delay in **Fig. 3.21** even these two cases have different propagation distance.

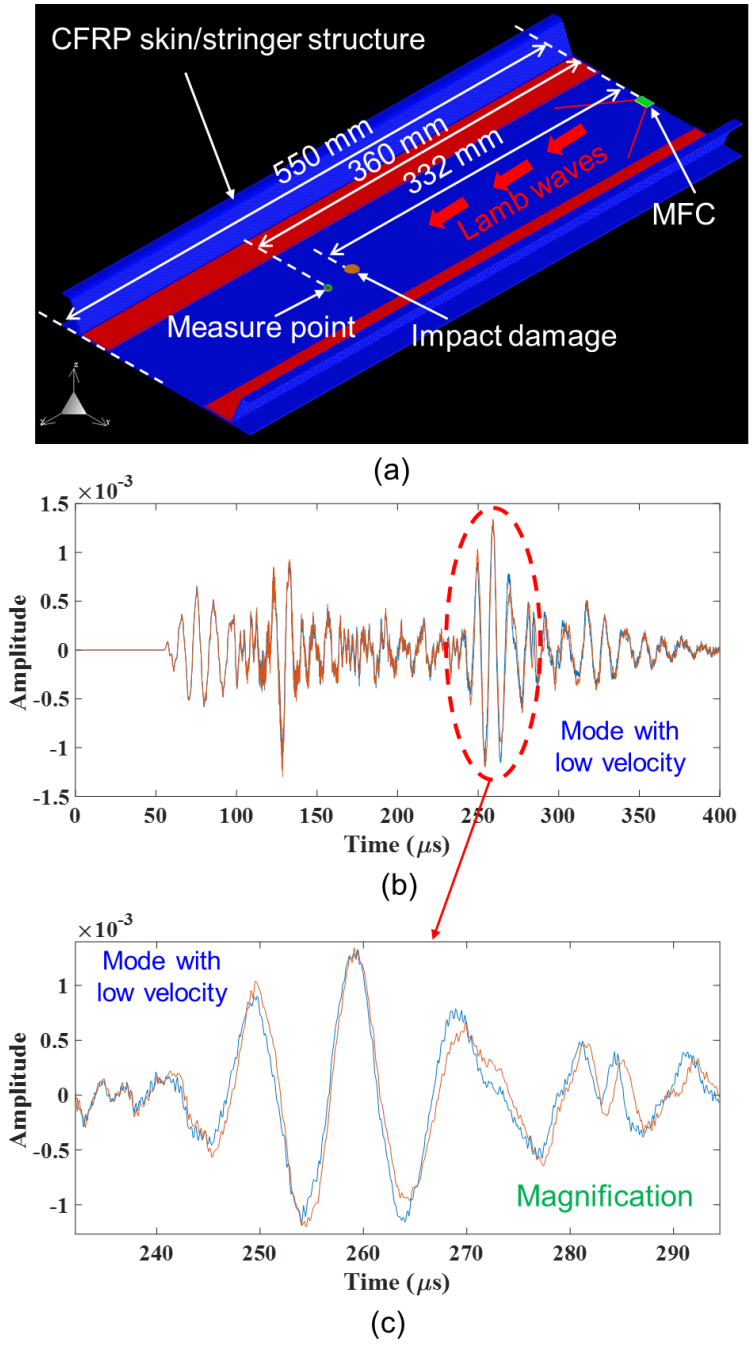

Fig. 3.21. (a) Simulation setup, (b) waveforms of propagated waves between damaged and intact cases and (c) close-up view of waveforms around 250 μs.

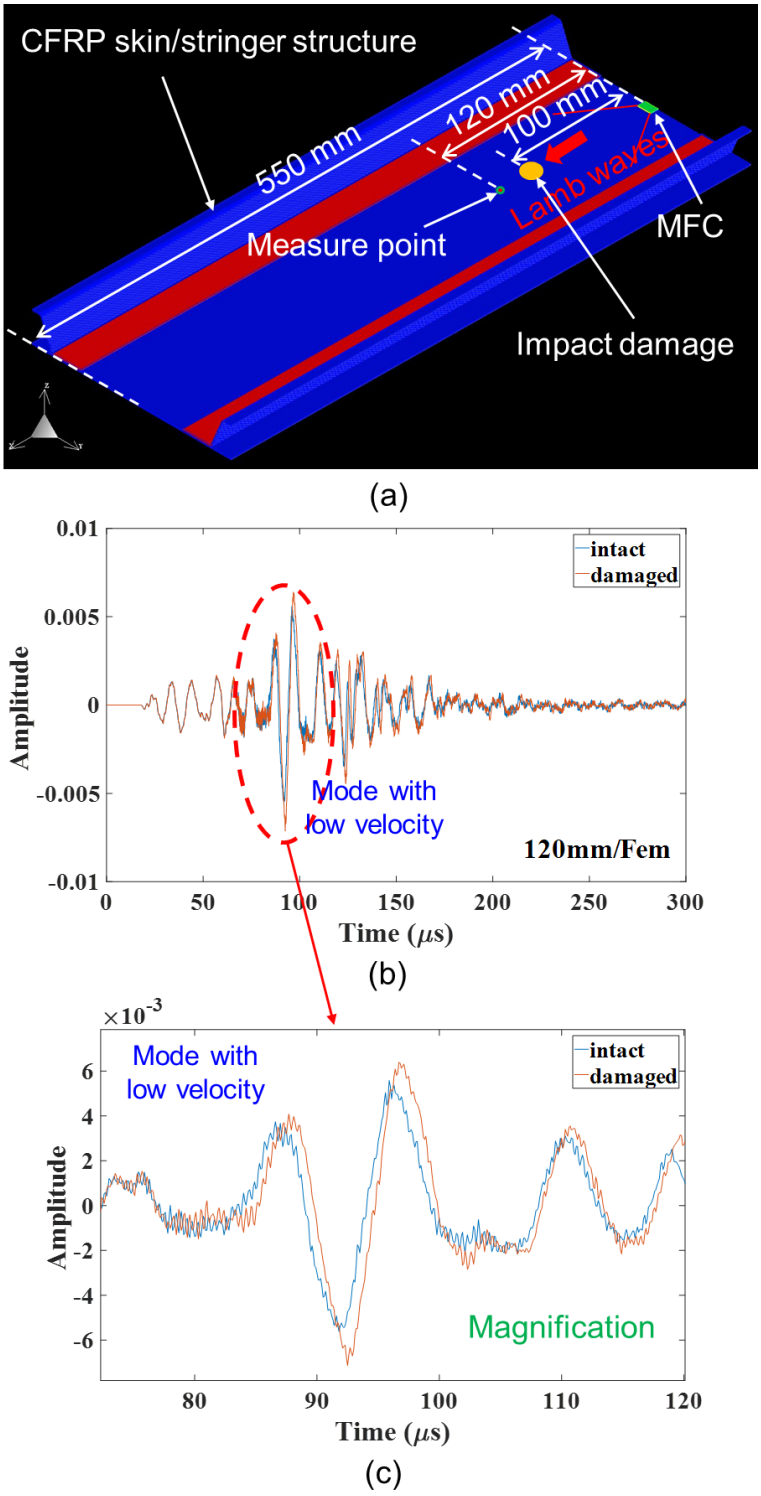

Fig. 3.22. (a) Simulation setup, (b) waveforms of propagated waves between damaged and intact cases and (c) close-up view of waveforms around 90 μs.

These results indicate that the mismatch between the simulation results and experiment results in **Fig. 3.17** is not due to the inaccurate simulation at a longer propagation distance. It may be caused by the inaccuracy in the modeling shape of the impact-damaged region. There is a possibility that the CFRP laminates made of T800/3900-2B may have a different microscopic damage distribution in the impact damage with that of the CFRP laminates made of T700SC/2500, because the T800/3900-2B has interlaminar toughened layers to prevent the progress of delamination. Therefore, we have to investigate the impact damage in detail in T800/3900-2B in our future research.

In this chapter, we have found two domain modes with different velocities: the mode with high velocity and the mode with low velocity and the delay of the mode with low velocity is larger than that of the mode with high velocity. In order to make the detection of impact damage easier, we need to excite this mode more strongly by optimizing the configuration of SHM system. Therefore, it is of great significance to clarify the modes responding to the impact damage. Thus, we attempted to calculate the theoretical dispersion curves in the following chapter.

4 Theoretical investigation of guided wave propagation in CFRP structures

4.1 Introduction

Dispersion relation is a physical concept which describes the dispersion phenomenon in a medium on the properties of a wave travelling within that medium. It relates the velocity of a mode to the frequency. In Lamb waves, the propagation velocities of different modes of Lamb waves can be calculated as a function of frequency, which is called dispersion curves. Due to the existence of dispersion, modes of Lamb waves have two kinds of velocities: phase velocity and group velocity.

In SHM, calculating the dispersion curves of group velocity is a good way to help understanding the velocity of each mode at a certain frequency. For example, **Fig. 4.1** shows that the modes of waveforms at 180 kHz are identified using the dispersion curves of the group velocities of Lamb waves propagating in a flat CFRP plate with infinite width. These waveforms are acquired from the experiment in **Fig. 2.6** (intact and damaged) and the propagation distance is 70 mm. From this Figure, we can know that compared to the mode with high velocity, the mode with low velocity, which is the A_0 mode, has a larger difference in propagation time. This means the A_0 mode is more sensitive to the impact damage in the CFRP laminate plate case.

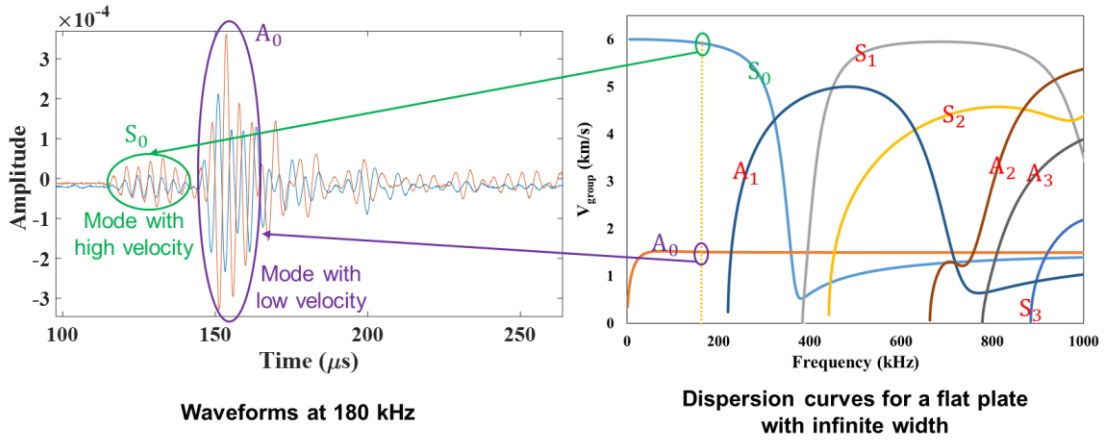

Fig. 4.1. Waveforms at 180 kHz are identified using dispersion curves.

Therefore, for a deeper understanding of the ultrasonic propagation behavior in the results in **Fig. 3.16** and **Fig. 3.17**, we should also clarify the modes in the waves by calculating the theoretical dispersion curves of a CFRP skin/hat-shaped stringer structure.

Fig. 4.2 shows the difference of the calculation of dispersion curves between structures with different boundary conditions.

In **Fig.4.2**, the left structure is a laminates with infinite width, the middle structure is also a laminates but with finite width, the right structure is a skin/stringer structure with periodic boundary. Lamb waves propagate in the Z-axis direction in all three cases.

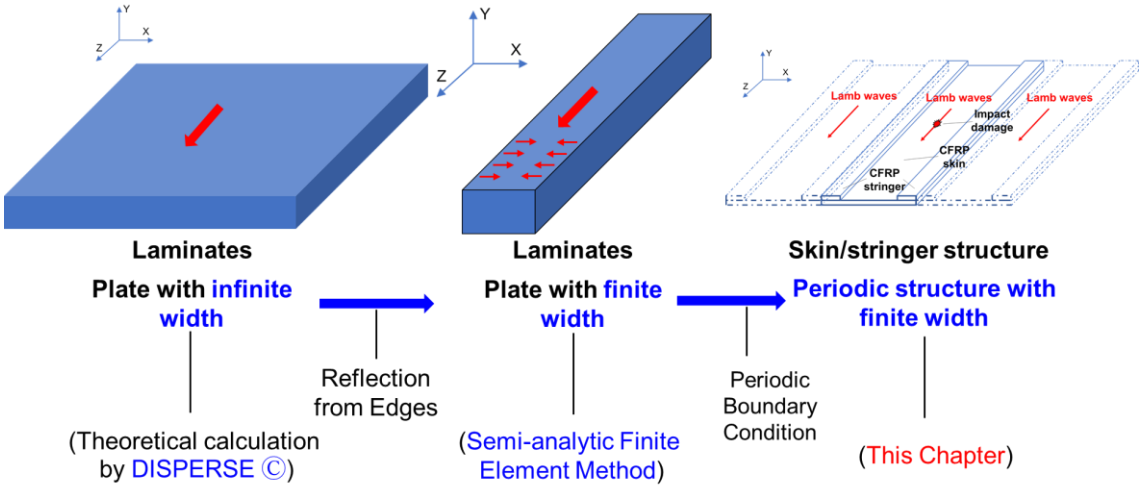

Fig. 4.2. Calculation of dispersion curves for different structures.

In **Section 2.2.1**, the theoretical calculation of velocity dispersion in a flat plate with an infinite width has been discussed. The calculation using software DISPERSE is easy because the wave behavior can be expressed in the two-dimensional cross-section [15].

In the case of a plate with finite width, reflection from side edges cannot be neglected. Hence, the mode behavior becomes much complex due to the transverse oscillations. Since this calculation is three-dimensional, it cannot be completed by using DISPERSE. Therefore, to calculate the dispersion curves in a plate with finite width, a method combining theoretical calculation and finite element analysis was developed by Roses' research group. This method is known as the semi-analytical finite element (SAFE) method [40]. Furthermore, the SAFE method cannot only calculate the dispersion curves of plates with finite width, but also deal with arbitrary cross-sectional shapes.

However, when the SAFE method is applied to the whole of a CFRP skin/stringer structure, the calculation cost becomes very large. Therefore, in this chapter, we took the periodicity of the structure into consideration and introduced periodic boundary conditions into the SAFE method in order to calculate only one unit of such a periodic stiffened structure. We then attempted to calculate the dispersion curves of the CFRP skin/hat-shaped stringer structure mentioned in **Chapter 3**.

4.2 Modified SAFE method

4.2.1 SAFE method

The fundamental equation followed by elastic waves is derived from the principle of virtual work. When an external force does not work, the principle of virtual work is as follows:

$$\int_V \delta u^{\dagger}(\rho \ddot{u}) dV + \int_V \delta \varepsilon^{\dagger} \sigma dV = 0 \,. \tag{18}$$

Here, u is displacement, ρ is density, ε is strain, and σ is stress. † means complex conjugate and taking transpose, and dot means time differentiation. Integration is about volume.

As shown in **Fig. 4.3** (a), the length in the Z-axis direction is infinite and the shape of the XY cross-section is assumed to be uniform along the Z-axis. An elastic wave propagated in the longitudinal direction (Z-axis direction) is considered.

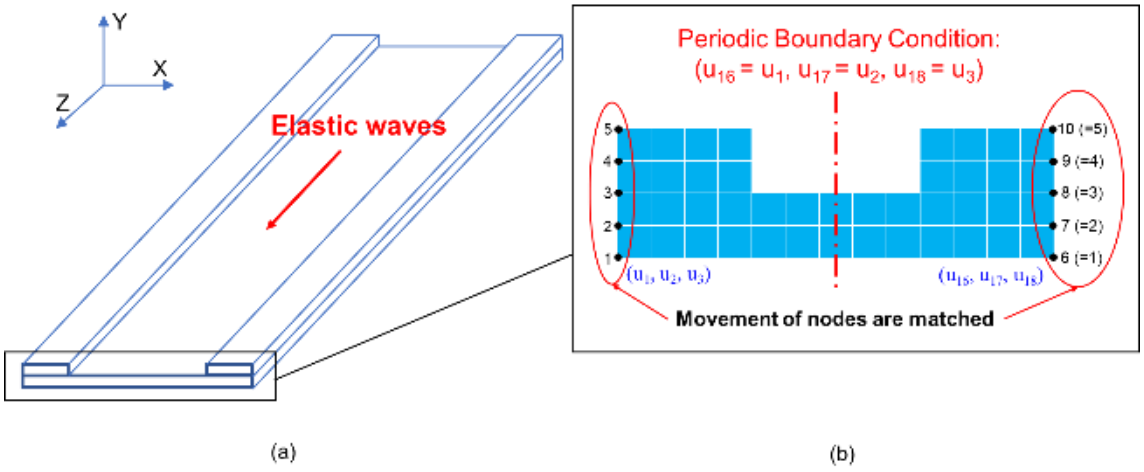

Fig. 4.3. (a) Columnar object through which elastic waves propagate and (b) introduction of periodic boundary condition.

When the elastic wave propagates in the Z-axis direction with the angular frequency ω and wave number ξ, the displacement in **Eq. (18)** can be expressed as:

$$\boldsymbol{u}(x,y,z) = \boldsymbol{f}(x,y)e^{i(\xi z-\omega t)}\,. \tag{19}$$

In the Z direction, $e^{i(\xi z-\omega t)}$ represents a wave with a certain frequency and is handled analytically. On the other hand, in the XY cross-section, a finite element method to divide the cross-section into meshes is used to obtain the displacement $\boldsymbol{f}(x,y)$. Let $\boldsymbol{U}$ be the vector representing the displacement on all nodes. In the presence of displacement in all three (XYZ) directions, $\boldsymbol{U}$ is a $3 \times N_{\mathrm{node}}$ vector. Here, N_{node} is the number of nodes. If only the j-th cell is considered, $\boldsymbol{U}^j$ has only 12 components as shown in **Fig. 4.4**. The displacement of an arbitrary point in j-th cell can be interpolated by the displacement of nodes as follows:

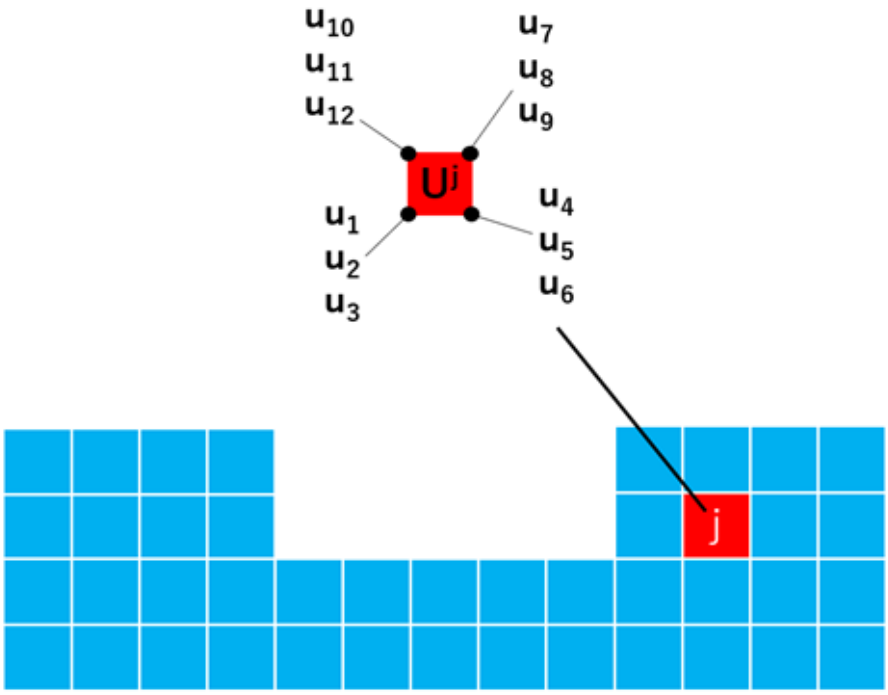

Fig. 4.4. Displacement of vertices of the j-th cell.

$$\boldsymbol{u}(x,y,z) = \boldsymbol{N}(x,y)\boldsymbol{U^j}e^{i(\xi z-\omega t)}\,, \tag{20}$$

where $\boldsymbol{N}(x,y)$ is a shape function which is a 3 × 12 matrix.

The displacement-strain relation and the stress-strain relation are then substituted into **Eq. (18)**, and the relational expression in the j-th cell becomes

$$\delta\boldsymbol{U}^{j\dagger}\left[-\omega^2\boldsymbol{M}^j + \boldsymbol{K}_1^j + i\xi\boldsymbol{K}_2^j + \xi^2\boldsymbol{K}_3^j\right]\boldsymbol{U}^j = \boldsymbol{0}. \tag{21}$$

Here, $\boldsymbol{M}^j$, $\boldsymbol{K}_1^j$, $\boldsymbol{K}_2^j$ and $\boldsymbol{K}_3^j$ are all 12 × 12 matrices represented by the shape function $\boldsymbol{N}(x,y)$ and the stiffness matrix. They are independent of $\boldsymbol{U}^j$ and can be represented by the shape function and the stiffness matrix, respectively.

Furthermore, when the sum is taken for all cells, **Eq. (21)** becomes

$$\delta \boldsymbol{U}^{\dagger}[-\omega^2 \boldsymbol{M} + \boldsymbol{K_1} + i\xi \boldsymbol{K_2} + \xi^2 \boldsymbol{K_3}]\boldsymbol{U} = \boldsymbol{0}. \tag{22}$$

Here, $\boldsymbol{M}$, $\boldsymbol{K}_1$, $\boldsymbol{K}_2$ and $\boldsymbol{K}_3$ are all $3N_{\mathrm{node}} \times 3N_{\mathrm{node}}$ matrices.

The condition that **Eq. (22)** holds for arbitrary $\delta \boldsymbol{U}^{\dagger}$ is

$$[-\omega^2 \boldsymbol{M} + \boldsymbol{K_1} + i\xi \boldsymbol{K_2} + \xi^2 \boldsymbol{K_3}]\boldsymbol{U} = \boldsymbol{0}. \tag{23}$$

Eq. (23) is the fundamental equation that defines $\boldsymbol{U}$. The nontrivial displacement vector $\boldsymbol{U}$ exists on the condition that the determinant of **Eq. (23)** is zero. Therefore,

$$\mathbf{det}\left[-\omega^2 \boldsymbol{M} + \boldsymbol{K_1} + i\xi \boldsymbol{K_2} + \xi^2 \boldsymbol{K_3}\right] = 0. \tag{24}$$

This is associating the angular frequency ω with the wave number ξ, which is the velocity dispersion curve.

Here, the group velocity representing the velocity of a wave packet including waves with various wave numbers can be expressed as

$$\boldsymbol{v_g} = \frac{\boldsymbol{d\omega(\xi)}}{\boldsymbol{d\xi}}. \tag{25}$$

4.2.2 Introduction of periodic boundary condition

The periodic boundary condition is then applied. Since the periodic structure is a continuous structure in which the same unit structural elements are connected to each other, the dimensions and shapes of the unit structural elements are completely identical. However, it is necessary to

match the movement of the left and right shared nodes when connecting them together as shown in **Fig. 4.3 (b)**. Furthermore, because the movements of the left and right shared nodes are matched, the degree of freedom of the entire structure will have a reduction. Thus, $\boldsymbol{M}$, $\boldsymbol{K}_1$, $\boldsymbol{K}_2$ and $\boldsymbol{K}_3$ are no longer $3N_{\mathrm{node}} \times 3N_{\mathrm{node}}$ matrices, and the dimension of the matrices will drop.

We have also made some other modifications to SAFE method. In the calculation, we separate all the modes according to symmetry and calculate them separately. This calculation strategy can greatly reduce the calculation cost.

By introducing this boundary condition into the SAFE method, we modify it to be appropriate to calculate the dispersion curves of a skin/stringer periodic structure. Thus, in this thesis, we called it “the modified SAFE method”.

4.3 Calculation of dispersion curves in a periodic stiffened panel structure

As the preparation for calculating dispersion curves of the skin/hat-shaped stringer structure, we first attempted to calculate the dispersion curves of a CFRP periodic stiffened panel structure using the modified SAFE method.

In this stiffened panel structure, the material properties of T700SC/2500 (see **Table 2.1**) are used for CFRP, the laminated configuration is considered quasi-isotropic, the thickness of the

panel and the stiffener are both 1.5 mm, and the distance between adjacent stiffeners was 107 mm. The mesh division of the cross-section is shown in **Fig. 4.5**.

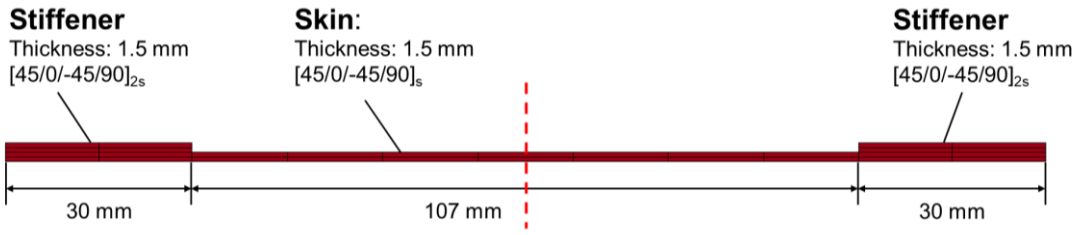

Fig. 4.5. Cross-section of one unit of a periodic stiffened panel structure is divided into meshes.

After mesh division, the periodic boundary condition was introduced on the left and right shared nodes. The appropriate range and increment of the angular frequency ω and wave number ξ were set, the solution of **Eq. (24)** was sought, and then the dispersion curves were calculated.

As a result, the dispersion relation of (ω, ξ) in asymmetric mode and symmetric mode are obtained as shown in **Fig. 4.7**. As the symmetric plane is in the YZ plane instead of the XZ plane, the definition of symmetry in a periodic stiffened panel structure is different from that in a flat plate with infinite width. We defined the lower-order modes as shown in **Fig. 4.6** in this thesis.

According to the deformation state of the lower-order modes, we define the mode sequence by counting the number of knots on one side of the symmetric plane. For each antisymmetric mode, they are designated $A_0, A_1, A_2, \cdots$, and for each symmetric modes, they are designated $S_0, S_1, S_2, \cdots$.

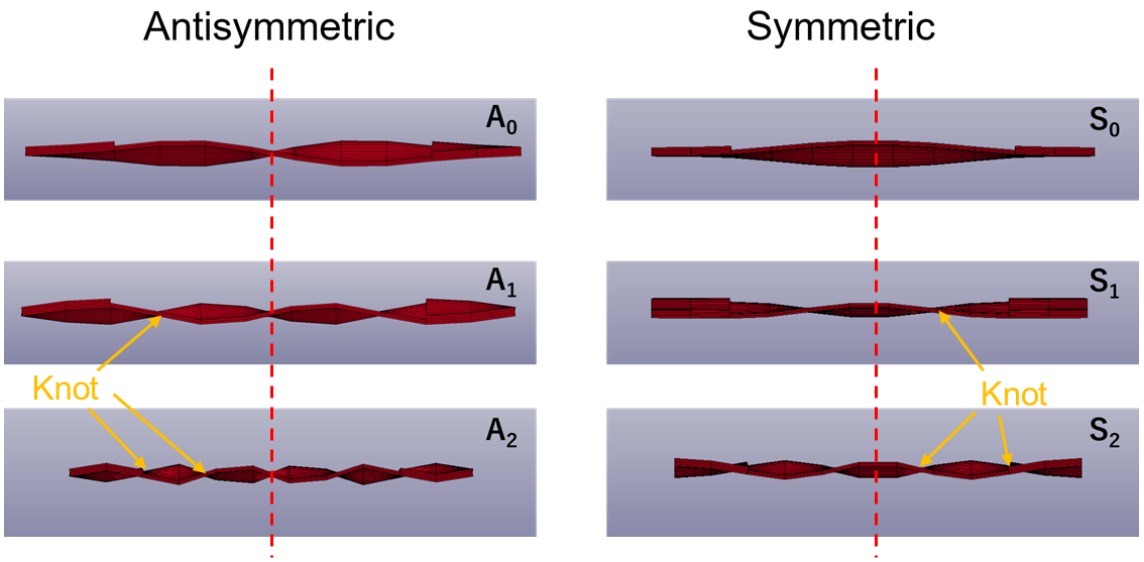

Fig. 4.6. The deformation state of lower-order modes viewed from the cross-section in a periodic stiffened panel structure.

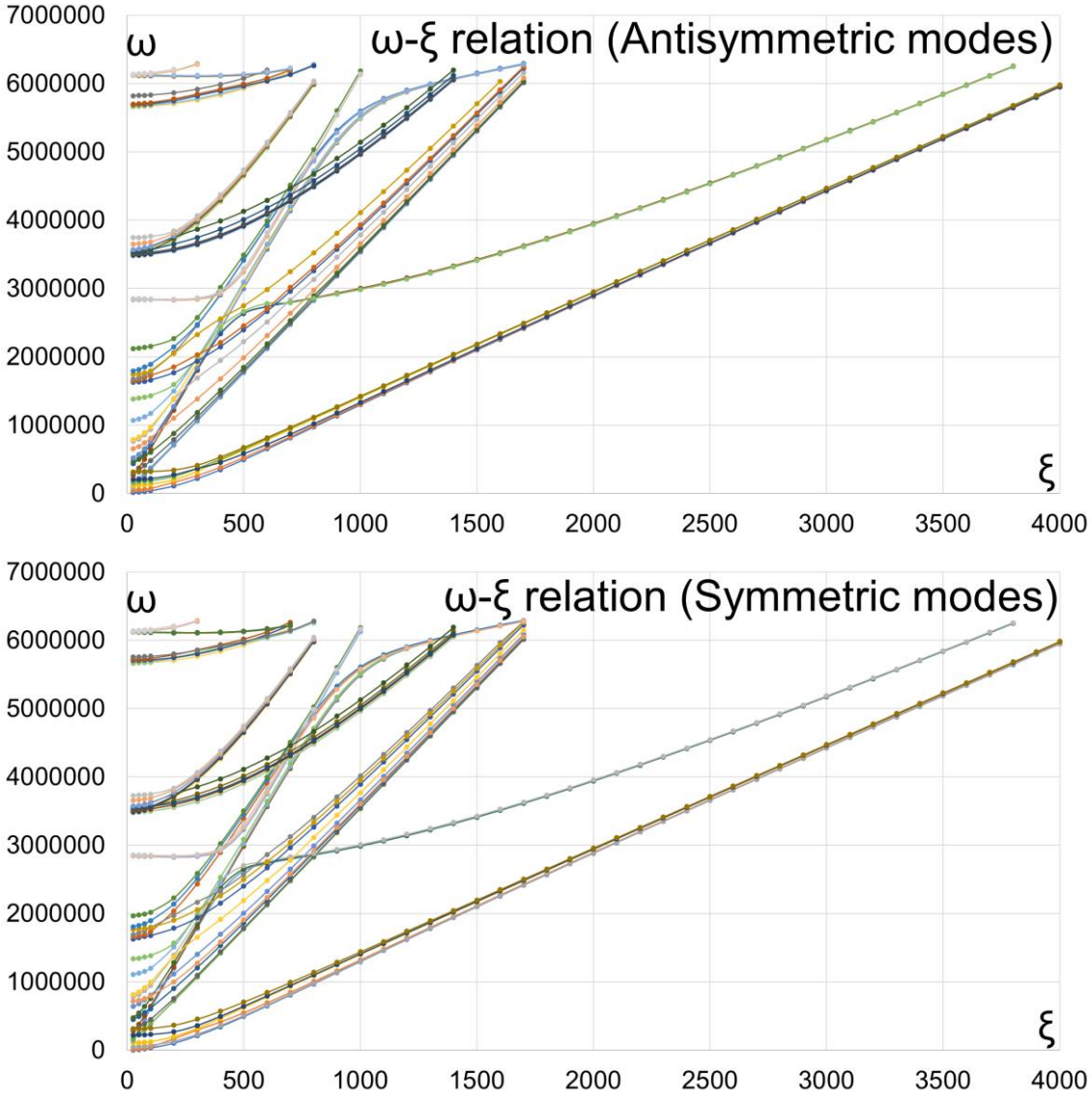

Fig. 4.7. Dispersion relation of (ω, ξ) in a periodic stiffened panel structure.

Furthermore, the group velocities are calculated from the dispersion relation of (ω, ξ) by using **Eq. (25)** and the results are shown in **Fig. 4.8**. The frequency range is from 0 to 1000 kHz.

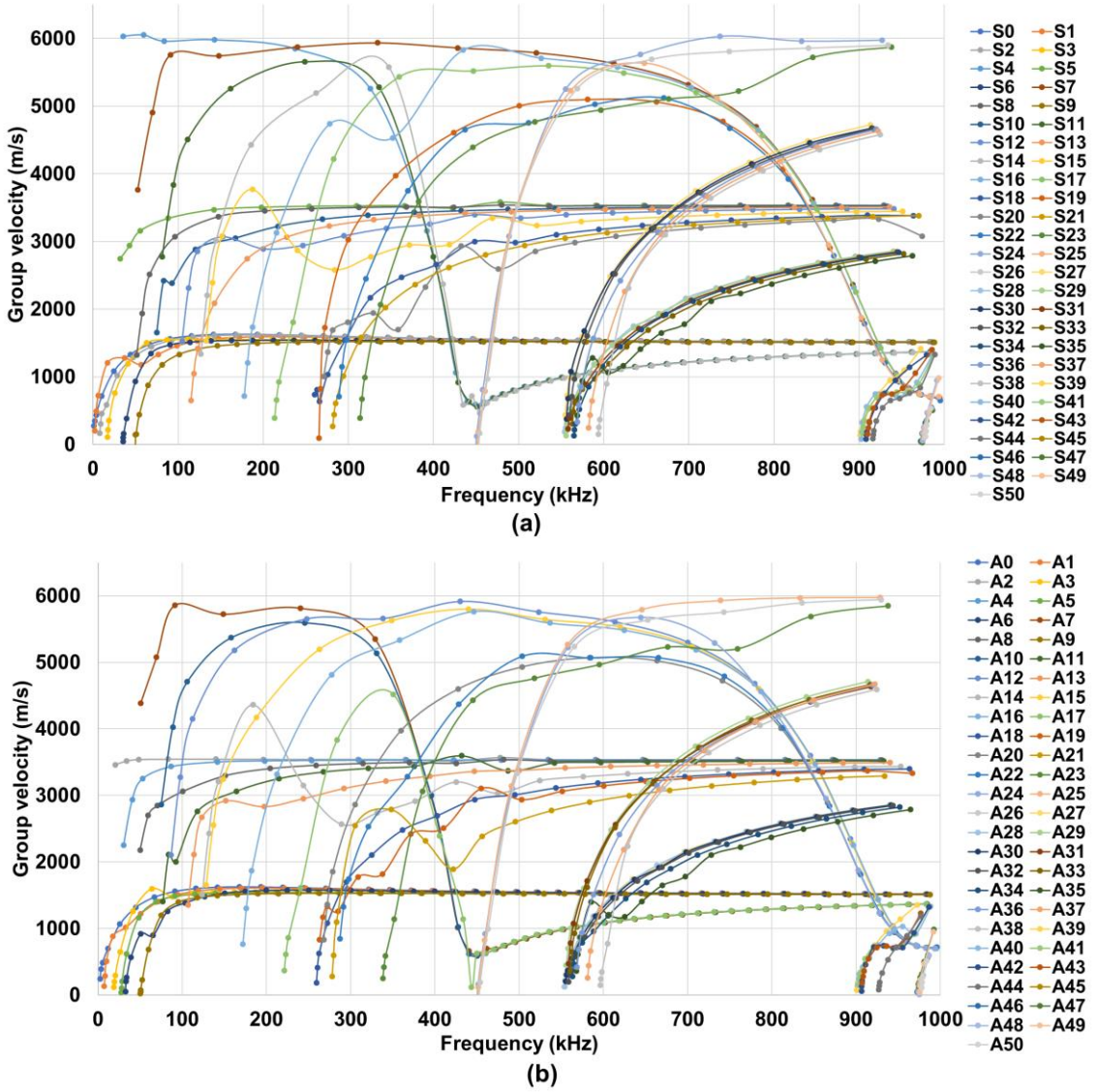

Fig. 4.8. Calculated group velocity dispersion curves in a periodic stiffened panel structure. Quasi-isotropic lamination of T700SC/2500. Skin thickness: 1.5 mm. Thickness of stiffener part: 1.5 mm. The distance between adjacent stringers: 107 mm. (a) Symmetric modes, (b) Antisymmetric modes.

4.4 Discussion on the introduction of periodic boundary condition

In order to confirm the effect of introducing the periodic boundary condition on the dispersion curves of the periodic structure, a comparison was made between the periodic stiffened panel structure and the single structure of only one unit with left and right boundary conditions as the free ends. The dispersion curves of two cases are shown in **Fig. 4.9**.

From **Fig. 4.9**, the total distribution of modes is similar between two cases because the same stiffness parameters and the thickness of the structure are used. However, several differences were still found around 100 kHz, 450 kHz and 750 kHz between the two cases.

Therefore, in order to accurately obtain the velocity dispersion curves in a periodic structure such as the stiffened panel structure or skin/hat-shaped stringer structure, it is necessary to introduce the periodic boundary condition into the SAFE calculation.

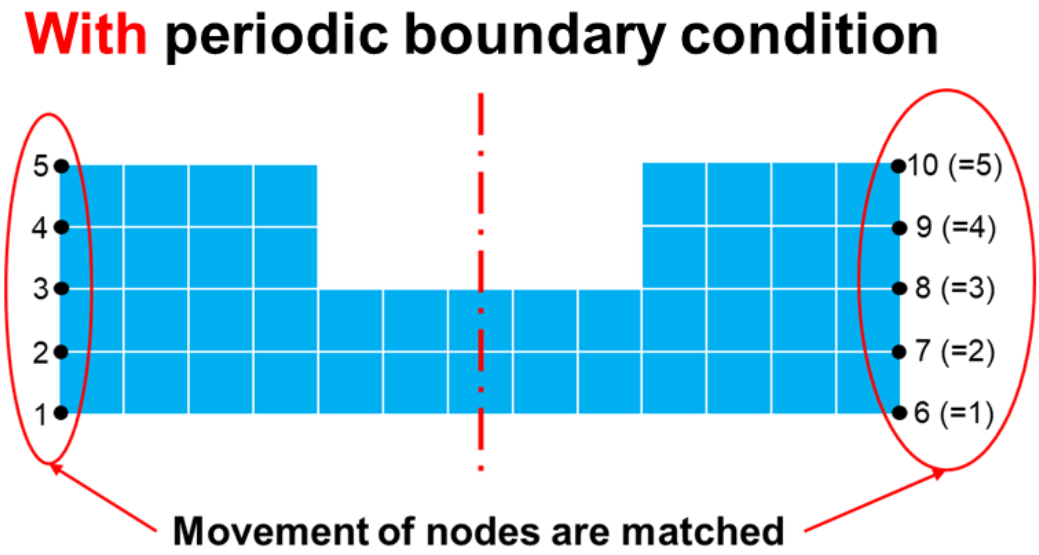
With periodic boundary condition
5
4
3
2
1
10 (=5)
9 (=4)
8 (=3)
7 (=2)
6 (=1)
Movement of nodes are matched

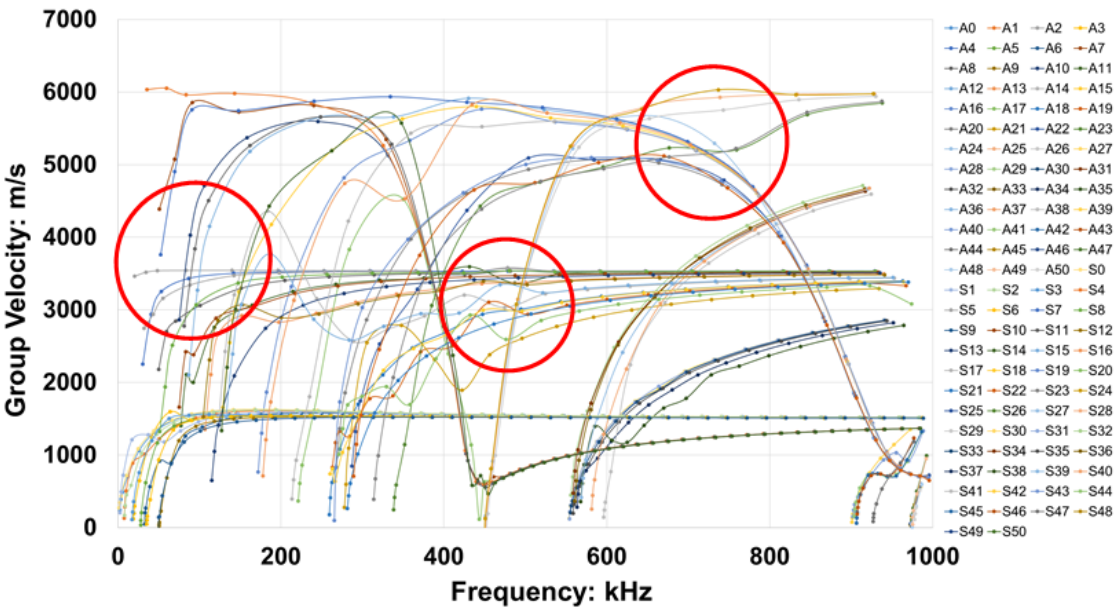
Group Velocity: m/s
7000
6000
5000
4000
3000
2000
1000
0
0
200
400
600
800
1000
Frequency: kHz
A0 A1 A2 A3
A4 A5 A6 A7
A8 A9 A10 A11
A12 A13 A14 A15
A16 A17 A18 A19
A20 A21 A22 A23
A24 A25 A26 A27
A28 A29 A30 A31
A32 A33 A34 A35
A36 A37 A38 A39
A40 A41 A42 A43
A44 A45 A46 A47
A48 A49 A50 S0
S1 S2 S3 S4
S5 S6 S7 S8
S9 S10 S11 S12
S13 S14 S15 S16
S17 S18 S19 S20
S21 S22 S23 S24
S25 S26 S27 S28
S29 S30 S31 S32
S33 S34 S35 S36
S37 S38 S39 S40
S41 S42 S43 S44
S45 S46 S47 S48
S49 S50

(a)

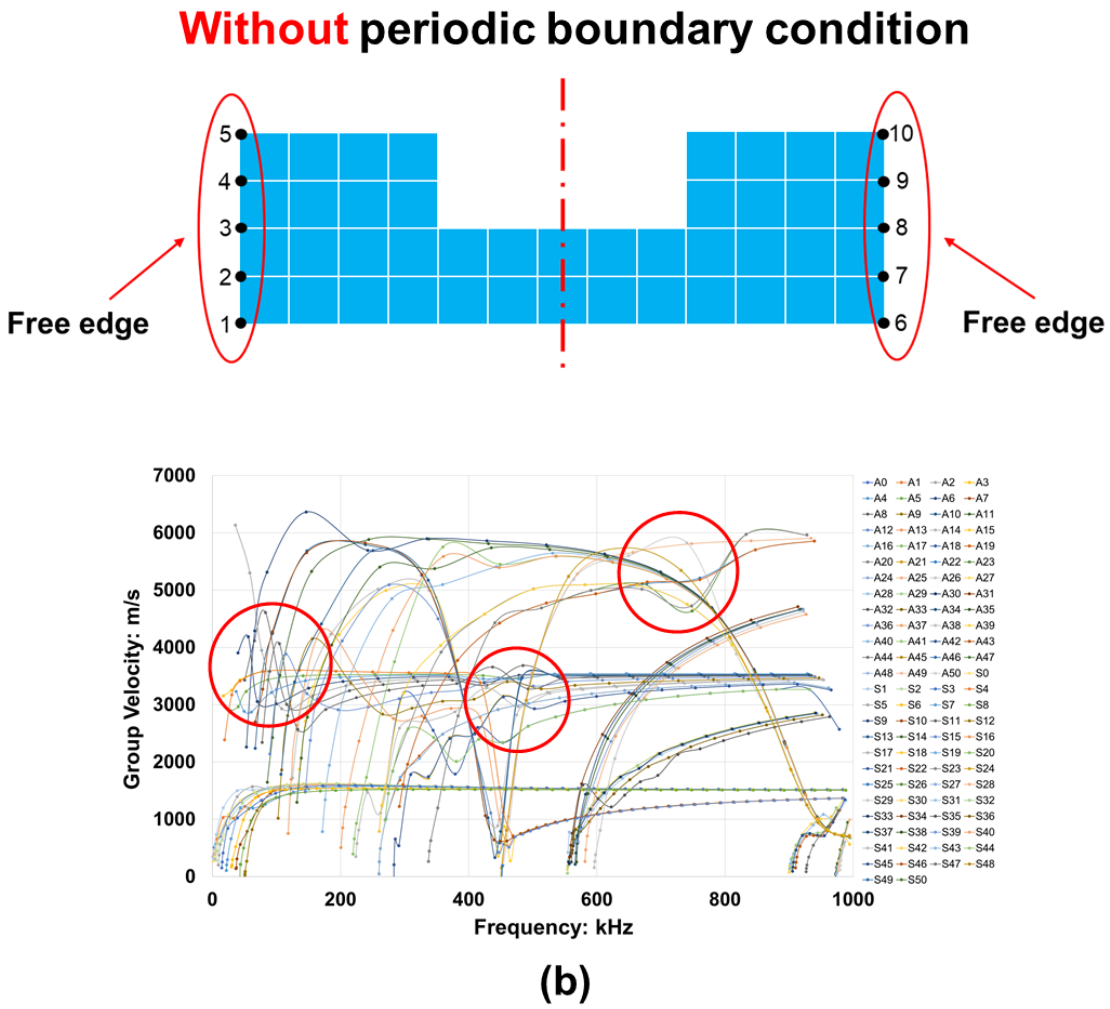

Fig. 4.9. Comparison of calculated dispersion curves between two cases: (a) with periodic boundary and (b) without periodic boundary condition.

4.5 Calculation of dispersion curves in a skin/hat-shaped stringer structure

The same method was then applied to the skin/hat-shaped stringer structure. The dimensions and material parameters of the skin/hat-shaped stringer structure are the same as those used in

Chapter 3. That is, different from the stiffened panel, the material properties of T800/3900-2B (see **Table 3.1**) were used. The mesh division of the cross-section is shown in **Fig. 4.10**.

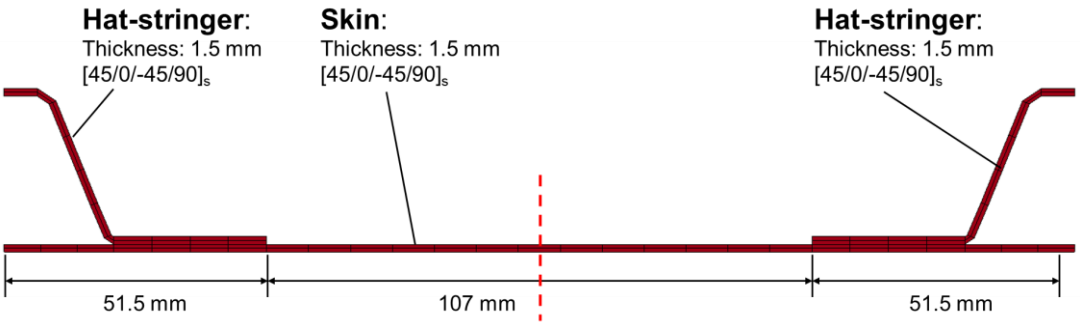

Fig. 4.10. Cross-section of one unit of the skin/hat-shaped stringer structure is divided into meshes.

We then calculated the dispersion curves using the same method, and the results of dispersion curves from 0 to 300 kHz are shown in **Fig. 4.11** (a) (symmetric modes) and **Fig. 4.11** (b) (antisymmetric modes).

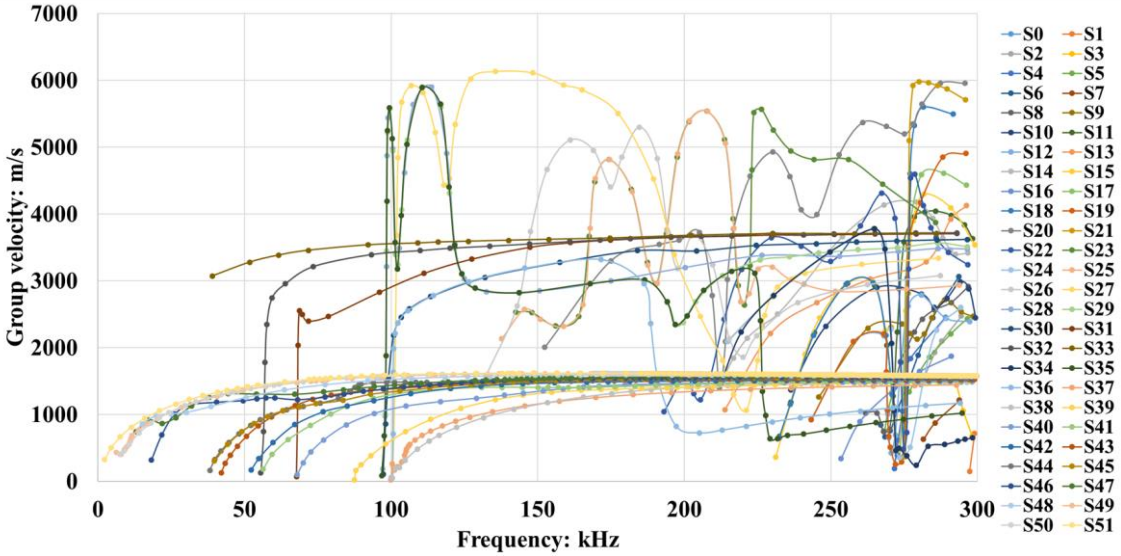

(a)

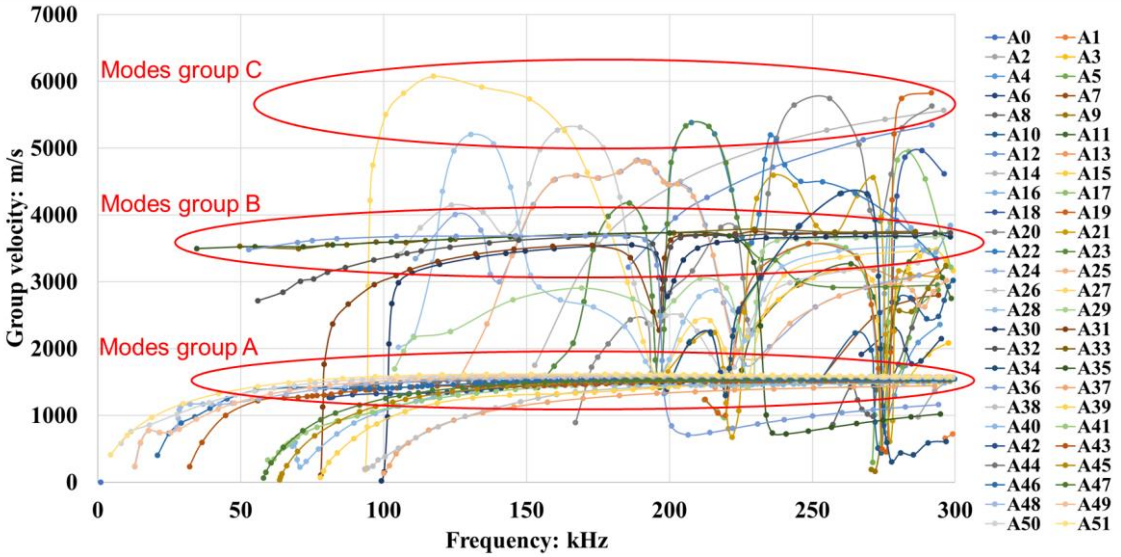

(b)

Fig. 4.11. Calculated group velocity dispersion curves in the CFRP skin/hat-shaped stringer structure. Quasi-isotropic lamination of T800/3900-2B. Skin thickness: 1.5 mm. Stringer thickness: 1.5 mm. The distance between adjacent stringers: 107 mm. (a) Symmetric modes, (b) Antisymmetric modes.

4.6 Verification of dispersion curves in a skin/hat-shaped stringer structure

In order to verify the calculated dispersion curves, we constructed a finite element model with ComWAVE, in which the CFRP skin/hat-shaped stringer structure has the same dimensions of those shown in **Fig. 3.2** but the impact damage and MFC actuator is not modeled. In this model, ultrasonic waves are excited with uniform oscillation of the entire end of the structure instead of using an MFC as an actuator (see **Fig. 4.12**). The verification distance is 200 mm.

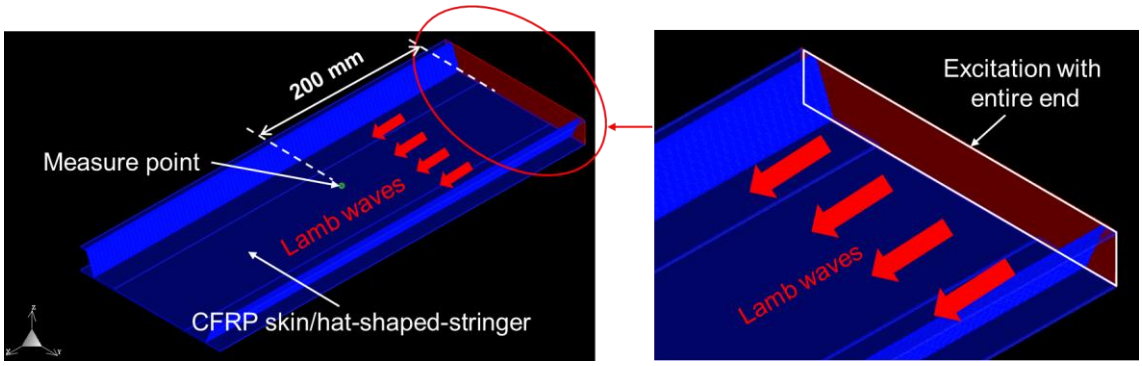

Fig. 4.12. Verification model and forced uniform oscillation of the entire end.

We then generated ultrasonic Lamb waves with the input signal as a three-cycle sinusoidal wave with a Hamming window at 100 kHz, 200 kHz and 300 kHz, respectively. Waveforms received at the measure point underwent wavelet transformation and the results are shown in **Fig. 4.13**.

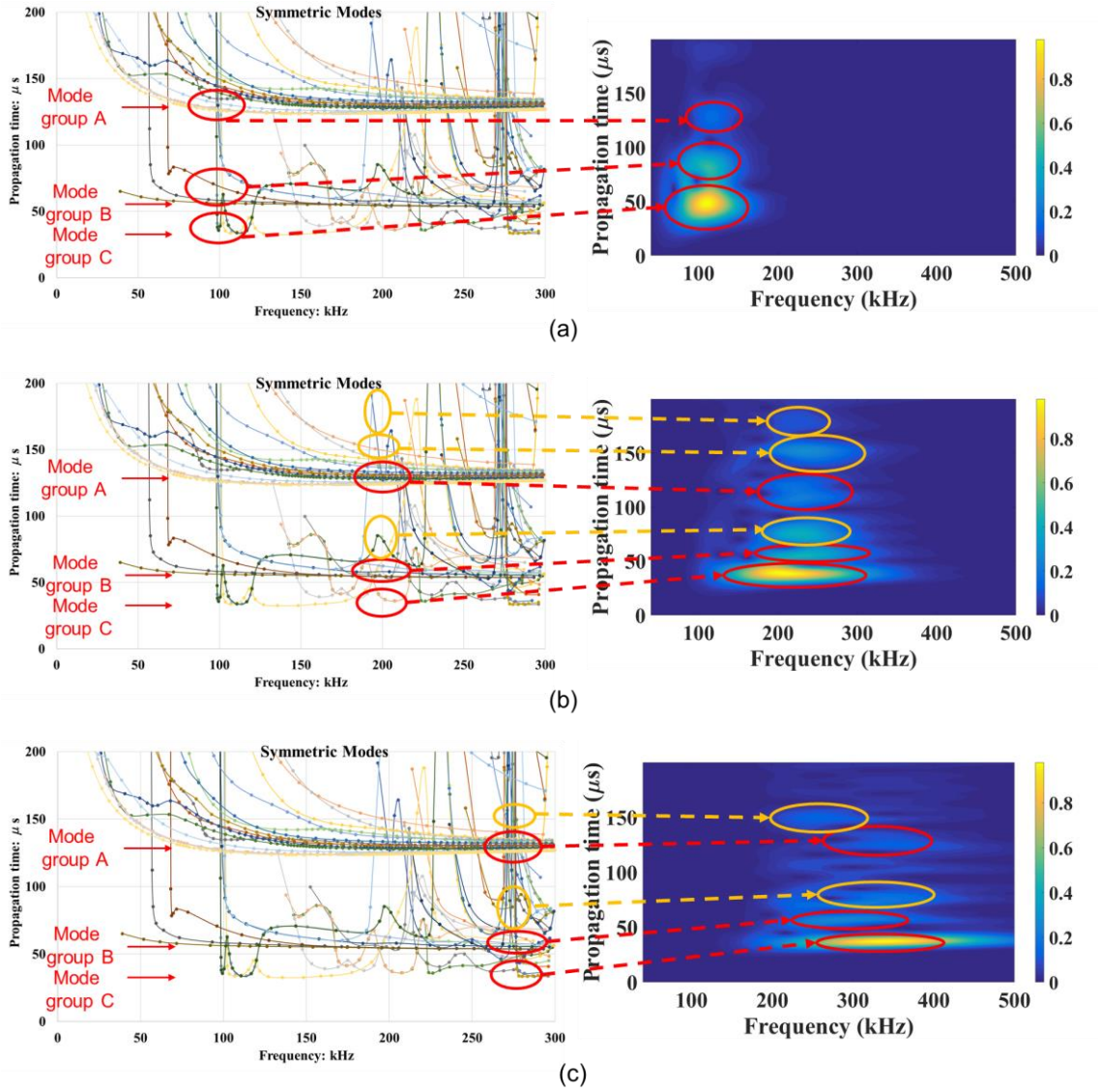

Fig. 4.13. Comparison between dispersion curves and wavelet transform results of simulation waveforms at (a) 100 kHz, (b) 200 kHz, (c) 300 kHz.

Fig. 4.13 (a) shows that the wavelet transform results agree well with the dispersion curves in propagation time of the three primary mode group regions. The propagation time of mode group

C, mode group B, and mode group A is respectively around 40 μs, 70 μs, and 130 μs. However, in the wavelet transform results in **Fig. 4.13** (b) and **Fig. 4.13** (c), more mode group regions can be found as the velocities of modes are more dispersive at 200 kHz and 300 kHz according to the dispersion curves. These comparison results verify that the calculated dispersion curves of the CFRP skin/hat-shaped stringer structure are appropriate.

4.7 Discussion about mode identification

From the dispersion curves in **Fig. 4.11** we found that the number of modes drastically increased compared to that of a flat plate with infinite width shown in **Fig. 2.1**. In **Fig. 4.11**, the group velocities of the modes are found to be concentrated in three regions. The deformation states of the modes in the three groups are then plotted with LS-PrePost 4.2, as shown in **Fig. 4.14**.

Fig. 4.14. Deformation state of typical modes in the three groups.

According to the deformation state type plotted in **Fig. 4.14**, we can infer that the three mode groups are, respectively, group A with the lowest velocity of transverse waves, group B with the middle velocity of shear-horizontal waves and group C with the highest velocity of longitudinal waves.

We then compared the calculated dispersion curves in **Fig. 4.11** with the waveforms in the simulation at 100 kHz in **Fig. 3.17**. Through the calculation of propagation velocity, we found that the wave modes with high velocity and low velocity in the FEM simulation results can be identified as the mode group of longitudinal waves and transversal waves, respectively (see **Fig. 4.15**).

Furthermore, because the most sensitive mode to impact damage is the mode with low velocity as discussed in **Section 3.5**, it can be inferred that the most sensitive mode to the impact damage is the transversal mode of group A.

Theoretical dispersion curves can help us identify the modes but cannot give the information of the specific amplitude of each mode/ mode group. The FEM simulation can provide us with waveforms including amplitude information. Using only one method cannot help us fully understand the propagation behavior of Lamb waves. Thus, the two methods should be combined together.

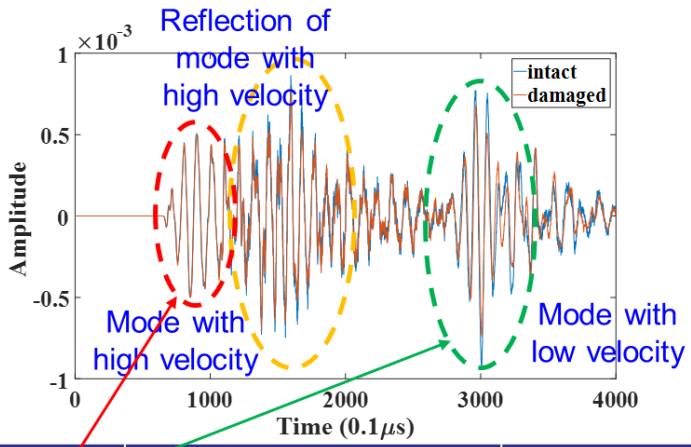

Mode group	Velocity	Wave Classification
A	Low (1.4 km/s)	Transversal wave
B	Medium (3.7 km/s)	Shear-horizontal wave
C	High (5.2 km/s)	Longitudinal wave

Fig. 4.15. Modes in the waveform are identified with dispersion curves.

4.8 Discussion about designing of the SHM system

The above discussion gives us useful information in designing the SHM system.

The configuration of the SHM system should be designed to excite the transversal mode group A strongly to detect impact damages more reliably. Also, we can judge whether damage has occurred or not through the presence of a delay in the transversal mode group A in the received waveform.

Therefore, we can judge whether impact damage with the same dimensions but occurring at different locations in the structure is detectable or not by using this judgement method. We then can outline the detectable range of impact damage of the present system.

To verify this, we established four models, the same as in **Fig. 3.2** but with different damage locations, by using ComWAVE. The impact damage locations are respectively named I, II, III, and IV and the distance between them and the schematic of them is shown in **Fig. 4.16**. The centers of these impact damage areas are in a line perpendicular to the X-axis and the distance between them is 7 mm, which is half the width of the MFC.

The waveforms of the same measure point, which is 430 mm from the MFC actuator, are then compared between the intact case, case I, case II, case III, and case IV. **Fig. 4.17** and **Fig. 4.18** show a close-up view of the waveform results around 300 μs.

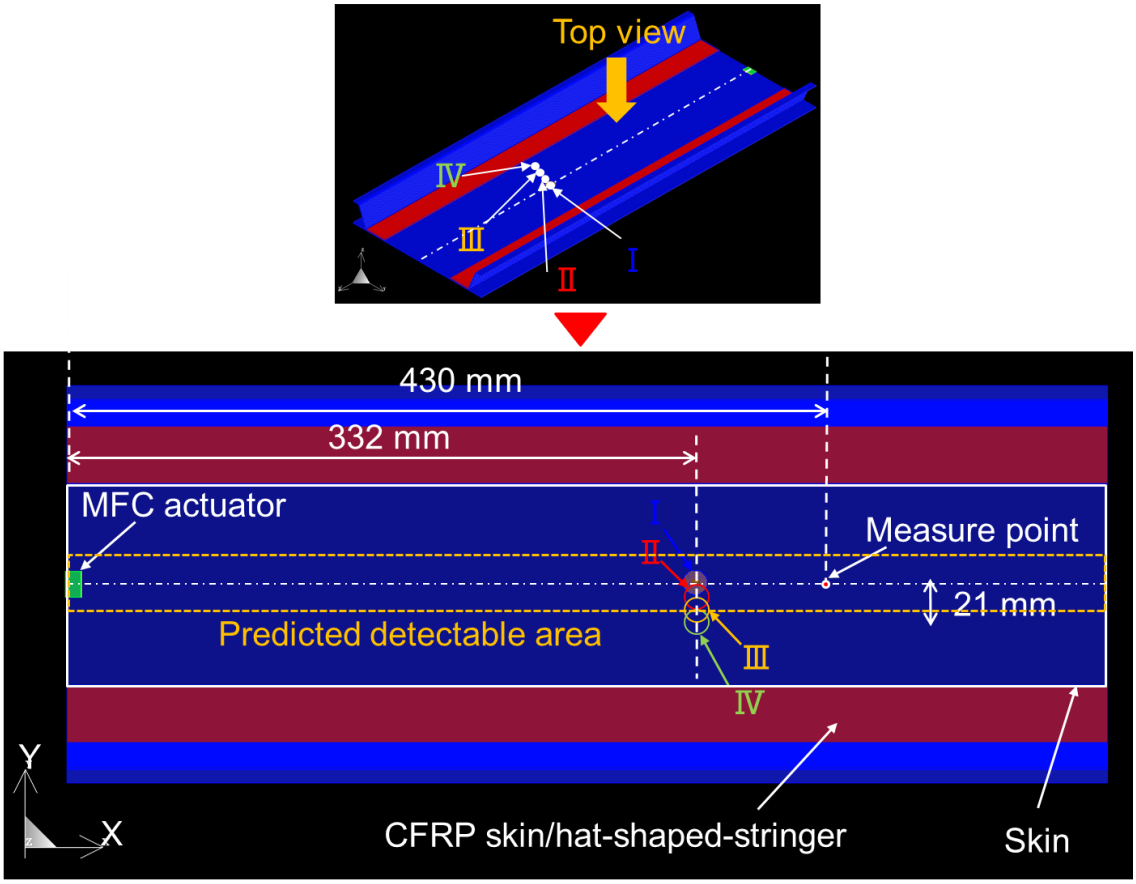

Fig. 4.16. Schematic of different impact damage locations I, II, III, and IV.

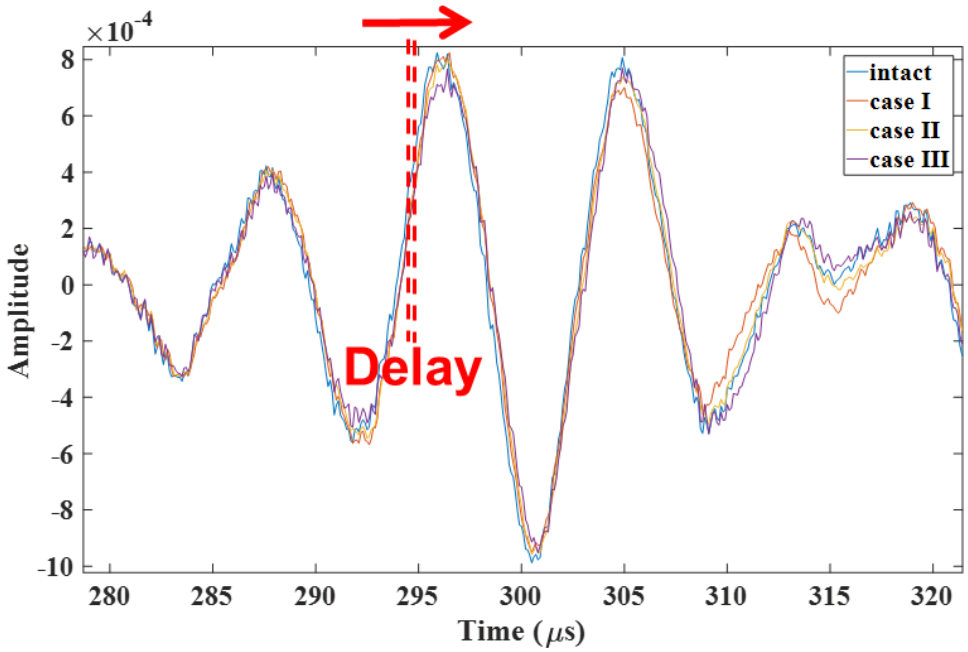

Fig. 4.17. Waveform comparison between the intact case, case I, case II, and case III.

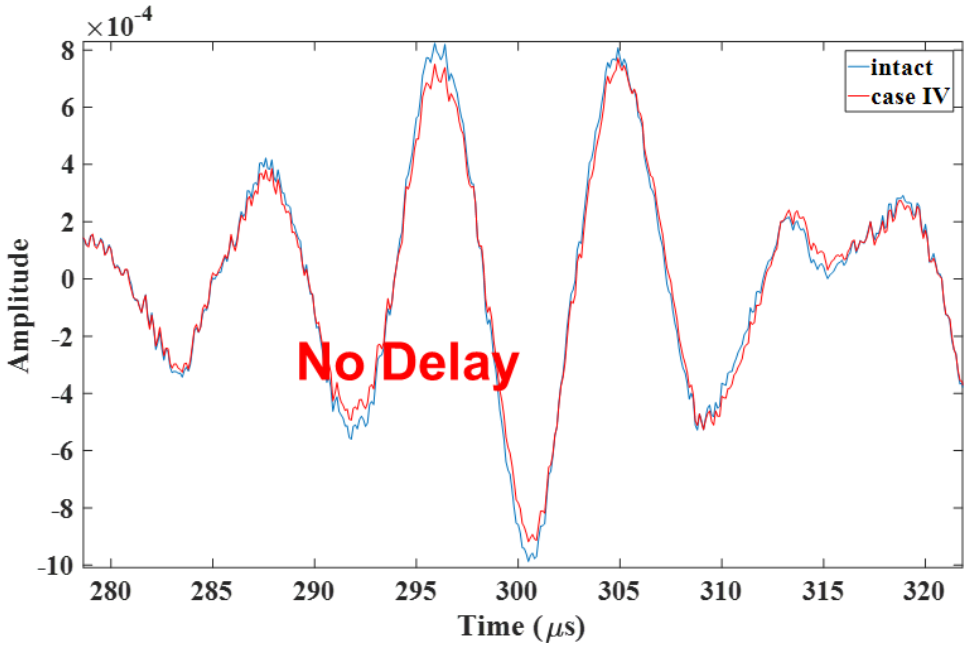

Fig. 4.18. Waveform comparison between the intact case and case IV.

Fig. 4.17 shows that a delay which is about 0.2 μs exists in each comparison of the waveform pairs of the intact case/case I, the intact case/case II, and the intact case/case III. This means that when impact damage occurs in these locations, it can be detected. On the other hand, **Fig. 4.18** shows that the delay is 0 μs in the comparison of the waveform pair of the intact case/case IV. This means that when impact damage occurs in location IV, it cannot be detected.

According to these results, we can conclude that only the impact damage which occurs in the area close to the line connecting actuator and sensor can be detected by using this configuration of MFC actuator and FBG sensor, as the predicted detectable area shown in **Fig. 4.16**. When impact damage occurs outside of this area, it cannot be detected by using this configuration.

Therefore, for the designing of an SHM system with a wider target area, setting several pairs of MFC actuator and FBG sensor may increase the reliability of the SHM system.

5 Conclusions

In this thesis, first the background information and relevant conceptions, as well as the objective and framework, were introduced in **Chapter 1**.

In **Chapter 2**, a simplified simulation method of impact damage was constructed and the appropriateness of it was verified through the comparison with the precise multiple delamination model and the experimental observation.

In **Chapter 3**, the proposed FEM simulation method was applied to a CFRP skin/hat-shape stringer structure and the results of the simulation agreed well with those of the experiment.

In **Chapter 4**, the propagation behaviors of the guided wave were investigated theoretically by using the modified SAFE method to calculate the dispersion curves of the CFRP skin/stringer structures to deeply understand the received waveforms. Discussion was made about the designing of the SHM system detecting impact damage.

In **Appendix Chapter A**, the applicability of this FEM simulation method in a fabric CFRP laminates was investigated.

This method is a simplified modeling method with degradation ratio without depending on the details of the microscopic damages in the impact-damaged area. However, the damage distribution may change as material changes. Thus, when this method is applied to other CFRP

quasi-isotropic materials such as fabric CFRP, the hypothesis of damage shape may need some adjustments to make this method more reliable.

References

[1] http://scribol.com/technology/aviation/airbus-a350-composites-on-trial-part-i/

[2] Marsh, George. "Airbus A350 XWB update." Reinforced Plastics 54.6 (2010): 20-24.

[3] Marsh, George. "Airbus takes on Boeing with reinforced plastic A350 XWB." Reinforced Plastics 51.11 (2007): 26-29.

[4] Roberts, Tony. "Rapid growth forecast for carbon fibre market." Reinforced Plastics 51.2 (2007): 10-13.

[5] Holmes, Mark. "Carbon fibre reinforced plastics market continues growth path." Reinforced Plastics 57.6 (2013): 24-29.

[6] Holmes, Mark. "Global carbon fibre market remains on upward trend." Reinforced Plastics 58.6 (2014): 38-45.

[7] Polimeno, U., and M. Meo. "Detecting barely visible impact damage detection on aircraft composites structures." Composite Structures 91.4 (2009): 398-402.

[8] Abrate, Serge. "Impact on laminated composite materials." Applied Mechanics Reviews 44.4 (1991): 155-190.

[9] Cantwell, W. J., and J. Morton. "Detection of impact damage in CFRP laminates." Composite Structures 3.3-4 (1985): 241-257.

[10] Mix, Paul E. Introduction to Nondestructive Testing: a Training Guide. John Wiley & Sons,

2005.

[11] Giurgiutiu, Victor. Structural Health Monitoring with Piezoelectric Wafer Active Sensors: with Piezoelectric Wafer Active Sensors. Elsevier, 2007.

[12] Bond, R., D. Adams, and D. Roach. "Structural Health Monitoring for Impact Damage in Composite Structures." SANDIA report (2014).

[13] Cramer, K. Elliott. "Research developments in nondestructive evaluation and structural health monitoring for the sustainment of composite aerospace structures at nasa." (2016).

[14] Balageas, Daniel, Claus-Peter Fritzen, and Alfredo Güemes, eds. Structural Health Monitoring. Vol. 90. John Wiley & Sons, 2010.

[15] Giurgiutiu, Victor. "Tuned Lamb wave excitation and detection with piezoelectric wafer active sensors for structural health monitoring." Journal of Intelligent Material Systems and Structures 16.4 (2005): 291-305.

[16] Raghavan, Ajay. "Guided-wave structural health monitoring." The Shock and Vibration Digest 39.2 (2007): 91-116.

[17] Worlton, D. C. "Experimental confirmation of Lamb waves at megacycle frequencies." Journal of Applied Physics 32.6 (1961): 967-971.

[18] Firestone, Floyd A. "Flaw detecting device and measuring instrument." U.S. Patent No. 2,280,226. 21 Apr. 1942.

[19] Su, Zhongqing, Lin Ye, and Ye Lu. "Guided Lamb waves for identification of damage in composite structures: A review." Journal of Sound and Vibration 295.3-5 (2006): 753-780.

[20] Hideki Soejima, Kohei Takahashi, et al. “Development of ultrasonic wave based structural health monitoring system for practical use.” Proc. 29th ICAF Symposium, Nagoya, Japan, 2017.

[21] Ogisu, T., et al. "Evaluation of FBG/PZT actuator hybrid damage monitoring system using structural element specimen." Proc. 5th International Workshop on Structural Health Monitoring 2005. 2005.

[22] Soejima, H., et al. "Investigation of the Probability of Detection of our SHM System." 6th European Workshop on Structural Health Monitoring, Dresden, Germany. 2012.

[23] K. Takahashi, H. Soejima, A. Sakabe, Y. Okabe, N, Takeda and M. Yoshida, “Damage detection technology for CFRP structure using MFC/FBG hybrid sensor system”, Proc. International Workshop on Structural Health Monitoring 2013.

[24] TAKAHASHI, Kohei, et al. "Development of FBG-MFC hybrid SHM system for aircraft composite structures in collaboration study with Airbus."

[25] Okabe, Yoji, et al. "Evaluation of debonding progress in composite bonded structures using ultrasonic waves received in fiber Bragg grating sensors." Smart Materials and Structures 16.4 (2007): 1370.

[26] Okabe, Yoji, et al. "Delamination detection in composite laminates using dispersion change based on mode conversion of Lamb waves." Smart Materials and Structures 19.11 (2010): 115013.

[27] Soejima, Hideki, et al. "Experimental Investigation of Impact Damage Detection for CFRP Structure by Lamb Wave Sensing Using FBG/PZT Hybrid System." 16th International Conference on Composite Materials. Kyoto, Japan: the Japan Society for Composite Materials (JSCM) and the Japan Aerospace Exploration Agency (JAXA). 2007.

[28] Frecker, Mary I. "Recent advances in optimization of smart structures and actuators." Journal of Intelligent Material Systems and Structures 14.4-5 (2003): 207-216.

[29] Gao, Huidong, and J. L. Rose. "Ultrasonic sensor placement optimization in structural health monitoring using evolutionary strategy." AIP Conference Proceedings. Vol. 820. No. 1. AIP, 2006.

[30] Guo, H. Y., et al. "Optimal placement of sensors for structural health monitoring using improved genetic algorithms." Smart Materials and Structures 13.3 (2004): 528.

[31] Yi, Ting-Hua, Hong-Nan Li, and Ming Gu. "Optimal sensor placement for structural health monitoring based on multiple optimization strategies." The Structural Design of Tall and Special Buildings 20.7 (2011): 881-900.

[32] Shen, Qin, Mohammed Omar, and Shan Dongri. "Ultrasonic NDE techniques for impact

damage inspection on CFRP laminates." Journal of Materials Science Research 1.1 (2011): 2.

[33] Edwards, C., A. Al-Kassim, and S. B. Palmer. "Laser ultrasound for the study of thin sheets." Review of Progress in Quantitative Nondestructive Evaluation. Springer, Boston, MA, 1993. 539-548.

[34] Basri, R., and W. K. Chiu. "Numerical analysis on the interaction of guided Lamb waves with a local elastic stiffness reduction in quasi-isotropic composite plate structures." Composite Structures 66.1-4 (2004): 87-99.

[35] Aymerich, Francesco, F. Dore, and P. Priolo. "Prediction of impact-induced delamination in cross-ply composite laminates using cohesive interface elements." Composites Science and Technology 68.12 (2008): 2383-2390.

[36] Aymerich, Francesco, F. Dore, and P. Priolo. "Simulation of multiple delaminations in impacted cross-ply laminates using a finite element model based on cohesive interface elements." Composites Science and Technology 69.11-12 (2009): 1699-1709.

[37] Bouvet, Christophe, Samuel Rivallant, and Jean-Jacques Barrau. "Low velocity impact modeling in composite laminates capturing permanent indentation." Composites Science and Technology 72.16 (2012): 1977-1988.

[38] Yashiro, S., J. Takatsubo, and N. Toyama. "An NDT technique for composite structures using

visualized Lamb-wave propagation." Composites Science and Technology 67.15-16 (2007): 3202-3208.

[39] Hill, Kenneth O., and Gerald Meltz. "Fiber Bragg grating technology fundamentals and overview." Journal of Lightwave Technology 15.8 (1997): 1263-1276.

[40] Hayashi, Takahiro, Won-Joon Song, and Joseph L. Rose. "Guided wave dispersion curves for a bar with an arbitrary cross-section, a rod and rail example." Ultrasonics 41.3 (2003): 175-183.

[41] Nishikawa, Yasuhiro, et al. "Fatigue crack constraint in plain-woven CFRP using newly-developed spread tows." International Journal of Fatigue 28.10 (2006): 1248-1253.

[42] Gao, F., et al. "Damage accumulation in woven-fabric CFRP laminates under tensile loading: Part 1. Observations of damage accumulation." Composites Science and Technology 59.1 (1999): 123-136.

[43] Gao, F., et al. "Damage accumulation in woven-fabric CFRP laminates under tensile loading: 2. Modelling the effect of damage on macro-mechanical properties." Composites Science and Technology 59.1 (1999): 137-145.

[44] Kim, Jang-Kyo, and Man-Lung Sham. "Impact and delamination failure of woven-fabric composites." Composites Science and Technology 60.5 (2000): 745-761.

Appendix Chapter A: Investigation of guided wave propagation in a fabric CFRP laminates

A.1 Introduction of fabric CFRP

In the previous chapters, the simplified modeling method was verified to be appropriate for a CFRP laminate and a CFRP skin/hat-shaped stringer structure. These two kinds of structures are both made of TORAYCA® prepreg (hereafter called prepreg CFRP), which is a sheet-shaped material using straight carbon fiber. The fibers in prepreg CFRP are arranged in the same direction in one single ply.

In this chapter, we attempted to explore more possibilities of this simulation method with the application to CFRP structures made of a fabric woven with carbon fiber tow (hereafter called fabric CFRP). The fibers in fabric CFRP are arranged in two directions perpendicular to each other in one single ply.

Over the past decades, fabric CFRP have been widely applied to the design of automobile components, wind turbine blades, primary aircraft structures, sports equipment and other industrial products [41]. Compared to prepreg CFRP, the advantages of fabric CFRP include that: it has an excellent drapability which means it is easier to be molded [42][43]. This enables the applicability in many complex-shaped CFRP structures with curved surfaces.

Fig. A.1 shows the difference in appearance between prepreg CFRP laminates and fabric CFRP laminates. In order to investigate the impact damage generated in them, we conducted a cross-sectional observation of a fabric CFRP laminate and compared it with that of a prepreg CFRP laminate. The results are shown in **Fig. A.2**.

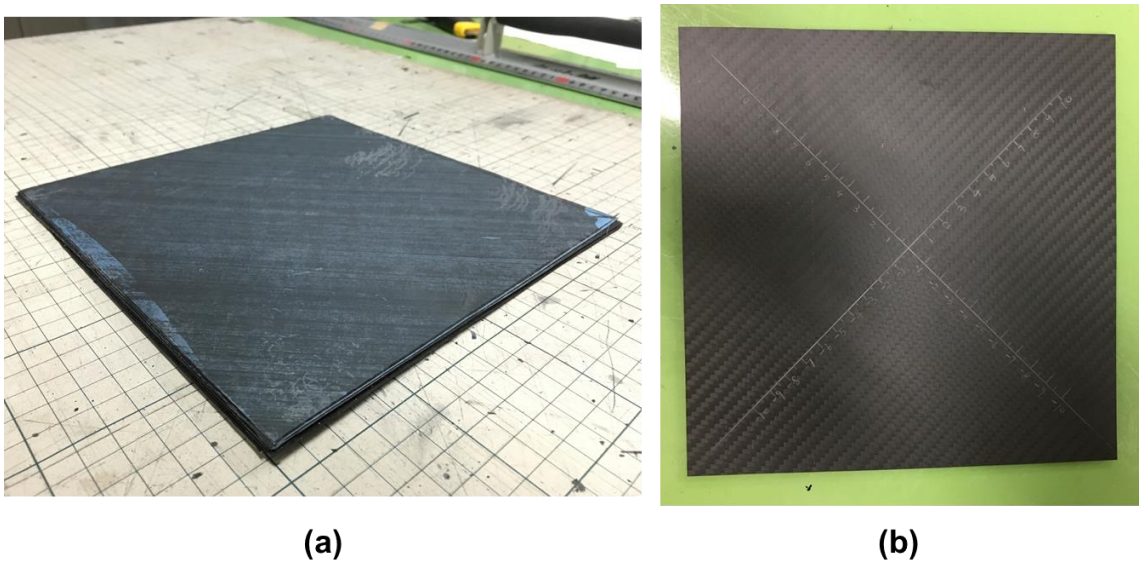

Fig. A.1. (a) Prepreg CFRP laminate and (b) fabric CFRP laminate.

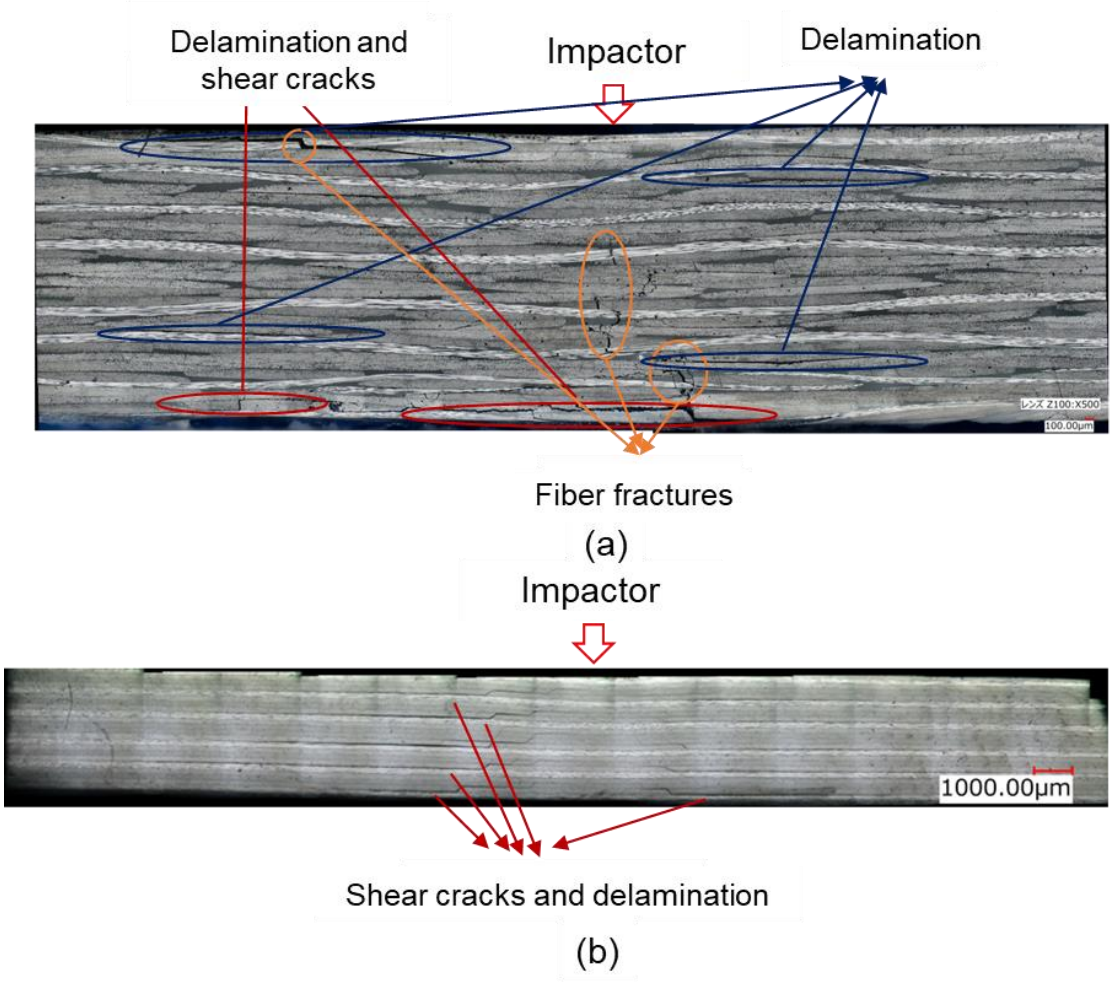

Fig. A.2. Comparison of cross-sectional observation between (a) post-impacted prepreg CFRP laminate and (b) post-impacted fabric CFRP laminate.

Fig. A.2 shows that there are more fiber break damages and shorter delamination damages existing in the impact-damaged area of the fabric CFRP laminate, which is largely different from those of the prepreg CFRP laminate.

A.2 Application of simplified modeling method in a fabric CFRP laminates

A.2.1 Application of simplified modeling method

We attempted to apply the simplified modeling method in a fabric CFRP laminate. We prepared a 3.695-mm-thick woven-fabric CFRP quasi-isotropic laminate plate ($[0/45]_{4s}$) as shown in **Fig. A.1** (b). The density and stiffness constants are listed in **Table A.1**. Impact damage in the form of a 4-mm-diameter dent was generated at the center of the plate, then the size of the damaged area was measured by a C-scan and found to be 14.4 mm in diameter.

However, because of the difference in damage distribution as shown in **Fig. A.2**, the degradation rates of stiffness probably differ from those of a prepreg CFRP laminate. Thus, we recalculated the degraded stiffness in the impact-damaged area with the same method used in **Chapter 2**. The input wave was a three-cycle sinusoidal wave with a Hamming window at 150 kHz. The recalculated stiffness in the impact-damaged area is shown in **Table A.2**.

Table A.1. Density and stiffness constants of the fabric CFRP laminates.

	ρ	C_{11}	C_{12}	C_{13}	C_{33}	C_{44}	C_{66}
Quasi-isotropic	1622	54.8098	17.3549	4.11296	10.3835	4.2357	18.7275

Density in kg/m^3 and stiffness constants in GPa.

Table A.2. Density and stiffness constants of the impact-damaged area of the fabric CFRP laminates.

	ρ	C_{11}	C_{12}	C_{13}	C_{33}	C_{44}	C_{66}
Impact-damaged area	1622	45.594	14.437	0	10.3835	2.540	15.579

Density in kg/m^3 and stiffness constants in GPa.

In the simplified modeling method in a fabric CFRP laminate, the impact-damaged area is also considered as a frustum shape with the dimensions determined by the dent size and the C-scan results. The stiffness parameters in **Table A.1** are used in the intact area and the stiffness parameters in **Table A.2** are used in the impact-damaged area.

A.2.2 Verification of validity

Using the same verification method discussed in **Chapter 2**, we attempted to verify the validity of the simplified modeling method in a fabric CFRP laminate.

In the previous discussion, the multiple delamination model considered that each peanut-shaped delamination between two adjacent plies faced towards the direction of fibers of the deeper ply. According to this, since two directions of fibers are woven fabricated in one single ply in the fabric CFRP laminate, the peanut-shaped delamination between two adjacent plies should face

toward both directions of fibers of the deeper ply. Thus, the multiple-delamination model used to verify the simplified modeling method is considered slightly different from that in **Chapter 2**. The shape of the delamination is considered to be double peanut-shaped. The difference of delamination used in the multiple delamination model of impact damage between prepreg CFRP laminate and fabric CFRP laminate is shown in **Fig. A.3**.

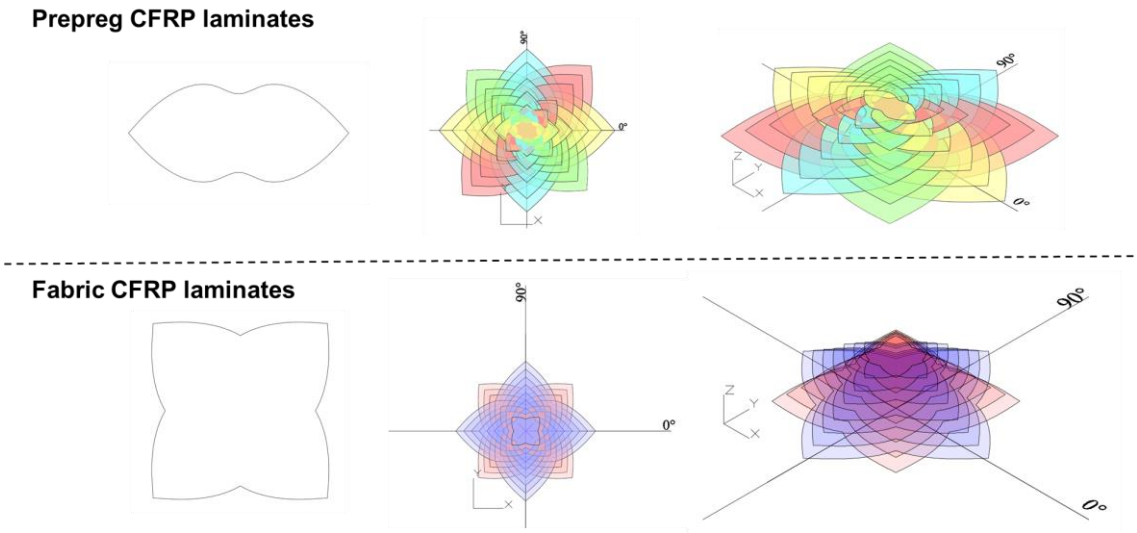

Fig. A.3. Delamination used in the multiple delamination model of impact damage between the UD CFRP laminate and woven-fabric CFRP laminate

A comparison between the simplified modeling method, multiple delamination model and experimental results was then made. The difference in propagation time between the wave in the damaged plate and that in the intact plate at different propagation distances is plotted in **Fig. A.4**.

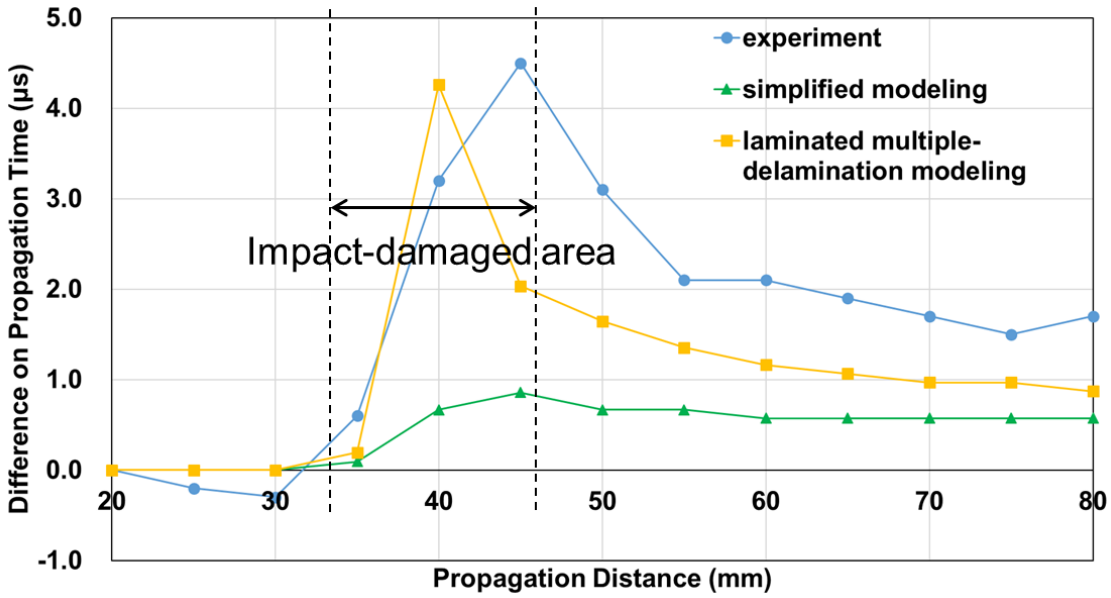

Fig. A.4. Difference in propagation time between the wave in the damaged plate and that in the intact plate at different propagation distances. The plate is a fabric CFRP laminate.

Fig. A.4 shows that, although the three cases all have a stable delay in propagation time, which is evidence of the existence of impact damage, there is a mismatch of difference in propagation time after passing through the impact-damaged area between the three kinds of results. This is mainly because there are more fiber breaks and shorter delamination existing in the impact-damaged area, which is different from that of prepreg CFRP laminate, as **Fig. A.2** indicates.

In specific, when impact is applied to the plate, the damage occurs firstly in the bottom side due to the bending of the plate. In the case of CFRP laminates made of prepreg, long delamination occurs in the bottom side and gradually absorbs the impact energy. Therefore, the delamination

becomes shorter as approaching the top surface, and it is considered reasonable to model the impact damage with a frustum shape.

However, in the case of a fabric CFRP laminates, since the fiber bundle of the woven fabric is undulated, it is hard for interlaminar delamination to progress linearly. This results in the length of all the interlaminar delaminations are short. Because of this, short delamination, cracks and fiber breakage are generated dispersedly throughout the plate thickness to absorb the impact energy, rather than absorbing the impact energy mainly by the bottom side.

In other words, the impact damage in a fabric CFRP laminates may not be of frustum shape, and it is thought close to bell shape or cylindrical shape, as can be seen from the details of cross-sectional observation in the **Fig. A.5**. We can also find that the damage area was similar between the top and bottom surfaces of the laminate according to some researches [44].

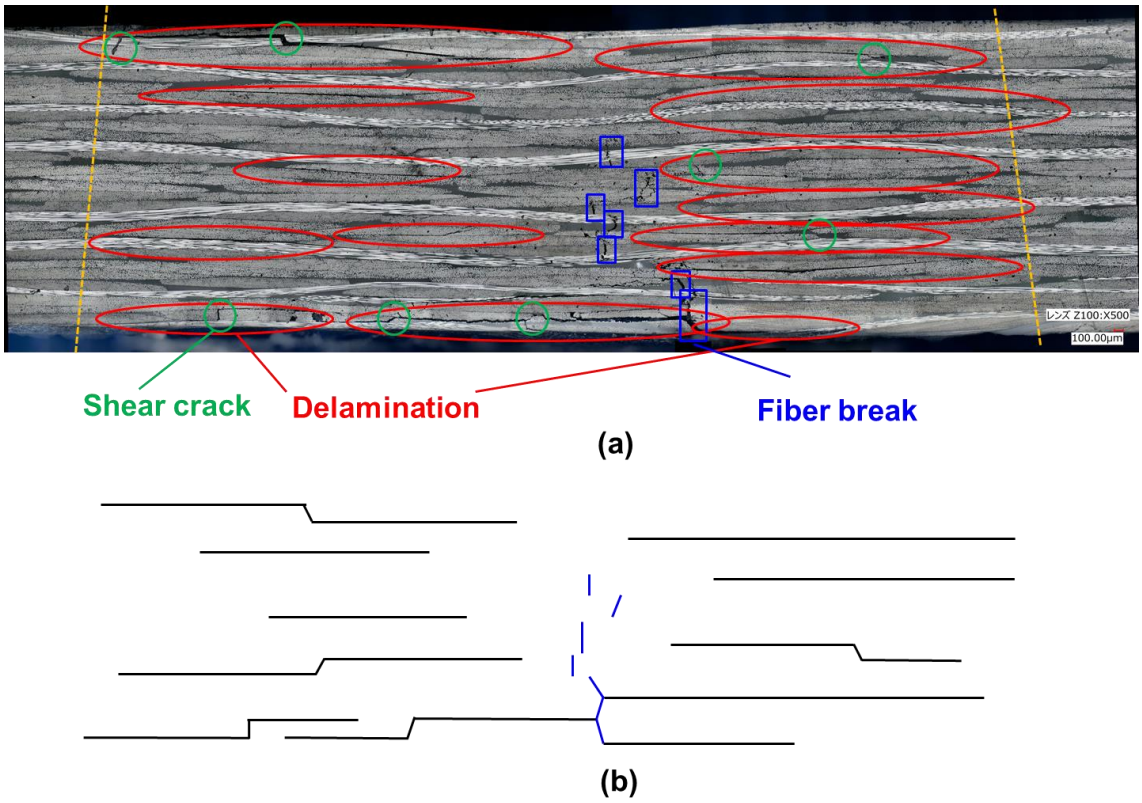

Fig. A.5. (a) Cross-sectional image of impacted fabric CFRP laminates observed by a microscope and (b) schematic of the damages.

Therefore, assuming the impact damage as frustum shape will result in a FE model that is smaller than the real damage, and according to the analysis results in **Fig. A.4**, the delay in the simulated results are indeed smaller than that of the experiment results.

From this, it can be implied that the multiple delamination model of fabric CFRP laminates in **Fig.A.3** is not appropriate, and in the future work, it is necessary to discuss about creating models with bell shape or cylindrical shape.

Appendix Chapter B: Comparison between simulation results and experiments results using the estimated stiffness constants of T700SC/2500

In **Fig. 2.18**, difference in propagation time between the wave in the damaged plate and that in the intact plate at different propagation distances were first plotted between the two modelings. And that of experimental results was also plotted in another graph in **Fig.2.18**. We can't compare the two graphs together directly because they are of different material.

However, in order to enable the comparison between the simulation results and experimental results, we considered a method to estimate the stiffness constants of T700SC/2500.

Table B.1. Estimation of density and stiffness constants of CFRP (T700SC/2500)

	ρ	C_{11}	C_{12}	C_{13}	C_{33}	C_{44}	C_{66}
Quasi-isotropic	1530	42.98	19.31 (T700S/2500)	5.16 (T700S/2500)	11.69	3.92	11.84
Unidirectional	1530	95.362	8.764	8.764	11.69	10.691	2.4

Density in kg/m^3 and stiffness constants in GPa.

In **Table B.1**, C_{11}, C_{44} are estimated by the measured velocities of intact area in the ultrasonic experiments in **Section 2.2.3.1** according to the **Eq. (13)**; C_{33} is calculated by the measured velocity of bulk wave of intact area in **Fig. 2.10 (a)** according to the **Eq. (4)**; C_{12} and C_{13} used the stiffness constants of T700S/2500 and C_{66} is calculated according **Eq. (1)**. We also assumed the density of T700SC/2500 is the same as that of T700S/2500. Besides, we made a C++ program to search the unidirectional stiffness constant by scanning parameters under the assumption of homogeneity.

The stiffness constants in the impact-damaged area were then calculated according to the same degradation ratio or degradation method in **Section 2.2.3**, respectively (see **Table B.2**).

Table B.2. Density and stiffness constants of impact-damaged area in the simplified modeling method (T700SC/2500)

	ρ	C_{11}	C_{12}	C_{13}	C_{33}	C_{44}	C_{66}
Impact-damaged area	1530	31.67	14.22	0	11.69	2.31	8.73

Density in kg/m^3 and stiffness constants in GPa

We then substituted these estimated stiffness constants of T700SC/2500 into the FEM simulation and recalculated the simplified modeling case and laminated multiple delamination

case. The comparison between simulation results and experimental results are shown in **Fig. B.1**.

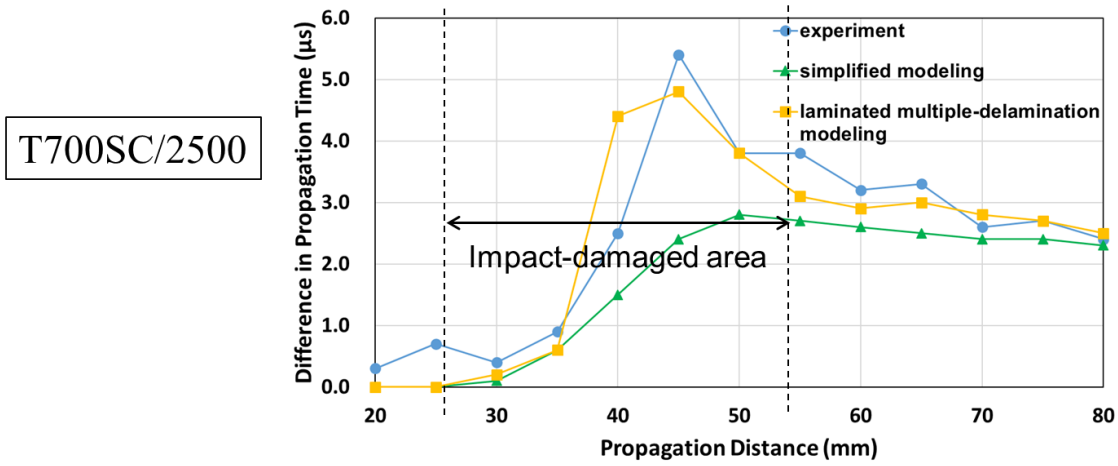

Fig. B.1. Difference in propagation time between the wave in the damaged plate and that in the intact plate at different propagation distances. Two kinds of modeling results and experimental result are compared.

Fig. B.1 shows that, the tendency of difference in propagation time agreed among two kinds of simulation results and the experiment result. This also indicates that our simplified modeling method is quantitatively appropriate for modeling the impact damage in Lamb wave propagation simulation in quasi-isotropic composite structures.

Acknowledgement

There are many people that have earned my gratitude for their contribution to my research work and daily life during the doctoral study period.

First and foremost, I would like to thank my supervisor, Prof. Yoji Okabe, director of the Okabe Laboratory in University of Tokyo. Since I started my application for doctoral program, he has given me endless support. Under his supervision, I learned how to define a research problem, find a solution to it, and finally publish the results. He helped me come up with the research topic and guided me though my entire doctoral study period.

I then would like to thank my secondary advisor, research associate, Dr. Osamu Saito. He gave me a lot of advices about the theoretical sections, especially the section of calculating the dispersion curves. He was always supportive and ready to help others.

Besides my advisors, I would like to thank Dr. Fengming Yu, for giving valuable advices about principles of experiments. I would like to thank master students Huan Guo, Chao Tang, Chang Su and Ge Zhang for helping me with a lot of experiments. Many thanks to the rest of members in Okabe Lab and I am very happy working with you.

I am also grateful to my industrial collaborators. This work was conducted as a part of the project “Practical applications of SHM” under the contract with RIMCOF founded by NEDO and

as a part of the collaborative project with Yamaha Motor Co., Ltd.

Many thanks to my graduation thesis review board, your valuable opinions have enabled me to see the deficiencies in my thesis and to revise them.

Thank my friends in Institute of Industrial Science and in University of Tokyo, you made my doctoral study period colorful and meaningful.

Last but not least, I would like to express my deepest gratitude to my family and all my friends. This research would not have been possible without your sincere love and endless support.